J. Fluid Mech. (2013), *vol.* 716, *pp.* 349–413. © Cambridge University Press 2013
doi:10.1017/jfm.2012.549

Nonlinear stability, bifurcation and vortical patterns in three-dimensional granular plane Couette flow

Meheboob Alam[1],† **and Priyanka Shukla**[2]

[1]Engineering Mechanics Unit, Jawaharlal Nehru Centre for Advanced Scientific Research, Jakkur P.O., Bangalore 560064, India

[2]Department of Mathematics and Statistics, Indian Institute of Science Education and Research Kolkata, P.O.: BCKV Campus, Mohanpur, Nadia 741252, India

(Received 28 June 2012; revised 30 October 2012; accepted 5 November 2012)

The effects of three-dimensional (3D) perturbations, having wave-like modulations along both the streamwise and spanwise/vorticity directions, on the nonlinear states of five types of linear instability modes, the nature of their bifurcations and the resulting nonlinear patterns are analysed for granular plane Couette flow using an order-parameter theory which is an extension of our previous work on two-dimensional (2D) perturbations (Shukla & Alam, *J. Fluid Mech.*, vol. 672, 2011*b*, pp. 147–195). The differential equations for modal amplitudes (the fundamental mode, the mean-flow distortion, the second harmonic and the distortion of the fundamental mode), up to cubic-order in perturbation amplitude, are solved using a spectral-based numerical technique, yielding an estimate of the first Landau coefficient that accounts for the leading-order nonlinear effect on finite-amplitude perturbations. In the near-critical regime of flows, we found evidence of mean-flow resonance, characterized by the divergence of the first Landau coefficient, that occurs due to the interaction/resonance between a linear instability mode and a mean-flow mode. The nonlinear solutions are found to appear via both pitchfork and Hopf bifurcations from the underlying linear instability modes, leading to supercritical nonlinear states of stationary and travelling wave solutions. The subcritical travelling wave solutions have also been uncovered in the linearly stable regimes of flow. It is shown that multiple nonlinear states of both stationary and travelling waves can coexist for a given parameter combination of mean density and Couette gap. The 3D nonlinear solutions persist for a range of spanwise wavenumbers up to $k_z = O(1)$ that originate from 2D instabilities which occur beyond a moderate value of the mean density. For purely 3D instabilities in dilute flows (having no analogue in 2D flows), the supercritical finite-amplitude solutions persist for a much larger range of spanwise wavenumber up to $k_z = O(10)$. For all instabilities, the vortical motion on the cross-stream plane has been characterized in terms of the fixed/critical points of the underlying flow field: saddles, nodes (sources and sinks) and vortices have been identified. While the cross-stream velocity field for supercritical solutions in dilute flows contains nodes and saddles, the subcritical solutions are dominated by large-scale vortices in the background of saddle-node-type motions. The latter type of flow pattern also persists at moderate densities in the form of supercritical nonlinear solutions that originate from the dominant 2D instability modes for which the vortex appears to be driven by two nearby saddles. The location

† Email address for correspondence: meheboob@jncasr.ac.in

https://doi.org/10.1017/jfm.2012.549 Published online by Cambridge University Press

of this vortex is found to be correlated with the local maxima of the streamwise vorticity.

Key words: granular media, nonlinear instability, pattern formation

1. Introduction

Understanding instabilities and patterns are important from both the fundamental and practical standpoints of modelling granular materials since inhomogeneities have a significant impact on the rheological properties of granular materials (Jackson 2000). When a system is driven by external forcing, it becomes unstable beyond some critical value of the control parameter by admitting various types of spatio-temporal instabilities. The collective behaviour of such unstable systems (e.g. fluid flows), far from equilibrium, yields a variety of patterned states (Cross & Hohenberg 1993). Such instability-induced pattern formation in rapid granular flows (Goldhirsch 2003; Alam *et al.* 2005; Aranson & Tsimring 2006) has attracted much attention during the past two decades. Some examples of patterned states in simple granular flow configurations are: squares, stripes, hexagons and oscillons in vertically vibrated shallow granular layers (Umbanhower, Melo & Swinney 1996); convection in vibrated deep granular layers under strong shaking (Gallas, Herrmann & Sokolowski 1992; Ramirez, Risso & Cordero 2000; Eshuis *et al.* 2010); and clustering, density waves and vortices in granular shear flows (Hopkins, Jenkins & Louge 1993; Alam & Nott 1998; Forterre & Pouliquen 2002; Goldfarb, Glasser & Shinbrot 2002; Conway & Glasser 2004; Raafat, Hulin & Herrmann 1996; Alam, Chikkadi & Gupta 2009; Woodhouse & Hogg 2010). Sand dunes and ripples (Sauermann, Kroy & Herrmann 2001) are examples of large-scale patterns in nature involving granular/particulate flows.

In the realm of rapid granular flows, the planar Couette shear flow has served as an ideal test-bed to study instabilities and patterns. Phenomena such as particle clustering, density waves and segregation in granular plane Couette flow have been studied using both particle simulations and stability analyses of hydrodynamic-like equations (Savage 1992; McNamara 1993; Tan & Goldhirsch 1997; Alam & Nott 1998; Goddard & Alam 1999; Conway & Glasser 2004; Alam 2005; Alam *et al.* 2005; Gayen & Alam 2006; Khain & Meerson 2006; Saitoh & Hayakawa 2007; Alam, Shukla & Luding 2008). For a brief of overview of these theoretical and simulation works, we refer to the introductory section of Shukla & Alam (2011*b*).

The study of nonlinear stability of granular flows has been initiated by us (Alam & Shukla 2008) focusing on 'bounded' granular plane Couette flow. An order-parameter theory has been developed resulting in the Landau–Stuart equation that governs the evolution of finite-amplitude perturbations. The Landau–Stuart equation for the temporal evolution of a single mode has been derived from granular hydrodynamic equations following two different approaches: (i) the centre-manifold reduction technique (Carr 1981; Shukla & Alam 2009); and (ii) the amplitude expansion method (Stuart 1960; Watson 1960; Shukla & Alam 2011*a*,*b*). Using this order-parameter theory, we have investigated the nonlinear saturation of two types of perturbations: (i) gradient-banding instability (Shukla & Alam 2009, 2011*a*; Alam & Shukla 2012); and (ii) two-dimensional (2D) perturbations (Shukla & Alam 2011*b*). (Note that the related nonlinear gradient-banding problem in 'unbounded' granular shear flow was probed later by Saitoh & Hayakawa (2011) using a complex Ginzburg–Landau equation.) A

https://doi.org/10.1017/jfm.2012.549 Published online by Cambridge University Press

summary of our main results on the nonlinear stability of 2D granular plane Couette flow is as follows.

(i) The nonlinear gradient-banding instabilities ($k_x = 0$, where k_x is the wavenumber along the flow/streamwise direction) appear beyond a minimum value of the mean density ($\phi = \phi_c \sim 0.15$, where ϕ is the volume fraction of particles). This is responsible for *shear-band formation* (leading to shear-localization with density segregation along the gradient direction) via supercritical pitchfork bifurcations; there are subcritical gradient-banding states at $\phi < \phi_c$ that bifurcate from infinity.

(ii) The flow is subcritically unstable to stationary 2D perturbations of long wavelengths ($k_x \sim 0$) in the dilute limit, the origin of which is tied to the underlying subcritical gradient-banding modes.

(iii) For moderate-to-large values of mean densities, supercritical nonlinear states exist which appear via pitchfork and Hopf bifurcations from the underlying gradient-banding, long-wavelength, and dominant stationary and travelling wave instabilities. The dominant instabilities (having the largest growth rate among all instabilities) appear at $k_x = O(1)$.

It was found (Shukla & Alam 2011*b*) that multiple nonlinear states of stationary and/or oscillatory solutions can coexist for a given set of control parameters. Overall, the predictions of this 2D nonlinear stability theory, in terms of both the nature of bifurcation (pitchfork/Hopf) and the resulting nonlinear patterned states, agree qualitatively with particle simulations (Tan & Goldhirsch 1997; Conway & Glasser 2004).

The nonlinear states of three-dimensional (3D) instability modes have remained unexplored and are the focus of this paper. The related linear stability analysis of 3D granular plane Couette flow has been done by Alam (2006). It was shown that the flow is unstable to pure spanwise stationary perturbations in the dilute limit which leads to density inhomogeneities in the form of dense and dilute regions of particles along the spanwise/vorticity direction. Apart from pure spanwise instability, a new travelling instability for non-zero streamwise wavenumbers was uncovered for dilute flows as well as another new mode that has an anomalous dependence on inelasticity. In moderate-to-dense flow regimes, different 3D stationary and travelling instabilities have been identified which originate from their 2D counterparts. In this paper we investigate the nonlinear stability of 3D granular plane Couette flow, generalizing our previous work (Shukla & Alam 2011*b*) on 2D flows. In addition, a first attempt is made to characterize the 3D flow patterns using critical-point concepts of dynamical systems theory.

This paper is organized as follows. The problem description and the governing equations are given in § 2. Neglecting nonlinearities, the linear stability problem and its adjoint are formulated in § 3. A brief account of the nonlinear analysis, adapted from the amplitude expansion method (Stuart 1960; Watson 1960; Shukla & Alam 2011*a*,*b*), is provided in § 4: the specific changes due to the three-dimensionality of perturbations are mentioned. This leads to an order-parameter theory for a single mode in terms of the well-known Landau–Stuart equation. The differential equations for the modal amplitudes of nonlinear perturbations are solved numerically using a spectral-based numerical scheme as detailed in § 5. The Landau–Stuart equation and the forms and a certain symmetry of the resulting nonlinear perturbation fields are analysed in § 6. As in previous studies, we restricted calculations to only the first Landau coefficient which provides the leading-order nonlinear effects on stability. The detailed results on the finite-amplitude solutions, the nature of bifurcations and the

https://doi.org/10.1017/jfm.2012.549 Published online by Cambridge University Press

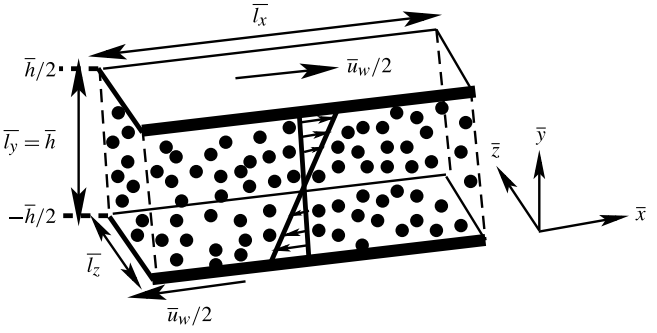


FIGURE 1. Schematic diagram of 3D plane Couette flow of smooth granular materials. Both plates move with the same velocity $\bar{u}_w/2$ but in opposite directions. The gap between the two plates is $\bar{l}_y = \bar{h}$, and the length and the depth of the channel are $\bar{l}_x$ and $\bar{l}_z$, respectively.

underlying nonlinear patterns (of density, granular temperature, cross-stream velocity and streamwise vorticity) are presented in § 7 for five types of linear instability modes in dilute, moderately dense and dense flows. In an effort to understand the underlying vortical/eddying motion, the cross-stream velocity field has been characterized in terms of its fixed/critical/stationary points (saddles, nodes, focus/vortex) as discussed in §§ 7.1–7.3. The implications of the present results from the viewpoint of particle simulations are discussed in § 8. The conclusions and suggestions for future work are given in § 9.

2. Problem description and hydrodynamic equations

The granular flow driven by two oppositely moving parallel walls, as shown schematically in figure 1, is the focus of this paper. Mono-disperse, smooth and identical spherical particles of intrinsic density $\overline{\rho}$ and diameter $\overline{d}$ are taken as model granular materials. The coordinates, $\bar{x}$, $\bar{y}$ and $\bar{z}$, refer to streamwise (flow), transverse (normal or gradient) and spanwise directions, respectively. For a continuum description of granular materials, we use the Navier–Stokes-order hydrodynamic equations that have been derived from a kinetic-theory approach (Jenkins & Richman 1985; Sela & Goldhirsch 1998; Garzo & Dufty 1999; Brilliantov & Pöschel 2004). At this order, there are five hydrodynamic fields: (i) the mass density $\overline{\varrho} = \overline{m}\,\overline{n} = \overline{\rho}\phi$, where $\overline{m}$, $\overline{n}$, $\overline{\rho}$ and ϕ are the particle mass, number density, material density and the volume fraction of particles, respectively; (ii–iv) the bulk/hydrodynamic velocity $\overline{\boldsymbol{u}} = (\overline{u}, \overline{v}, \overline{w})$, where $\overline{u}$, $\overline{v}$ and $\overline{w}$ are the components of velocity along the $\bar{x}$-, $\bar{y}$- and $\bar{z}$-directions, respectively; (v) the granular temperature $\overline{T}$ which is a measure of the fluctuation kinetic energy of particles.

As in our previous work (Shukla & Alam 2009, 2011*a*,*b*), we choose a simplified version of the kinetic-theory constitutive model for the granular stress ($\overline{\boldsymbol{\Sigma}}$) and the pseudo-thermal heat flux ($\overline{\boldsymbol{q}}$):

$$\overline{\boldsymbol{\Sigma}} = \left(\overline{p} - \overline{\zeta}(\overline{\boldsymbol{\nabla}} \cdot \overline{\boldsymbol{u}})\right) \boldsymbol{I} - 2\overline{\mu}\,\overline{\boldsymbol{S}}, \tag{2.1}$$

$$\overline{\boldsymbol{q}} = -\overline{\kappa}\,\overline{\boldsymbol{\nabla}}\,\overline{T} - \overline{\kappa}_h \overline{\boldsymbol{\nabla}}\,\overline{\varrho}, \tag{2.2}$$

where $\overline{p}(\phi, \overline{T})$ is the pressure, $\overline{\mu}(\phi, \overline{T})$ and $\overline{\zeta}(\phi, \overline{T})$ are the coefficients of shear and bulk viscosities, respectively, $\overline{\kappa}(\phi, \overline{T})$ is the granular thermal conductivity, $\boldsymbol{I}$ is the

https://doi.org/10.1017/jfm.2012.549 Published online by Cambridge University Press

identity tensor and $\overline{\boldsymbol{S}} = (\overline{\boldsymbol{\nabla}}\overline{\boldsymbol{u}} + (\overline{\boldsymbol{\nabla}}\overline{\boldsymbol{u}})^{\mathrm{T}})/2 - (\overline{\boldsymbol{\nabla}} \cdot \overline{\boldsymbol{u}})\boldsymbol{I}/3$ is the deviatoric strain rate tensor. In the heat-flux relation (2.2), the contribution of the non-Fourier term ($\overline{\kappa}_h$), which is proportional to the gradients in particle volume fraction, is neglected in all calculations in this paper; this can be justified from our previous works showing that this term does not introduce any new instability in either unbounded (Gayen & Alam 2006) or bounded (Alam & Nott 1998; Alam 2006) plane shear flows of granular materials; see appendix A for a discussion on the robustness of linear instability modes in 3D granular Couette flow for two sets of constitutive relations. Moreover, it has been recently shown that this non-Fourier term does not qualitatively affect the observed instabilities in two additional classes of shear flows: (i) granular Poiseuille flow (Alam *et al.* 2009); and (ii) the granular flow down an inclined chute (Woodhouse & Hogg 2010).

It may be noted that the above Newtonian–Fourier-type constitutive model for a rapid granular fluid holds strictly in the limit of small dissipation/inelasticity. The choice of this constitutive model and its possible range of validity have also been discussed in our recent papers (Shukla & Alam 2011*a*,*b*). It would certainly be worthwhile to check the quantitative effects of more refined constitutive relations (Sela & Goldhirsch 1998; Garzo & Dufty 1999; Garzo, Santos & Montanero 2007; Noskowicz *et al.* 2007) on our predictions of various 3D nonlinear states in plane shear flow; however, such a detailed parametric study is beyond the scope of the present paper and can be taken up in a future comparative analysis.

2.1. *Hydrodynamic equations in dimensionless form*

Let us introduce a reference length $\overline{h}$, equal to the gap between two walls, a reference velocity $\overline{u}_w$, the difference between the wall velocities, and a reference time $\overline{h}/\overline{u}_w$, the inverse of the total shear rate, We define non-dimensional variables as

$$(x, y, z) = (\overline{x}, \overline{y}, \overline{z})/\overline{h}, \quad (u, v, w) = (\overline{u}, \overline{v}, \overline{w})/\overline{u}_w, \quad t = \overline{u}_w \overline{t}/\overline{h}. \tag{2.3}$$

The overbar on any symbol represents a dimensional quantity and its bare counterpart is dimensionless. Using (2.3), the dimensionless forms of granular temperature, stress, heat flux, and the rate of dissipation are defined as

$$T = H^2 \overline{T}/\overline{u}_w^2, \quad \boldsymbol{\Sigma} = H^2 \overline{\boldsymbol{\Sigma}}/\overline{\rho}\,\overline{u}_w^2, \quad \boldsymbol{q} = H^3 \overline{\boldsymbol{q}}/\overline{\rho}\,\overline{u}_w^3 \quad \text{and} \quad \mathcal{D} = H^3 \overline{d}\,\overline{\mathcal{D}}/\overline{\rho}\,\overline{u}_w^3, \tag{2.4}$$

respectively, where $H = \overline{h}/\overline{d}$ is the dimensionless Couette gap in terms of particle diameter.

The resulting dimensionless equations for hydrodynamic fields $\phi(x, y, z, t)$, $u(x, y, z, t)$, $v(x, y, z, t)$, $w(x, y, z, t)$ and $T(x, y, z, t)$ are

$$\left(\frac{\partial}{\partial t} + \boldsymbol{u} \cdot \boldsymbol{\nabla}\right) \phi = -\phi \boldsymbol{\nabla} \cdot \boldsymbol{u}, \tag{2.5}$$

$$\begin{aligned} \phi \left(\frac{\partial}{\partial t} + \boldsymbol{u} \cdot \boldsymbol{\nabla}\right) u = &-\frac{1}{H^2}\frac{\partial p}{\partial x} + \frac{1}{H^2}\frac{\partial}{\partial x}\left[2\mu \frac{\partial u}{\partial x} + \lambda(\boldsymbol{\nabla} \cdot \boldsymbol{u})\right] \\ &+ \frac{1}{H^2}\frac{\partial}{\partial y}\left[\mu\left(\frac{\partial u}{\partial y} + \frac{\partial v}{\partial x}\right)\right] + \frac{1}{H^2}\frac{\partial}{\partial z}\left[\mu\left(\frac{\partial u}{\partial z} + \frac{\partial w}{\partial x}\right)\right], \end{aligned} \tag{2.6}$$

$$\begin{aligned} \phi \left(\frac{\partial}{\partial t} + \boldsymbol{u} \cdot \boldsymbol{\nabla}\right) v = &-\frac{1}{H^2}\frac{\partial p}{\partial y} + \frac{1}{H^2}\frac{\partial}{\partial y}\left[2\mu \frac{\partial v}{\partial y} + \lambda(\boldsymbol{\nabla} \cdot \boldsymbol{u})\right] \\ &+ \frac{1}{H^2}\frac{\partial}{\partial z}\left[\mu\left(\frac{\partial v}{\partial z} + \frac{\partial w}{\partial y}\right)\right] + \frac{1}{H^2}\frac{\partial}{\partial x}\left[\mu\left(\frac{\partial u}{\partial y} + \frac{\partial v}{\partial x}\right)\right], \end{aligned} \tag{2.7}$$

https://doi.org/10.1017/jfm.2012.549 Published online by Cambridge University Press

$$\phi\left(\frac{\partial}{\partial t}+\boldsymbol{u}\cdot\boldsymbol{\nabla}\right)w=-\frac{1}{H^2}\frac{\partial p}{\partial z}+\frac{1}{H^2}\frac{\partial}{\partial z}\left[2\mu\frac{\partial w}{\partial z}+\lambda(\boldsymbol{\nabla}\cdot\boldsymbol{u})\right]$$
$$+\frac{1}{H^2}\frac{\partial}{\partial x}\left[\mu\left(\frac{\partial u}{\partial z}+\frac{\partial w}{\partial x}\right)\right]+\frac{1}{H^2}\frac{\partial}{\partial y}\left[\mu\left(\frac{\partial v}{\partial z}+\frac{\partial w}{\partial y}\right)\right], \tag{2.8}$$

$$\frac{3}{2}\phi\left(\frac{\partial}{\partial t}+\boldsymbol{u}\cdot\boldsymbol{\nabla}\right)T=\frac{1}{H^2}\boldsymbol{\nabla}\cdot(\kappa\boldsymbol{\nabla}T+\kappa_h\boldsymbol{\nabla}\phi)-p(\boldsymbol{\nabla}\cdot\boldsymbol{u})$$
$$+2\mu\left[\left(\frac{\partial u}{\partial x}\right)^2+\left(\frac{\partial v}{\partial y}\right)^2+\left(\frac{\partial w}{\partial z}\right)^2+\frac{1}{2}\left(\frac{\partial u}{\partial y}+\frac{\partial v}{\partial x}\right)^2\right.$$
$$\left.+\frac{1}{2}\left(\frac{\partial v}{\partial z}+\frac{\partial w}{\partial y}\right)^2+\frac{1}{2}\left(\frac{\partial w}{\partial x}+\frac{\partial u}{\partial z}\right)^2+\frac{\lambda}{2\mu}(\boldsymbol{\nabla}\cdot\boldsymbol{u})^2\right]-\mathcal{D}, \tag{2.9}$$

The transport coefficients in dimensionless form are

$$\left.\begin{aligned} p(\phi,T)&=f_1(\phi)\,T, & \mu(\phi,T)&=f_2(\phi)\,T^{1/2},\\ \zeta(\phi,T)&=f_3(\phi)\,T^{1/2}, & \lambda(\phi,T)&=(\zeta-\tfrac{2}{3}\,\mu),\\ \kappa(\phi,T)&=f_4(\phi)\,T^{1/2}, & \kappa_h(\phi,T)&=f_{4h}(\phi,e)\,T^{3/2},\\ \mathcal{D}(\phi,T)&=f_5(\phi,e)\,T^{3/2}, \end{aligned}\right\} \tag{2.10}$$

where f_1–f_5 represent dimensionless functions of particle volume fraction ϕ and restitution coefficient e given in appendix A. As discussed in the introduction to this section (see also the discussion in appendix A), we set the non-Fourier term of granular heat flux to zero ($f_{4h}=0$) in all calculations below since this term does not qualitatively affect our instability results. The following expression for the radial distribution function $\chi(\phi)$ is used:

$$\chi(\phi)=\frac{1}{1-(\phi/\phi_{max})^{1/3}} \tag{2.11}$$

that diverges in the random close packing limit ($\phi\to\phi_{max}\equiv 0.65$). We have verified that the qualitative nature of the nonlinear results remains unaltered even if the Carnahan–Starling form for $\chi(\phi)$ is adopted. We use no-slip and zero-heat-flux boundary conditions as in our previous studies. It may be noted that the nonlinear analysis described in §§ 3 and 4 can be easily adapted to ascertain the effect of gravity on the shear flow (as well as in other flows, for example, in granular convection) by adding the gravitational force term to (2.7). Of course, the underlying base state (§ 2.2) would be characterized by non-uniform shear when gravity is included (Alam *et al.* 2005).

2.2. *Base flow of uniform shear*

We consider a steady $[\partial/\partial t(\cdot)=0]$ and fully developed $[\partial/\partial x(\cdot)=0]$ base flow given by

$$\phi=\phi^0(y),\quad \boldsymbol{u}=(u^0(y),0,0)\quad\text{and}\quad T=T^0(y). \tag{2.12}$$

With the no-slip and zero-heat-flux boundary conditions, the base flow equations admit an analytical solution:

$$\phi^0(y)=\text{const.},\quad u^0(y)=y,\quad T^0(y)=\text{const.}=\frac{f_2(\phi^0)}{f_5(\phi^0)}, \tag{2.13}$$

https://doi.org/10.1017/jfm.2012.549 Published online by Cambridge University Press

which represents a state of uniform/homogeneous density, granular temperature and shear rate ($\mathrm{d}u^0/\mathrm{d}y$) throughout the domain. This is the *uniform shear flow* the nonlinear stability of which under 3D perturbations is the focus of this paper.

3. Nonlinear perturbation equations and their linear counterpart

To analyse flow stability, we decompose each hydrodynamic variable, $\underline{X} = (\phi, u, v, w, T)^{\mathrm{Tr}}$, into a mean and its perturbation:

$$\underline{X}(x, y, z, t) = X^0(y) + X(x, y, z, t), \tag{3.1}$$

$$X^0(y) = (\phi^0, u^0, v^0, w^0, T^0)^{\mathrm{Tr}}, \tag{3.2}$$

$$X(x, y, z, t) = (\phi', u', v', w', T')^{\mathrm{Tr}}, \tag{3.3}$$

with the superscripts 0 and prime denoting the mean and the perturbation terms, respectively. Substituting (3.1) into balance equations (2.5)–(2.9) and subtracting the respective mean/base flow equations (§ 2.2), we arrive at the following set of nonlinear perturbation equations in operator form:

$$\left(\boldsymbol{I}\frac{\partial}{\partial t} - \boldsymbol{\mathcal{L}}\right) X = \boldsymbol{\mathcal{N}}(X, X, X, \ldots) = \boldsymbol{\mathcal{N}}_2(X, X; \partial_t) + \boldsymbol{\mathcal{N}}_3(X, X, X) + \cdots, \tag{3.4}$$

where

$$\boldsymbol{\mathcal{L}} \equiv \boldsymbol{\mathcal{L}}\left(\frac{\partial}{\partial x}, \frac{\partial^2}{\partial x^2}, \frac{\partial}{\partial y}, \frac{\partial^2}{\partial y^2}, \frac{\partial}{\partial z}, \frac{\partial^2}{\partial z^2}; \phi^0, H, e, \ldots\right) \tag{3.5}$$

is the linear partial differential operator (see appendix B), $\boldsymbol{\mathcal{N}}_2$ and $\boldsymbol{\mathcal{N}}_3$ are the quadratic and cubic nonlinear terms (see appendix C), respectively, and $\boldsymbol{I}$ is the identity operator. Note that the quadratic nonlinear terms $\boldsymbol{\mathcal{N}}_2(X, X; \partial_t)$ involve time-derivatives that originate from the inertial terms of the hydrodynamic equations.

3.1. *Linear stability problem*

Neglecting nonlinear terms in (3.4), we obtain the linear stability equations:

$$\left(\boldsymbol{I}\frac{\partial}{\partial t} - \boldsymbol{\mathcal{L}}\right) X = 0 \quad \text{with } \boldsymbol{\mathcal{B}}X \equiv \mathrm{diag}\left(0, 1, 1, \frac{\partial}{\partial y}, \frac{\partial}{\partial y}\right) X = 0 \quad \text{at } y = \pm 1/2. \tag{3.6}$$

The coefficients in the linear operator ($\boldsymbol{\mathcal{L}}$) and the boundary operator ($\boldsymbol{\mathcal{B}}$) do not depend explicitly on the streamwise (x) and spanwise (z) coordinates and this makes the linear problem (3.6) translation-invariant in the x- and z-directions. Therefore, we can seek a normal mode solution of the form

$$X(x, y, z, t) = \hat{X}(y)\mathrm{e}^{\mathrm{i}(k_x x + k_z z) + ct} = \left(\hat{\phi}(y), \hat{u}(y), \hat{v}(y), \hat{w}(y), \hat{T}(y)\right)^{\mathrm{Tr}} \mathrm{e}^{\mathrm{i}(k_x x + k_z z) + ct}, \tag{3.7}$$

where k_x and k_z are the streamwise and spanwise wavenumbers, respectively; c is the complex eigenvalue, with $\mathrm{Re}(c)$ and $\mathrm{Im}(c)$ being the growth rate and frequency of the perturbation, respectively. The flow is said to be linearly stable for $\mathrm{Re}(c) < 0$ and unstable for $\mathrm{Re}(c) > 0$.

Substituting (3.7) into (3.6) and equating the exponential terms we obtain a differential eigenvalue problem:

$$\boldsymbol{L}\hat{X} = c\hat{X} \quad \text{with } \boldsymbol{B}\hat{X} = 0, \tag{3.8}$$

https://doi.org/10.1017/jfm.2012.549 Published online by Cambridge University Press

where

$$\boldsymbol{L} \equiv \boldsymbol{\mathcal{L}}\left(\mathrm{i}k_x, (\mathrm{i}k_x)^2, \frac{\mathrm{d}}{\mathrm{d}y}, \frac{\mathrm{d}^2}{\mathrm{d}y^2}, \mathrm{i}k_z, (\mathrm{i}k_z)^2, \ldots\right), \tag{3.9}$$

$$\boldsymbol{B} \equiv \mathrm{diag}\left(0, 1, 1, \frac{\mathrm{d}}{\mathrm{d}y}, \frac{\mathrm{d}}{\mathrm{d}y}\right) \tag{3.10}$$

are the linear stability and boundary operators, respectively. The elements of the linear operator $\boldsymbol{L}$ can be obtained by replacing $\partial^j/\partial x^j \to (\mathrm{i}k_x)^j$ and $\partial^j/\partial z^j \to (\mathrm{i}k_z)^j$ in $\boldsymbol{\mathcal{L}}$ as given in appendix B. The linear eigenvalue problem is invariant under the following co-ordinate rotation:

$$x \to -x, \quad y \to -y, \quad z \to -z, \quad (\hat{\phi}, \hat{u}, \hat{v}, \hat{w}, \hat{T}) \to (\hat{\phi}, -\hat{u}, -\hat{v}, -\hat{w}, \hat{T}). \tag{3.11}$$

This implies that for every forward propagating mode [$\mathrm{Im}(c) > 0$] there is a backward propagating mode [$\mathrm{Im}(c) < 0$] with the same growth rate but having equal and opposite phase speed.

3.2. *Adjoint linear stability operator*

We shall see in § 4 that the calculation of Landau coefficients requires *a priori* knowledge of the adjoint eigenfunction corresponding to the fundamental mode of the linear stability problem. To formulate the adjoint eigenvalue problem we first need to define an adjoint operator corresponding to the linear operator $\boldsymbol{L}$ and the related adjoint boundary conditions based on a suitable inner product. Let us define the adjoint operator $\boldsymbol{L}^\dagger$ such that

$$\langle X^\dagger, \boldsymbol{L}\hat{X}\rangle = \langle \boldsymbol{L}^\dagger X^\dagger, \hat{X}\rangle, \tag{3.12}$$

where the inner product $\langle \cdot, \cdot \rangle$ is defined as

$$\langle f, g\rangle = \int_{-1/2}^{1/2} \tilde{f}(y) g(y)\, \mathrm{d}y \tag{3.13}$$

for two complex-valued vector functions $f(y)$ and $g(y)$, with the tilde denoting a complex-conjugate quantity. Note that the complex conjugation is in the first function of the inner product in (3.13).

The explicit forms of the adjoint operator and the adjoint boundary conditions are obtained from (3.12)–(3.13) by using integration by parts. In matrix notation, the adjoint eigenvalue problem corresponding to (3.8) can be written as

$$\boldsymbol{L}^\dagger X^\dagger = \tilde{c} X^\dagger \quad \text{with } \boldsymbol{B}^\dagger X^\dagger = 0 \quad \text{at } y = \pm 1/2, \tag{3.14}$$

where $X^\dagger(y) = (\phi^\dagger(y), u^\dagger(y), v^\dagger(y), w^\dagger(y), T^\dagger(y))^{\mathrm{Tr}}$ is the adjoint eigenfunction and the elements of adjoint operator $\boldsymbol{L}^\dagger$ are given in appendix B. It has been verified that the adjoint boundary conditions are the same as the boundary conditions of the linear problem ($\boldsymbol{B}^\dagger \equiv \boldsymbol{B}$).

The eigenvalues of the adjoint problem (3.14) are complex conjugates of the eigenvalues of the linear eigenvalue problem. The set of linear eigenvectors are not always orthogonal. To solve the inhomogeneous set of equations of the linear problem, we need to find a set which is orthogonal to all the eigenvectors except one (Eckhaus 1965) and this is called the bi-orthogonality condition. Equation (3.12) can be simplified by using (3.8) and (3.14) to arrive at:

$$(c_j^{(0)} - c_k^{(0)})\langle X_k^\dagger, \hat{X}_j\rangle = 0. \tag{3.15}$$

https://doi.org/10.1017/jfm.2012.549 Published online by Cambridge University Press

Therefore, the bi-orthogonality condition is

$$\langle X_k^{\dagger}, \hat{X}_j \rangle = \delta_{kj}, \tag{3.16}$$

where δ_{kj} is the Kronecker delta.

4. Weakly nonlinear theory for 3D perturbations

The weakly nonlinear stability theory (Stuart 1960; Watson 1960; Reynolds & Potter 1967; Shukla & Alam 2011*a*,*b*) is built around the Fourier decomposition of the linear/basic wave as defined in (3.7) that accounts for the finite size of the perturbation. Information about the amplitude and phase of the infinitesimal-amplitude wave can be separated by rewriting (3.7) as

$$X(x, y, z, t) = X^{[1;1]}(y)\mathrm{e}^{at}\mathrm{e}^{\mathrm{i}(k_x x + k_z z + \omega t)}, \tag{4.1}$$

such that

$$a + \mathrm{i}\omega \equiv c \tag{4.2}$$

is the complex eigenvalue [$a = \mathrm{Re}(c)$ and $\omega = \mathrm{Im}(c)$] of the linear problem (3.8), and $X^{[1;1]} = \hat{X}$ is the linear eigenfunction or the fundamental mode. In (4.1), the first (real) exponential e^{at} represents the time-dependent amplitude and the second (complex) exponential represents the phase of the basic wave.

The following theoretical analysis for 3D perturbations is an extension of our previous analyses for one-dimensional (Shukla & Alam 2011*a*) and 2D (Shukla & Alam 2011*b*) perturbations. The analysis holds fairly generally for the nonlinear stability of any steady base flow of granular materials (plane Couette flow, plane Poiseuille flow, inclined chute flow, granular convection, etc.) under 3D finite-amplitude perturbations, which is described by Newtonian constitutive models with homogeneous and time-independent boundary conditions. Here we outline only a brief sketch of the underlying procedure to arrive at: (i) the Landau equation; (ii) the expressions for the Landau coefficients; and (iii) the related differential equations for the modal amplitudes of finite-amplitude perturbations.

4.1. *Transformed nonlinear equations*

The finite-amplitude of the perturbation in nonlinear stability is taken to be the counterpart of the real exponential term in (4.1): let $A(t)$ be the real amplitude of a finite-size perturbation such that $A(t) = \mathrm{e}^{at}$ holds for infinitesimal-amplitude perturbations (as in linear theory). Moreover, the frequency of the basic wave, ω, is allowed to depend on the amplitude of perturbation, i.e.

$$\omega \equiv \omega(A(t)). \tag{4.3}$$

Therefore, both the growth rate and the frequency of nonlinear perturbations change with the finite size of the perturbation. These two facts are embodied in the following transformation for 3D perturbations (Reynolds & Potter 1967):

$$\theta(x, z, \omega, t) = k_x x + k_z z + \Theta(\omega, t), \quad \Theta(\omega, t) = \omega(A)t, \quad A = A(t), \quad y = y, \tag{4.4}$$

which implies that

$$\frac{\partial \theta}{\partial t} \equiv \frac{\partial \Theta}{\partial t} = \omega + \frac{\mathrm{d}\omega}{\mathrm{d}A}\left(t\frac{\mathrm{d}A}{\mathrm{d}t}\right). \tag{4.5}$$

https://doi.org/10.1017/jfm.2012.549 Published online by Cambridge University Press

Using (4.4), the time and spatial derivatives in the (θ, A, y)-plane can be written as

$$\frac{\partial}{\partial t} \to \frac{\mathrm{d}A}{\mathrm{d}t}\frac{\partial}{\partial A} + \frac{\partial \Theta}{\partial t}\frac{\partial}{\partial \theta}, \tag{4.6}$$

$$\left(\frac{\partial}{\partial x}, \frac{\partial^2}{\partial x^2}, \frac{\partial}{\partial y}, \frac{\partial^2}{\partial y^2}, \frac{\partial}{\partial z}, \frac{\partial^2}{\partial z^2}\right) \to \left(k_x\frac{\partial}{\partial \theta}, k_x^2\frac{\partial^2}{\partial \theta^2}, \frac{\partial}{\partial y}, \frac{\partial^2}{\partial y^2}, k_z\frac{\partial}{\partial \theta}, k_z^2\frac{\partial^2}{\partial \theta^2}\right). \tag{4.7}$$

Equation (4.6) reveals the underlying two-time-scale ansatz of the Reynolds–Potter transformation (4.4): the first and second terms in (4.6) represent slow and fast time scales, respectively. In other words, while the perturbation amplitude $A(t)$ is a slowly varying function of time, its phase ($\theta \sim \Theta$ and $\mathrm{d}\Theta/\mathrm{d}t \sim \omega$) is a rapidly varying function of time. Therefore, our adopted approach for weakly nonlinear theory is equivalent to the well-known multiple-scale analysis of perturbation theory.

As an illustration of the above transformation (4.4), let us consider the nonlinear perturbation equation for the balance of mass:

$$\frac{\partial \phi'}{\partial t} = -\left[u^0\frac{\partial \phi'}{\partial x} + \phi^0\frac{\partial u'}{\partial x} + \phi^0\frac{\partial v'}{\partial y} + \phi^0\frac{\partial w'}{\partial z}\right] - \left[\frac{\partial(\phi' u')}{\partial x} + \frac{\partial(\phi' v')}{\partial y} + \frac{\partial(\phi' w')}{\partial z}\right]. \tag{4.8}$$

This equation is transformed, using (4.6)–(4.7), into

$$\left(\frac{\mathrm{d}A}{\mathrm{d}t}\frac{\partial}{\partial A} + \frac{\partial \Theta}{\partial t}\frac{\partial}{\partial \theta}\right)\phi' = \mathcal{L}^1 X + \mathcal{N}^1, \tag{4.9}$$

where $\mathcal{L}^1$ and $\mathcal{N}^1$ represent all linear and nonlinear terms, respectively, having following forms:

$$\mathcal{L}^1 X = \left(-u^0 k_x\frac{\partial}{\partial \theta}, -\phi^0 k_x\frac{\partial}{\partial \theta}, -\phi^0\frac{\partial}{\partial y}, -\phi^0 k_z\frac{\partial}{\partial \theta}, 0\right) X, \tag{4.10}$$

$$\mathcal{N}^1 = -k_x\left[\phi'\frac{\partial u'}{\partial \theta} + u'\frac{\partial \phi'}{\partial \theta}\right] - \left[\phi'\frac{\partial v'}{\partial y} + v'\frac{\partial \phi'}{\partial y}\right] - k_z\left[\phi'\frac{\partial w'}{\partial \theta} + w'\frac{\partial \phi'}{\partial \theta}\right]. \tag{4.11}$$

The rest of the equations are transformed accordingly. All five transformed nonlinear perturbation equations can be written compactly in operator form:

$$[\boldsymbol{\mathcal{M}} - \boldsymbol{\mathcal{L}}]\, X = \boldsymbol{\mathcal{N}}(X, \ldots, X), \tag{4.12}$$

where

$$\boldsymbol{\mathcal{L}} \equiv \boldsymbol{\mathcal{L}}(\partial_y, \partial_y^2, \partial_\theta, \partial_\theta^2; \phi^0, \ldots) = (\mathcal{L}^1, \mathcal{L}^2, \mathcal{L}^3, \mathcal{L}^4, \mathcal{L}^5)^{\mathrm{Tr}} \tag{4.13}$$

is the linear stability operator,

$$\boldsymbol{\mathcal{M}}(\partial_A, \partial_\theta; \omega) = \left[\frac{\mathrm{d}A}{\mathrm{d}t}\frac{\partial}{\partial A} + \frac{\partial \Theta}{\partial t}\frac{\partial}{\partial \theta}\right] \boldsymbol{I} \tag{4.14}$$

is a diagonal operator and

$$\boldsymbol{\mathcal{N}} \equiv (\mathcal{N}^1, \mathcal{N}^2, \mathcal{N}^3, \mathcal{N}^4, \mathcal{N}^5)^{\mathrm{Tr}} \tag{4.15}$$

is the nonlinear operator. In (4.9)–(4.11), (4.13) and (4.15), the superscripts $1, 2, \ldots, 5$ refer to terms originating from the continuity, x-momentum, y-momentum, z-momentum and granular energy equations, respectively.

Note in (4.12) that all perturbation hydrodynamic fields, $X(y, A, \theta)$, now depend on three independent variables: the wall-normal distance (y), the amplitude of perturbation

https://doi.org/10.1017/jfm.2012.549 Published online by Cambridge University Press

(A) and the instantaneous position in the cycle of the basic wave $[\theta = \theta(x, z, \omega, t)]$. Following previous works (Stuart 1960; Watson 1960; Reynolds & Potter 1967; Shukla & Alam 2011*a*,*b*), we separate out harmonic components of all perturbation fields by assuming a Fourier expansion in θ:

$$X(y, A, \theta) = X^{(k)}(y, A)\mathrm{e}^{\mathrm{i}k\theta} + \tilde{X}^{(k)}(y, A)\mathrm{e}^{-\mathrm{i}k\theta}, \tag{4.16}$$

where the summation is taken over all positive integers $k \geqslant 0$.

Substituting (4.16) into (4.12) and collecting the coefficients of $\mathrm{e}^{\mathrm{i}k\theta}$, we obtain an infinite set of coupled nonlinear partial differential equations for each Fourier amplitude $X^{(k)}(y, A) = (\phi^{(k)}, u^{(k)}, v^{(k)}, w^{(k)}, T^{(k)})^{\mathrm{Tr}}$:

$$(\boldsymbol{\mathcal{M}}_k - \boldsymbol{\mathcal{L}}_k)\, X^{(k)} = \boldsymbol{\mathcal{N}}(X^{(k)}, \ldots, X^{(k)}) \equiv \boldsymbol{\mathcal{N}}_{(k)}, \tag{4.17}$$

where the linear operator for the kth Fourier mode is

$$\boldsymbol{\mathcal{L}}_k \equiv \boldsymbol{\mathcal{L}}\left(\partial_y, \partial_y^2, \mathrm{i}k, -k^2; \phi^0, \ldots\right) = \left(\mathcal{L}_k^1, \mathcal{L}_k^2, \mathcal{L}_k^3, \mathcal{L}_k^4, \mathcal{L}_k^5\right)^{\mathrm{Tr}}, \tag{4.18}$$

the corresponding diagonal operator $\boldsymbol{\mathcal{M}}_k$ is

$$\boldsymbol{\mathcal{M}}_k \equiv \boldsymbol{\mathcal{M}}(\partial_A, \mathrm{i}k; \omega) = \left[\frac{\mathrm{d}A}{\mathrm{d}t}\frac{\partial}{\partial A} + \frac{\partial \Theta}{\partial t}\mathrm{i}k\right]\boldsymbol{I} \tag{4.19}$$

and the nonlinear operator for the kth Fourier mode is

$$\boldsymbol{\mathcal{N}}_{(k)} \equiv \boldsymbol{\mathcal{N}}\left(\partial_y, \partial_y^2, \mathrm{i}k, -k^2; \phi^0, \ldots\right) = \left(\mathcal{N}_{(k)}^1, \mathcal{N}_{(k)}^2, \mathcal{N}_{(k)}^3, \mathcal{N}_{(k)}^4, \mathcal{N}_{(k)}^5\right)^{\mathrm{Tr}}. \tag{4.20}$$

The boundary conditions are accordingly transformed into

$$\boldsymbol{\mathcal{B}}X^{(k)} = 0 \quad \text{at } y = \pm 1/2. \tag{4.21}$$

To illustrate how (4.17) is arrived at, we focus on the mass balance equation (4.9) which, upon using (4.16), takes the following form:

$$\left(\frac{\mathrm{d}A}{\mathrm{d}t}\frac{\partial}{\partial A} + \frac{\partial \Theta}{\partial t}\mathrm{i}k\right)\phi^{(k)} = \mathcal{L}_k^1 X^{(k)} + \mathcal{N}_{(k)}^1, \tag{4.22}$$

where the left-hand side represents one diagonal element of $\boldsymbol{\mathcal{M}}_k$, and

$$\mathcal{L}_k^1 X^{(k)} = (-u^0\mathrm{i}kk_x, -\phi^0\mathrm{i}kk_x, -\phi^0\frac{\partial}{\partial y}, -\phi^0\mathrm{i}kk_z, 0)X^{(k)}, \tag{4.23}$$

$$\begin{aligned}
\mathcal{N}_{(k)}^1 = &-\frac{\mathrm{i}k_x}{1+\delta_{k0}}\left[\phi^{(k-j)}ju^{(j)} + \tilde{\phi}^{(j)}(k+j)u^{(k+j)} - \phi^{(k+j)}j\tilde{u}^{(j)}\right.\\
&\left.+ u^{(k-j)}j\phi^{(j)} + \tilde{u}^{(j)}(k+j)\phi^{(k+j)} - u^{(k+j)}j\tilde{\phi}^{(j)}\right]\\
&-\frac{1}{1+\delta_{k0}}\left[\phi^{(k-j)}\frac{\partial v^{(j)}}{\partial y} + \tilde{\phi}^{(j)}\frac{\partial v^{(k+j)}}{\partial y} + \phi^{(k+j)}\frac{\partial \tilde{v}^{(j)}}{\partial y}\right.\\
&\left.+ v^{(k-j)}\frac{\partial \phi^{(j)}}{\partial y} + \tilde{v}^{(j)}\frac{\partial \phi^{(k+j)}}{\partial y} + v^{(k+j)}\frac{\partial \tilde{\phi}^{(j)}}{\partial y}\right]\\
&-\frac{\mathrm{i}k_z}{1+\delta_{k0}}\left[\phi^{(k-j)}jw^{(j)} + \tilde{\phi}^{(j)}(k+j)w^{(k+j)} - \phi^{(k+j)}j\tilde{w}^{(j)}\right.\\
&\left.+ w^{(k-j)}j\phi^{(j)} + \tilde{w}^{(j)}(k+j)\phi^{(k+j)} - w^{(k+j)}j\tilde{\phi}^{(j)}\right].
\end{aligned} \tag{4.24}$$

https://doi.org/10.1017/jfm.2012.549 Published online by Cambridge University Press

The factor $1/(1+\delta_{k0})$ in (4.24) arises from the product of two Fourier series in which the zeroth-order terms are multiplied by a factor 2; the summation over the dummy index j ($\geqslant 0$) is implied (Einstein's convention). Recall that the superscript and subscript k in (4.17)–(4.22) refers to a specific Fourier mode ($k \geqslant 0$) as defined in (4.16); other related details on superscript notations are given in § 4.3.

4.2. *Power-series expansion and Landau equation*

To make progress in solving the infinite set of partial differential equations (4.17), which are nonlinearly coupled, we focus on small-amplitude (but finite) waves such that a power series solution in the real amplitude $A(t)$ can be sought (Stuart 1960; Watson 1960):

$$X^{(k)}(A(t), y) = A^n(t) X^{[k;n]}(y) \quad \text{with } k \geqslant 0, n \geqslant 1, \tag{4.25}$$

where

$$X^{[k;n]}(y) = \left(\phi^{[k;n]}, u^{[k;n]}, v^{[k;n]}, w^{[k;n]}, T^{[k;n]}\right)^{\mathrm{Tr}} \tag{4.26}$$

represents the vector of spatially varying amplitude functions. Equation (4.25) is simply a Taylor series expansion in perturbation amplitude which helps to decouple the coupled system of nonlinear equations (4.17). In the dual superscript notation for $X^{[k;n]}$ in (4.25), the first index (k) refers to a particular Fourier mode and the second index (n) indicates the order of a particular term as $O(A^n)$. See § 4.3 for rules on superscript indices and different types of brackets/limiters.

It is evident from (4.22) that we need to postulate about the time derivatives of perturbation amplitude A and its frequency Θ. We expand $A^{-1}(\mathrm{d}A/\mathrm{d}t)$ as a power series in A:

$$A^{-1}\frac{\mathrm{d}A}{\mathrm{d}t} = a^{(0)} + Aa^{(1)} + A^2 a^{(2)} + \cdots = A^n a^{(n)}, \tag{4.27}$$

since the solution of the linear part of (4.27) yields $A(t) \sim \mathrm{e}^{a^{(0)}t}$ (with $a^{(0)} = a$ being the real part of eigenvalue (growth rate) of the linear stability problem) as in linear theory that must be recovered for waves of infinitesimal-amplitudes $A \to 0$. Similarly, we can expand $\partial\Theta/\partial t$ as

$$\frac{\partial \Theta}{\partial t} \equiv \omega + \frac{\mathrm{d}\omega}{\mathrm{d}A}\left(t\frac{\mathrm{d}A}{\mathrm{d}t}\right) = b^{(0)} + Ab^{(1)} + A^2 b^{(2)} + \cdots = A^n b^{(n)}, \tag{4.28}$$

such that the frequency of the linear eigenvalue is recovered (i.e. $b^{(0)} = \omega$) in the limit of $A \to 0$.

Equations (4.27) and (4.28) are combined to yield the well-known Landau equation for complex amplitude $\mathcal{A} = A\exp(\mathrm{i}\Theta(t))$:

$$\frac{\mathrm{d}\mathcal{A}}{\mathrm{d}t} = c^{(0)}\mathcal{A} + c^{(1)}\mathcal{A}^2 + c^{(2)}\mathcal{A}^3 + \cdots, \tag{4.29}$$

where

$$c^{(n)} = a^{(n)} + \mathrm{i}b^{(n)} \tag{4.30}$$

are called Landau coefficients. It is worth pointing out that the Landau equation is *postulated* to hold in the amplitude expansion method (Stuart 1960; Watson 1960) in contrast to the centre manifold reduction (Carr 1981) wherein the Landau equation is derived from the evolution equation of the slow mode by taking its inner product

https://doi.org/10.1017/jfm.2012.549 Published online by Cambridge University Press

with the adjoint linear eigenfunction (Shukla & Alam 2009). This is one of the main differences between the direct method of centre manifold reduction and the indirect method of the amplitude expansion technique as employed in this paper. It was demonstrated by Shukla & Alam (2009, 2011*a*) that the first Landau coefficient obtained from the centre manifold reduction technique (Shukla & Alam 2009) exactly matches that obtained from the amplitude expansion technique (Shukla & Alam 2011*a*) for the gradient-banding problem. It has been verified that the above conclusion holds also for the general case of 3D perturbations.

4.3. *Modal equations for the* kth *harmonic at* $O(A^n)$*:* $X^{[k;n]}$

Inserting (4.25), (4.27) and (4.28) into (4.22) and equating the coefficients of A^n, we obtain modal equations for $\phi^{[k;m]}$:

$$(ma^{(n-m)} + \mathrm{i}kb^{(n-m)})\phi^{[k;m]} = L_k^1 X^{[k;n]} + N_{kn}^1, \tag{4.31}$$

where

$$L_k^1 X^{[k;n]} = \left(-u^0 \mathrm{i}kk_x, -\phi^0 \mathrm{i}kk_x, -\phi^0 \frac{\mathrm{d}}{\mathrm{d}y}, -\phi^0 \mathrm{i}kk_z, 0\right) X^{[k;n]}, \tag{4.32}$$

and

$$\begin{aligned} N_{kn}^1 = &-\frac{\mathrm{i}k_x}{1+\delta_{k0}}[\phi^{[k-j;n-m]} j u^{[j;m]} + \tilde{\phi}^{[j;n-m]}(k+j)u^{[k+j;m]} - \phi^{[k+j;n-m]} j\tilde{u}^{[j;m]} \\ &+ u^{[k-j;n-m]} j\phi^{[j;m]} + \tilde{u}^{[j;n-m]}(k+j)\phi^{[k+j;m]} - u^{[k+j;n-m]} j\tilde{\phi}^{[j;m]}] \\ &- \frac{1}{1+\delta_{k0}}\left[\phi^{[k-j;n-m]}\frac{\mathrm{d}v^{[j;m]}}{\mathrm{d}y} + \tilde{\phi}^{[j;n-m]}\frac{\mathrm{d}v^{[k+j;m]}}{\mathrm{d}y} + \phi^{[k+j;n-m]}\frac{\mathrm{d}\tilde{v}^{[j;m]}}{\mathrm{d}y}\right. \\ &\left. + v^{[k-j;n-m]}\frac{\mathrm{d}\phi^{[j;m]}}{\mathrm{d}y} + \tilde{v}^{[j;n-m]}\frac{\mathrm{d}\phi^{[k+j;m]}}{\mathrm{d}y} + v^{[k+j;n-m]}\frac{\mathrm{d}\tilde{\phi}^{[j;m]}}{\mathrm{d}y}\right] \\ &- \frac{\mathrm{i}k_z}{1+\delta_{k0}}[\phi^{[k-j;n-m]} j w^{[j;m]} + \tilde{\phi}^{[j;n-m]}(k+j)w^{[k+j;m]} - \phi^{[k+j;n-m]} j\tilde{w}^{[j;m]} \\ &+ w^{[k-j;n-m]} j\phi^{[j;m]} + \tilde{w}^{[j;n-m]}(k+j)\phi^{[k+j;m]} - w^{[k+j;n-m]} j\tilde{\phi}^{[j;m]}]. \end{aligned} \tag{4.33}$$

In (4.33), Einstein's summation convention is implied for dummy indices j and m. To change the second index of $\phi^{[k;m]}$ on the left-hand side of (4.31) from $[k;m]$ to $[k;n]$ as well as to simplify algebraic manipulations of modal equations, we now adopt a set of rules to specify the superscript and bracket notation as in our previous work (Shukla & Alam 2011*a*,*b*):

$$(n) \Rightarrow n \geqslant 0, \quad [n] \Rightarrow n \geqslant 1 \quad \text{and} \quad \{n\} \Rightarrow n \geqslant 2, \tag{4.34}$$

where the type of bracket/delimiter, ( ) or { } or [ ], determines the lower bound on its index. For the latter two brackets, the following dual-index notation is adopted:

$$[k;n] \Rightarrow k \geqslant 0, \quad n \geqslant 1, \tag{4.35}$$

$$\{k;n\} \Rightarrow k \geqslant 1, \quad n \geqslant 2, \tag{4.36}$$

where the first index (k) is bounded by the second index (n), i.e. $n \geqslant k$. For the dual-index notation too, the lower bound on any index, which is greater than or equal to zero, depends on the type of bracket/delimiter as in (4.34).

https://doi.org/10.1017/jfm.2012.549 Published online by Cambridge University Press

Following index notation (4.34)–(4.36), the left-hand side of (4.31) can be rewritten as

$$\begin{aligned}(ma^{(n-m)} + \mathrm{i}kb^{(n-m)})\phi^{[k;m]} &= (na^{(0)} + \mathrm{i}kb^{(0)})\phi^{[k;n]} + (ma^{[n-m]} + \mathrm{i}kb^{[n-m]})\phi^{[k;m]} \\ &= (na^{(0)} + \mathrm{i}kb^{(0)})\phi^{[k;n]} + (a^{[n-1]} + \mathrm{i}kb^{[n-1]})\phi^{[k;1]} \\ &\quad + (ma^{[n-m]} + \mathrm{i}kb^{[n-m]})\phi^{\{k;m\}} \\ &= (na^{(0)} + \mathrm{i}kb^{(0)})\phi^{[k;n]} + (a^{[n-1]} + \mathrm{i}b^{[n-1]})\phi^{[1;1]}\delta_{k1} \\ &\quad + (ma^{[n-m]} + \mathrm{i}kb^{[n-m]})\phi^{\{k;m\}}. \end{aligned} \tag{4.37}$$

Now substituting (4.37) into (4.31) and rearranging terms, we obtain:

$$\begin{aligned}(na^{(0)} + \mathrm{i}kb^{(0)})\phi^{[k;n]} - L_k^1 X^{[k;n]} &= -(a^{[n-1]} + \mathrm{i}b^{[n-1]})\phi^{[1;1]}\delta_{k1} \\ &\quad - (ma^{[n-m]} + \mathrm{i}kb^{[n-m]})\phi^{\{k;m\}} + \frac{E_{kn}^1}{(1+\delta_{k0})} + F_{kn}^1, \end{aligned} \tag{4.38}$$

where E_{kn}^1 refers to quadratic nonlinearities in the mass balance equation such that

$$E_{kn}^1 = N_{kn}^1(1+\delta_{k0}), \tag{4.39}$$

and F_{kn}^1 refers to additional nonlinear terms that involve cubic- and higher-order nonlinearities and is zero for the mass balance equation (i.e. $F_{kn}^1 = 0$). The other four perturbation equations are similarly reduced to the form (4.38), except that the cubic- and higher-order nonlinearities are non-zero for momentum and granular energy balance equations.

Combining all five perturbation equations of the form (4.38), we obtain an infinite set of inhomogeneous equations for modal amplitude $X^{[k;n]} = [\phi^{[k;n]}, u^{[k;n]}, v^{[k;n]}, w^{[k;n]}, T^{[k;n]}]^{\mathrm{T}}$:

$$\boldsymbol{L}_{kn}X^{[k;n]} = -c^{[n-1]}X^{[1;1]}\delta_{k1} + G_{kn}, \tag{4.40}$$

where $\boldsymbol{L}_{kn}$ is a linear operator given by

$$\boldsymbol{L}_{kn} = \left(na^{(0)} + \mathrm{i}kb^{(0)}\right)\boldsymbol{I} - \boldsymbol{L}_k, \tag{4.41}$$

$$\boldsymbol{L}_k \equiv \boldsymbol{\mathcal{L}}(\partial_y \to \mathrm{d}_y, \partial_y^2 \to \mathrm{d}_y^2, \mathrm{i}k, -k^2, \phi^0, \ldots), \tag{4.42}$$

the Landau coefficients are denoted by $c^{[n-1]} = a^{[n-1]} + \mathrm{i}b^{[n-1]}$, and

$$\begin{aligned} G_{kn} &\equiv (G_{kn}^1, G_{kn}^2, G_{kn}^3, G_{kn}^4, G_{kn}^5)^{\mathrm{Tr}} \\ &= -\left(ma^{[n-m]} + \mathrm{i}kb^{[n-m]}\right)X^{\{k;m\}} + \frac{E_{kn}}{(1+\delta_{k0})} + F_{kn} \end{aligned} \tag{4.43}$$

represents a sum of linear and nonlinear (E_{kn} and F_{kn}) terms. The expression for $F_{kn} = (0, F_{kn}^2, F_{kn}^3, F_{kn}^4, F_{kn}^5)^{\mathrm{Tr}}$ involves the product of three or more Fourier series and has been obtained following a similar procedure to that we have illustrated for the expression for E_{kn}^1 ((4.33) and (4.39)). The above system of equations (4.40) is supplemented with the following boundary conditions

$$\boldsymbol{B}X^{[k;n]} = \mathrm{diag}(0, 1, 1, \mathrm{d}_y, \mathrm{d}_y)X^{[k;n]} = 0 \quad \text{at } y = \pm 1/2. \tag{4.44}$$

Equation (4.40) with boundary conditions (4.44) must be solved to analyse the nonlinear stability of granular Couette flow that also involves the solution for Landau coefficients. It is straightforward to verify that $G_{kn} = 0$ when $(k+n)$ is odd, and hence $c^{[n-1]}$ vanishes for even $n = 2, 4, 6, \ldots$. The non-zero Landau coefficients appear in the modal equations for the distortion to the fundamental mode at odd-orders in

https://doi.org/10.1017/jfm.2012.549 Published online by Cambridge University Press

$O(A) \rightarrow$	$O(A^2) \rightarrow$	$O(A^3) \rightarrow$	$O(A^4) \rightarrow$	$O(A^5) \rightarrow$
	$X^{[0;2]}$		$X^{[0;4]}$	
$X^{[1;1]}$		$c^{[2]}, X^{[1;3]}$		$c^{[4]}, X^{[1;5]}$
	$X^{[2;2]}$		$X^{[2;4]}$	
		$X^{[3;3]}$		$X^{[3;5]}$
			$X^{[4;4]}$	

TABLE 1. Ordered sequence of modal amplitude functions ($X^{[k;n]}$) and Landau coefficients.

perturbation amplitude:

$$\boldsymbol{L}_{1n} X^{[1;n]} = -c^{[n-1]} X^{[1;n]} + G_{1n}. \tag{4.45}$$

With the assumption of small growth rate, the solvability condition for (4.45) yields the following expression for Landau coefficients (Shukla & Alam 2011*a*,*b*):

$$c^{[n-1]} = a^{[n-1]} + \mathrm{i}b^{[n-1]} = \frac{\langle X^{\dagger}, G_{1n}\rangle}{\langle X^{\dagger}, X^{[1,1]}\rangle} = \frac{\displaystyle\int_{-1/2}^{1/2} \tilde{X}^{\dagger} G_{1n}\,\mathrm{d}y}{\displaystyle\int_{-1/2}^{1/2} \tilde{X}^{\dagger} X^{[1;1]}\,\mathrm{d}y}, \tag{4.46}$$

where $\tilde{X}^{\dagger}$ is the complex conjugate of the adjoint eigenfunction as defined in (3.14).

5. Numerical schemes for three types of problem

In § 4, we have reduced the nonlinear stability problem (3.4) to a sequence of linear inhomogeneous differential equations (4.40) for $X^{[k;n]}$ and each of which can be solved sequentially if we know the Landau coefficients $c^{[n-1]}$ along the way. Table 1 shows the ordered sequence of harmonics that must be calculated at different orders in perturbation amplitude. For example, to calculate the first Landau coefficient $c^{(2)}$, we need to evaluate: (i) the fundamental mode $X^{[1;1]}$; (ii) the distortion to the mean flow $X^{[0;2]}$; and (iii) the second harmonic $X^{[2;2]}$. The evaluation of: (iv) the distortion to the fundamental mode $X^{[1;3]}$; and (v) the third harmonic $X^{[3;3]}$ completes our work up to cubic-order, see table 1. In a companion paper on vorticity-banding instability (Shukla & Alam 2012), we also evaluated the second Landau coefficient $c^{(4)}$ that requires solutions of all harmonics up to quartic-order $O(A^4)$, see table 1; however, that problem has been tackled analytically.

A spectral-based numerical method has been developed to solve the modal equations (Shukla & Alam 2011*a*,*b*) which has been modified to account for 3D perturbations in the present paper. Depending on the particular choice of the index values in (4.40), we can divide the numerical method into three categories:

(i) type-1 problem: $k = n = 1$;
(ii) type-2 problem: $k \neq 1$ and $n \geqslant k$;
(iii) type-3 problem: $k = 1$ and $n > 1$.

While the type-1 problem corresponds to a differential eigenvalue problem, the type-2 and type-3 problems involve solutions of inhomogeneous differential equations with or without solvability condition (4.46). A brief description of the numerical scheme for each of these problems is given below.

https://doi.org/10.1017/jfm.2012.549 Published online by Cambridge University Press

5.1. *Type-1: generalized eigenvalue problem* $\boldsymbol{L}X = c^{(0)}\boldsymbol{K}X$

Substituting $k = n = 1$ into (4.40) we get a generalized differential eigenvalue problem

$$\boldsymbol{L}_1\left(\mathrm{d}_y^2, \mathrm{d}_y; \ldots\right) X^{[1;1]} = c^{(0)} X^{[1;1]}, \tag{5.1}$$

which must be numerically solved along with homogeneous boundary conditions:

$$\boldsymbol{B}X^{[1;1]} = \mathrm{diag}(0, 1, 1, \mathrm{d}_y, \mathrm{d}_y) X^{[1;1]} = 0 \quad \text{at } y = \pm 1/2. \tag{5.2}$$

The solution of (5.1)–(5.2) yields the linear eigenfunction $X^{[1;1]}$ and the corresponding eigenvalue $c^{(0)}$. The adjoint system of differential equations (3.14), which is of the same form as (5.1), must also be solved simultaneously to obtain the adjoint eigenfunction $X^{\dagger}$ and its adjoint eigenvalue.

All five ordinary differential equations of (5.1) have been discretized along the y-direction by implementing the staggered-grid spectral collocation method that uses Chebyshev polynomials (Canuto *et al.* 1988; Alam & Nott 1998; Shukla & Alam 2011*a*) as basis functions. More specifically, the mass balance equation is collocated at Gauss points:

$$\xi_{j+1/2} = \cos\left(j + \frac{1}{2}\right)\frac{\pi}{M}, \quad j = 0, \ldots M-1, \tag{5.3}$$

which are the zeros of the Chebyshev polynomial of degree M, denoted by $\mathcal{T}_M(\xi)$. Note that the Gauss points (5.3) do not include two boundary points and hence we do not need to implement any 'artificial' boundary condition for density (Alam & Nott 1998). On the other hand, the momentum and granular energy equations are collocated at Gauss–Lobatto points:

$$\xi_j = \cos\left(\frac{j\pi}{M}\right) \quad \text{where } j = 0, \ldots, M, \tag{5.4}$$

which are the extrema of the Mth-order Chebyshev polynomial. The physical domain in the present problem is $(-1/2, 1/2)$, thus we assume a transformation $\xi = 2y \in (-1, 1)$ which transforms the variables from the physical grid (y) to the spectral grid (ξ).

The unknown variables are next expanded in terms of Chebyshev polynomials of degree M, subject to the constraint that the error is exactly zero at collocation points. This is equivalent to expanding the unknown variables in terms of their values at the collocation points via the respective Lagrange interpolation polynomials. Therefore the unknown variables at Gauss and Gauss–Lobatto points can be represented by

$$\phi(\xi) = \sum_{j=1}^{M-1} \mathcal{G}_j(\xi)\phi(\xi_{j+1/2}), \tag{5.5}$$

$$f(\xi) = \sum_{j=0}^{M} \mathcal{F}_j(\xi) f(\xi_j), \tag{5.6}$$

respectively, where the interpolation polynomials are

$$\mathcal{G}_j(\xi) = \frac{(-1)^j\sqrt{(1-\xi_j^2)}\mathcal{T}_M(\xi)}{M(\xi - \xi_j)}, \tag{5.7}$$

https://doi.org/10.1017/jfm.2012.549 Published online by Cambridge University Press

$$\mathcal{F}_j(\xi) = \frac{(-1)^{j+1}(1-\xi^2)\mathcal{T}'_M(\xi)}{c_j M^2(\xi - \xi_j)}, \tag{5.8}$$

with $c_0 = c_M = 1$ and $c_j = 2$ for $0 < j < M$ and $\mathcal{T}'_M(\xi) = \mathrm{d}\mathcal{T}_M(\xi)/\mathrm{d}\xi$. Note that $\mathcal{G}_j(\xi_{k+1/2}) = \delta_{jk}$ and $\mathcal{F}_j(\xi_k) = \delta_{jk}$ as required by the constraint imposed in the collocation scheme. The derivatives of unknown variables are similarly obtained by differentiating (5.5)–(5.6).

In the discretized continuity equation at Gauss points, the density field is represented at Gauss points [i.e. $\phi(\xi_{j+1/2})$], but the other variables (velocities and granular temperature, which are also represented at Gauss points) must be transferred to Gauss–Lobatto points, i.e.

$$(u, v, w, T)(\xi_{j+1/2}) \to (u, v, w, T)(\xi_j). \tag{5.9}$$

Similarly, the discretization of momentum and energy equations at Gauss–Lobatto points requires the density field to be transferred from the Gauss–Lobatto points to Gauss points [i.e. $\phi(\xi_j) \to \phi(\xi_{j+1/2})$]. To achieve this transfer of variables in the staggered-collocation scheme, we need to construct interpolation polynomials from Gauss variables to Gauss–Lobatto variables and vice versa via the following transformation:

$$\phi(\xi_k) = \sum_{j=0}^{M-1} \mathcal{P}_j(\xi_k)\phi(\xi_{j+1/2}) \quad \text{for } k = 0, \ldots, M, \tag{5.10}$$

$$f(\xi_{k+1/2}) = \sum_{j=0}^{M} \mathcal{Q}_j(\xi_{k+1/2}) f(\xi_j) \quad \text{for } k = 0, \ldots, M-1. \tag{5.11}$$

Here $\mathcal{P}_j(\xi_i)$ is the interpolation matrix (of order M by $M-1$) from Gauss point to Gauss–Lobatto point and $\mathcal{Q}_j(\xi_{i+1/2})$ is the interpolation matrix (of order $M-1$ by M) from Gauss–Lobatto point to Gauss point as given by:

$$\mathcal{P}_j(\xi_k) = \frac{(-1)^{j+k}\sqrt{(1-\xi_j^2)}}{M(\xi_k - \xi_j)}, \tag{5.12}$$

$$\mathcal{Q}_j(\xi_{k+1/2}) = \frac{(-1)^{k+j+1}\sqrt{1-\xi_{k+1/2}^2}}{c_j M(\xi_{k+1/2} - \xi_j)}. \tag{5.13}$$

Using the above spectral discretization scheme, the differential equations of the eigenvalue problem (5.1) are transformed into a generalized matrix eigenvalue problem:

$$\boldsymbol{L}X = c^{(0)}\boldsymbol{K}X, \tag{5.14}$$

where $\boldsymbol{L}$ and $\boldsymbol{K} = \boldsymbol{I}$ are square matrices of order $(5M+4)$, with M being the degree of the Chebyshev polynomial, and

$$X = \left(\phi(\xi_{j+1/2}), u(\xi_k), v(\xi_k), w(\xi_k), T(\xi_k)\right)^{\mathrm{Tr}}, \tag{5.15}$$

with $j = 0, \ldots, M-1$ and $k = 0, \ldots, M$, is the discrete representation of the linear eigenfunction $X^{[1;1]}$. We have chosen the second to fifth and $(5M+4)$th to $(5M-1)$th rows to enforce the velocity $[(u, v, \mathrm{d}_y w) = 0$ at $y \pm 1/2]$ and the heat flux $[\mathrm{d}_y T = 0$ at $y = \pm 1/2]$ boundary conditions. The rows of matrix $\boldsymbol{K}$ that corresponds to boundary

https://doi.org/10.1017/jfm.2012.549 Published online by Cambridge University Press

conditions contain zeros and hence this matrix is singular. The singularity of $\boldsymbol{K}$ has been removed by using row and column operations that reduce the rank of the matrices $\boldsymbol{L}$ and $\boldsymbol{K}$. The resultant order of the matrix eigenvalue problem is $(5M-4)$ which has been solved by the QZ-algorithm of MATLAB software.

5.2. *Type-2: solution of* $\boldsymbol{AX}=\boldsymbol{b}$

The general form of the equation for $k\neq 1$ and $n\geqslant k$)namely (4.40)) can be written as $\boldsymbol{L}_{kn}X^{[k;n]}=\boldsymbol{G}_{kn}$ which at $O(A^2)$ leads to two equations:

$$\boldsymbol{L}_{02}\left(\mathrm{d}_y^2,\mathrm{d}_y;\ldots\right)X^{[0;2]}=G_{02}\left(\mathrm{d}_y^2,\mathrm{d}_y;X^{[1;1]},\tilde{X}^{[1;1]}\right), \tag{5.16}$$

$$\boldsymbol{L}_{22}\left(\mathrm{d}_y^2,\mathrm{d}_y;\ldots\right)X^{[2;2]}=G_{22}\left(\mathrm{d}_y^2,\mathrm{d}_y;X^{[1;1]},X^{[1;1]}\right), \tag{5.17}$$

for the distortion to the mean flow ($X^{[0;2]}$) and the second harmonic ($X^{[2;2]}$), respectively, which are needed to calculate the first Landau coefficient (see table 1).

Each of the above inhomogeneous systems of ordinary differential equations (5.16)–(5.17) is discretized using the same staggered-grid spectral collocation method as explained in § 5.1: the continuity equation is evaluated at Gauss points and the other equations are at Gauss–Lobatto points. The resulting set of algebraic equations along with boundary conditions can be put into the form:

$$\boldsymbol{AX}=\boldsymbol{b}, \tag{5.18}$$

where X is the discrete version (5.15) of the respective modal amplitude function ($X^{[0;2]}$ or $X^{[2;2]}$). Owing to the global nature of the spectral scheme, the coefficient matrix $\boldsymbol{A}$ is dense, unstructured, unsymmetric and ill-conditioned. We have employed the method of singular-value decomposition (Trefethen & Bau 1997) to solve (5.18) for all cases.

5.3. *Type-3: solution of* $\boldsymbol{AX}=cX+\boldsymbol{b}$

The general form for the type-3 problem is given by

$$\boldsymbol{AX}=cX+\boldsymbol{b} \tag{5.19}$$

that results from (4.40) for $k=1$ and $n>1$, leading to (4.45). Here the first part of the computations is related to evaluating the first Landau coefficient $c^{(2)}$ that involves the ratio of two definite integrals as defined in (4.46). These integrals are evaluated using a Gauss–Chebyshev quadrature scheme which is simply the standard Gaussian quadrature that uses Chebyshev polynomials as interpolating polynomials. More specifically, we first calculate each integrand at Gauss–Lobatto points and then take the weighted summation using the following quadrature formula:

$$\int_{-1/2}^{1/2}f(y)\,\mathrm{d}y=\frac{1}{2}\int_{-1}^{1}f(\xi)\,\mathrm{d}\xi=\frac{1}{2}\sum_{j=0}^{M}w(\xi_j)f(\xi_j), \tag{5.20}$$

where the mapping $\xi=\xi(y)=2y$ has been used to transform the physical domain $y\in(-1/2,1/2)$ to the Chebyshev domain $\xi\in(-1,1)$. The spectral weights $w(\xi_j)$ are given by Shukla & Alam (2011*a*):

$$w(\xi_j)=\frac{b_j}{M}\left\{2+\sum_{\alpha=2}^{M}c_\alpha\frac{1+(-1)^\alpha}{1-\alpha^2}\cos\left(\frac{\alpha j\pi}{M}\right)\right\}, \tag{5.21}$$

where $b_0=b_M=1/2$ and $b_j=1$ for $1\leqslant j<M$. It has been verified (Shukla & Alam 2011*a*) that the Gauss–Chebyshev quadrature converges with much fewer grid points

https://doi.org/10.1017/jfm.2012.549 Published online by Cambridge University Press

than the conventional (Simpson and trapezoidal) quadrature formula. The spectral accuracy of the Gauss–Chebyshev quadrature scheme (Canuto *et al.* 1988; Shukla & Alam 2011*a*) is responsible for its superior convergence.

After calculating the first Landau coefficient $c^{(2)}$, the equation for the distortion to the fundamental mode (4.45) with $k = 1$ and $n = 3$ can be put into form

$$\left(\boldsymbol{L}_{13} + c^{(2)}\boldsymbol{I}\right) X^{[1;3]} = G_{13}, \tag{5.22}$$

which comprises second-order ordinary differential equations that, upon spectral discretization using formulae as in § 5.1, takes the form of the type-2 problem, $\boldsymbol{A}X = \boldsymbol{b}$, as discussed in § 5.2. The numerical solution of (5.22), along with the third harmonic from $\boldsymbol{L}_{33}X^{[3;3]} = G_{33}$, provides the complete solution of the nonlinear stability problem up to cubic-order $O(A^3)$ (see table 1).

6. Analysis of the cubic Landau equation: bifurcation and nonlinear patterns

6.1. *Equilibrium amplitude and the nature of bifurcation*

Separating the real and imaginary parts of the complex Landau–Stuart equation (4.29) at cubic-order, we obtain

$$\frac{\mathrm{d}A}{\mathrm{d}t} = a^{(0)}A + a^{(2)}A^3, \tag{6.1}$$

$$\frac{\mathrm{d}\Theta}{\mathrm{d}t} = \omega + \frac{\mathrm{d}\omega}{\mathrm{d}A}\left(t\frac{\mathrm{d}A}{\mathrm{d}t}\right) = b^{(0)} + b^{(2)}A^2. \tag{6.2}$$

The equilibrium amplitude, $A(t) = A_e$, is obtained by substituting $\mathrm{d}A/\mathrm{d}t = 0$ in (6.1) which yields a trivial solution, $A_e = 0$, that represents the uniform shear base flow, and two nonlinear solutions with finite amplitudes

$$A_e = \pm\sqrt{-\frac{a^{(0)}}{a^{(2)}}}. \tag{6.3}$$

It is clear that the equilibrium solution (6.3) exists if and only if $a^{(0)}$ and $a^{(2)}$ have opposite signs. Therefore, for the *subcritical* ($a^{(0)} < 0$, i.e. stable according to linear theory) and *supercritical* ($a^{(0)} > 0$, i.e. linearly unstable) flows, the equilibrium amplitude exists if the real part of the first Landau coefficient is positive ($a^{(2)} > 0$) and negative ($a^{(2)} < 0$), respectively. In the supercritical regime, the linearly unstable uniform shear flow bifurcates at some threshold/critical value of the control parameter and gives birth to two stable nonlinear states (6.3) above the critical parameter. On the other hand, the linearly stable uniform shear flow in the subcritical regime coexists with two unstable nonlinear solutions (6.3) below the critical parameter; the related stable nonlinear solutions can be obtained from the quintic-order Landau equation that requires the calculation of second Landau coefficient.

Corresponding to cubic-order equilibrium amplitude (6.3), the equilibrium frequency, see (6.2), is given by

$$\omega \equiv \omega(A(t)) = b^{(0)} + b^{(2)}A_e^2. \tag{6.4}$$

The nature of bifurcation depends on the numerical value of this frequency term; two types of subcritical/supercritical bifurcations can be classified: (i) *pitchfork/stationary* bifurcation if $b^{(0)} = 0$; and (ii) *Hopf/oscillatory* bifurcation if $b^{(0)} \neq 0$. For the latter case of Hopf/oscillatory bifurcations, the solution trajectory in phase space represents

https://doi.org/10.1017/jfm.2012.549 Published online by Cambridge University Press

stable/unstable spirals (i.e. attractor/repeller), leading to stable/unstable limit cycles, respectively (Shukla & Alam 2011*b*).

Since the nonlinearities modify the frequency of perturbation, its phase velocity also changes. The equilibrium 'nonlinear' phase velocity can be defined as

$$c_{ph}^{e} = -\frac{\omega}{\sqrt{(k_x^2+k_z^2)}} = c_{ph} - \frac{b^{(2)}A_e^2}{\sqrt{(k_x^2+k_z^2)}}, \tag{6.5}$$

where $c_{ph} = -b^{(0)}/\sqrt{(k_x^2+k_z^2)}$ denotes linear phase velocity. Note that $c_{ph} = c_{ph}^{e} = 0$ for pitchfork bifurcations since $b^{(0)} = 0 = b^{(2)}$ for stationary modes.

In this paper, we restrict our calculations to only the first Landau coefficient which, of course, does not provide stable equilibrium solutions in the case of subcritical bifurcations. To obtain stable equilibrium solutions for the flows having subcritical bifurcations, we should calculate higher-order Landau coefficients which is beyond the scope of this paper (see, however, the companion paper on nonlinear vorticity banding Shukla & Alam 2012 that reports the second Landau coefficient by retaining up to quintic-order terms, which is tackled analytically).

6.2. *Nonlinear stationary and travelling wave patterns and symmetry*

At cubic-order in perturbation amplitude $O(A^3)$, the expression for the nonlinear disturbance field $X(A,\theta,y)$ can be written as

$$\begin{aligned} X &= A^2X^{[0;2]} + \left[\left(AX^{[1;1]}\mathrm{e}^{\mathrm{i}\theta} + A^2X^{[2;2]}\mathrm{e}^{2\mathrm{i}\theta} + A^3X^{[1;3]}\mathrm{e}^{\mathrm{i}\theta} + A^3X^{[3;3]}\mathrm{e}^{3\mathrm{i}\theta}\right) + \text{c.c.}\right] \\ &= A^2X^{[0;2]} + 2A\left[X_r^{[1;1]}\cos\theta - X_i^{[1;1]}\sin\theta\right] + 2A^2\left[X_r^{[2;2]}\cos 2\theta - X_i^{[2;2]}\sin 2\theta\right] \\ &\quad + 2A^3\left[X_r^{[1;3]}\cos\theta - X_i^{[1;3]}\sin\theta\right] + 2A^3\left[X_r^{[3;3]}\cos 3\theta - X_i^{[3;3]}\sin 3\theta\right], \end{aligned} \tag{6.6}$$

where $X^{[1;1]}$, $X^{[0;2]}$, $X^{[2;2]}$, $X^{[1;3]}$ and $X^{[3;3]}$ are the fundamental, the distortion of the mean flow, the second harmonic, the distortion of the fundamental and the third harmonic, respectively; the subscripts r and i refer to the real and imaginary parts of the vector-valued complex function $X^{[k;n]}$, respectively. Using θ-transformation (4.4) with $t = 0$ in (6.6), we finally obtain

$$\begin{aligned} X(x,y,z,t=0) &= A^2X^{[0;2]} + 2A\left[X_r^{[1;1]}\cos(k_xx+k_zz) - X_i^{[1;1]}\sin(k_xx+k_zz)\right] \\ &\quad + 2A^2\left[X_r^{[2;2]}\cos 2(k_xx+k_zz) - X_i^{[2;2]}\sin 2(k_xx+k_zz)\right] \\ &\quad + 2A^3\left[X_r^{[1;3]}\cos(k_xx+k_zz) - X_i^{[1;3]}\sin(k_xx+k_zz)\right] \\ &\quad + 2A^3\left[X_r^{[3;3]}\cos 3(k_xx+k_zz) - X_i^{[3;3]}\sin 3(k_xx+k_zz)\right], \end{aligned} \tag{6.7}$$

$$\begin{aligned} &= A^2X^{[0;2]} + 2A\left[X_r^{[1;1]}\cos 2\pi(x^*+z^*) - X_i^{[1;1]}\sin 2\pi(x^*+z^*)\right] \\ &\quad + 2A^2\left[X_r^{[2;2]}\cos 4\pi(x^*+z^*) - X_i^{[2;2]}\sin 4\pi(x^*+z^*)\right] \\ &\quad + 2A^3\left[X_r^{[1;3]}\cos 2\pi(x^*+z^*) - X_i^{[1;3]}\sin 2\pi(x^*+z^*)\right] \\ &\quad + 2A^3\left[X_r^{[3;3]}\cos 6\pi(x^*+z^*) - X_i^{[3;3]}\sin 6\pi(x^*+z^*)\right], \end{aligned} \tag{6.8}$$

where $k_x = 2\pi/\lambda_x$ and $k_z = 2\pi/\lambda_z$ and λ_x and λ_z are the wavelengths in the x- and z-directions, respectively;

$$x^* = \frac{x}{\lambda_x} \quad \text{and} \quad z^* = \frac{z}{\lambda_z} \tag{6.9}$$

https://doi.org/10.1017/jfm.2012.549 Published online by Cambridge University Press

$0 \leqslant e \leqslant 1$	Restitution coefficient
ϕ^0	Mean density (volume fraction of particles)
$H = \dfrac{\overline{h}}{\overline{d}}$	Couette gap (i.e. the gap between two moving plates in terms of particle diameter)
$k_x = \dfrac{2\pi}{\lambda_x}$	Streamwise wavenumber
$k_z = \dfrac{2\pi}{\lambda_z}$	Spanwise wavenumber
$c^{(0)} = a^{(0)} + \mathrm{i}b^{(0)}$	Linear eigenvalue, (3.7), (4.29), (5.1) and (5.14)
$c^{[2]} = a^{[2]} + \mathrm{i}b^{[2]}$	First Landau coefficient, (4.46)
$A(t)$	Amplitude (real) of perturbation, (4.3), (4.27) and (6.1)
A_e	Equilibrium amplitude of perturbation, (6.3)
c^e_{ph}	Equilibrium phase velocity, (6.5)
M	Degree of Chebyshev polynomials, (5.3) and (5.4)

TABLE 2. Summary of control and flow parameters.

are the normalized x- and z-directions, measured in terms of the corresponding wavelength, respectively. Note that (6.8) remains invariant under the transformation $x^* \to z^*$ and $z^* \to x^*$, i.e. (6.8) is symmetric in x^* and z^*. Because of this symmetry, the patterns look the same in both the (y, z^*)- and (y, x^*)-planes as observed from fixed x- and z-locations, respectively. Therefore, all patterns are shown in the (y, z^*)-plane at fixed x-locations.

6.3. *Control parameters*

There are five control parameters in this problem as summarized in the first five rows of table 2. Among these five control parameters, three parameters, H, k_x, k_z, depend on the geometry (dimensions) of the system; the other two, ϕ^0 (mean density) and e (restitution coefficient), are related to the state of the system and the properties of the material, respectively. The wavelengths corresponding to two wavenumbers k_x and k_z,

$$\lambda_x = \frac{\overline{\lambda}_x}{\overline{h}} \quad \text{and} \quad \lambda_z = \frac{\overline{\lambda}_z}{\overline{h}}, \tag{6.10}$$

set the streamwise ($\bar{l}_x = \overline{\lambda}_x$) and spanwise ($\bar{l}_z = \overline{\lambda}_z$) lengths of the Couette cell. In other words, if an instability exists for a specified combination of k_x and k_z (with a fixed Couette gap of H, i.e. the height of the Couette cell is specified), the dimensions of the Couette cell must satisfy $\bar{l}_x/\overline{h} \geqslant \lambda_x$ and $\bar{l}_z/\overline{h} \geqslant \lambda_z$ to accommodate this instability (for example, in particle simulations).

For numerical calculations with the spectral method, we have used Chebyshev polynomials of varying degrees $M = 50$–150 (i.e. the number of Gauss collocation points) that were found to be sufficient to obtain converged values for the eigenvalue and the first Landau coefficient. These are time-consuming calculations, and hence we have not done an exhaustive parametric study. Instead we followed our previous work (Alam 2006; Shukla & Alam 2011*b*) and chose four combinations of (ϕ^0, H)

https://doi.org/10.1017/jfm.2012.549 Published online by Cambridge University Press

Instability	Form of perturbation	Authors
Pure transverse (gradient banding)	$\frac{\partial}{\partial y}(\cdot) \neq 0,\ k_x = 0$	Shukla & Alam (2009, 2011*a*)
2D long-wave stationary and travelling	$\frac{\partial}{\partial y}(\cdot) \neq 0,\ k_x \sim 0$	Shukla & Alam (2011*b*)
2D dominant stationary and travelling	$\frac{\partial}{\partial y}(\cdot) \neq 0,\ k_x \sim O(1)$	Shukla & Alam (2011*b*)
Pure spanwise (vorticity banding)	$\frac{\partial}{\partial y}(\cdot) = 0,\ k_x = 0,\ k_z \neq 0$	Shukla & Alam (2012)
Three-dimensional (3D)	$\frac{\partial}{\partial y}(\cdot) \neq 0,\ k_x \neq 0,\ k_z \neq 0$	Alam & Shukla (2012); this paper

TABLE 3. Summary of instabilities in granular plane Couette flow.

that represent five types of instability modes in this flow and probed the effect of 3D perturbations on the resulting nonlinear states as discussed in the following section.

7. Results and discussion: 3D nonlinear states from pitchfork and Hopf bifurcations

As mentioned in the introductory section, the nonlinear states and patterns in 2D granular plane Couette flow have been probed by us (Shukla & Alam 2011*b*) recently. Table 3 summarizes all types of linear instability modes in this flow, along with the specific form of perturbations. Depending on the value of streamwise wavenumber (k_x), the instabilities in 2D flows can be classified as: (i) *gradient-banding* instability ($k_x = 0$, i.e. the perturbations are allowed only along the transverse (y) direction and hence they are called pure transverse perturbations) which is responsible for the banding of particles along the gradient/transverse (y) direction; (ii) stationary and travelling waves at $k_x \sim 0$ (*long waves*) whose origin is tied to the gradient-banding instability; and (iii) *dominant* stationary and travelling waves at $k_x = O(1)$ having the largest growth rate among all instabilities. While the gradient-banding instability arise from 1D perturbations, the latter two are 2D instabilities since they originate from 2D perturbations. The effects of 3D perturbations ($k_z \neq 0$) on these linear instability modes (Alam 2006) are briefly recalled at the beginning of § 7.1 from the linear stability viewpoint.

We would like to emphasize that the instabilities of granular plane Couette flow are specific to inelastic systems ($e \neq 1$) as demonstrated by Alam & Nott (1998) and Alam (2006) for 2D and 3D perturbations, respectively. Although the incompressible plane Couette flow (Drazin & Reid 1981) is known to be linearly stable at all Reynolds numbers (but there are finite-amplitude solutions that bifurcate from $Re = \infty$), its compressible counterpart (i.e. the plane Couette flow of a gas of elastic hard spheres) supports acoustic instabilities at supersonic Mach numbers (Malik, Alam & Dey 2006; Malik, Dey & Alam 2008), provided the Reynolds number is very large ($Re > 10^5$). The compressibility of the fluid is primarily responsible for these instabilities, and the underlying family of instability modes are called *Mack modes* (Mack 1984). We can

https://doi.org/10.1017/jfm.2012.549 Published online by Cambridge University Press

define an effective Reynolds number for our granular Couette flow problem:

$$Re = \frac{\rho_p \overline{u}_w \overline{h}}{\overline{\mu}} = H^2 \sqrt{f_5/f_2^2}, \tag{7.1}$$

where $H = \overline{h}/\overline{d}$ is the scaled Couette gap, and f_2 and f_5 are related to shear viscosity and collisional dissipation (see appendix A), respectively. Note that the shear rate is scaled out of Reynolds number (7.1) since the granular temperature depends quadratically on the shear rate in a shear flow. We have checked that $Re = O(10^4)$ or less for the range of parameters investigated in this paper; moreover, the Mach number belongs to the subsonic regime, ruling out the possibility of acoustic instability in granular Couette flow. Therefore, the Mack modes of the related elastic compressible Couette flow remain stable in our inelastic system, and all instabilities discussed below belong to inelastic ($e \neq 1$) plane Couette flow and vanish in the perfectly elastic limit ($e = 1$).

In the rest of this paper, we focus on the effect of 3D perturbations on the nonlinear stability, bifurcation and the resulting patterns for each of the above 2D instability modes as detailed in §§ 7.1 and 7.2 for moderately dense ($\phi^0 = 0.2$) and dense ($\phi^0 = 0.4$) flows, respectively. In addition, we probe the nonlinear saturation of two specific 3D instability modes (Alam 2006) in dilute ($\phi^0 < 0.1$) flows that have no analogue in 2D flows as detailed in § 7.3. For all instability modes, we have attempted to characterize the 3D motion on the cross-stream plane in terms of the fixed/critical/stationary points of the underlying flow field.

7.1. *Three-dimensional perturbations at moderate density ($\phi^0 = 0.2$)*

Figure 2(*a*) displays the zones of instability in the (k_x, k_z)-plane (grey-shaded regions) for a moderate mean density $\phi^0 = 0.2$, with a Couette gap of $H = 100$ and the restitution coefficient of $e = 0.8$. (This parameter combination was extensively probed by Shukla & Alam 2011*b* for nonlinear stability against 2D perturbations.) Note that the 2D perturbations correspond to the ($k_z = 0$)-axis in figure 2(*a*). There are two 'hills' of unstable regions above the ($k_z = 0$)-axis: one around $k_x \sim 0.55$ and the other around $k_x \sim 0.95$ representing stationary and travelling waves, respectively (see below). The outer boundary of each hill represents the contour of zero growth rate (i.e. the neutral/critical contour), and the growth rates are positive (negative) inside (outside) the neutral/critical contour. It may be noted that out of $(5M + 4)$ eigenvalues of (5.14), where M is the number of Gauss collocation points or the degree of the Chebyshev polynomials, we have considered the growth rate of the least-stable mode which is defined as the one having the maximum growth rate for given values of k_x and k_z:

$$a_l^{(0)} = \max a^{(0)}. \tag{7.2}$$

In the following, we drop the subscript l (that denotes the least-stable mode) and use $a^{(0)}$ to present results for the least-stable mode. The inset of figure 2(*a*) shows a magnified view of the same stability diagram for small streamwise wavenumbers ($k_x \sim 0$) – these long-wave instabilities and their nonlinear states are separately discussed in § 7.1.3.

The variation of the growth rate of the least-stable mode with streamwise wavenumber is shown in figure 2(*b*) for ten different spanwise wavenumbers, ranging from $k_z = 0$ to 5.2, with other parameters as in figure 2(*a*). For each spanwise wavenumber k_z, the maximum growth rate (over all k_x) corresponds to the first peak (that occurs at $k_x \approx 0.58$) – this is called the dominant peak that represents

https://doi.org/10.1017/jfm.2012.549 Published online by Cambridge University Press

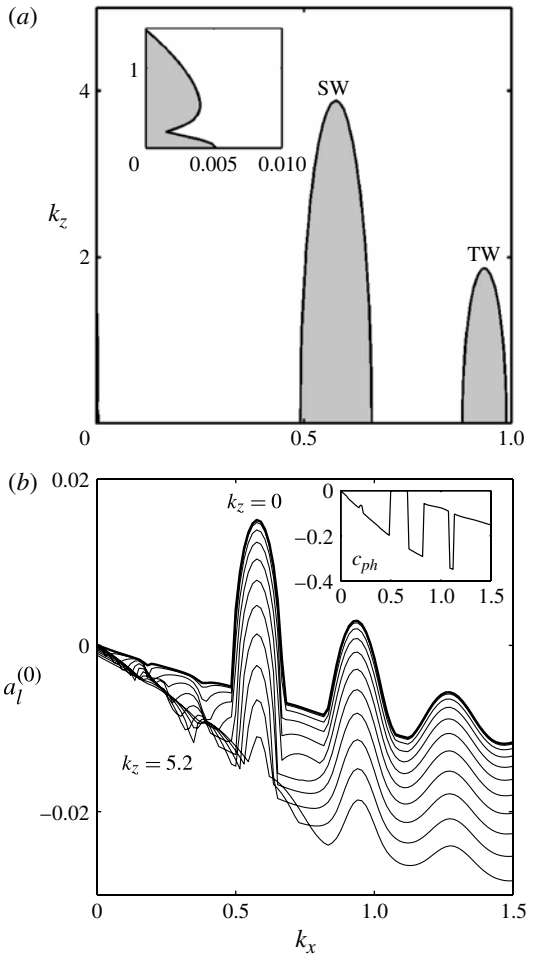


FIGURE 2. (*a*) Instability zones (grey-shaded) in the (k_x, k_z)-plane for $\phi^0 = 0.2$, $H = 100$ and $e = 0.8$; the inset shows a magnified part for small streamwise wavenumbers $k_x \sim 0$. (*b*) Variation of the growth rate of the least-stable mode with k_x for ten values of k_z in the range $k_z = (0, 5.2)$; the inset shows the variation of the phase velocity (of the backward travelling mode) with k_x for $k_z = 1$.

the stationary wave instability. The location of the dominant peak remains relatively unaltered with increasing k_z. The inset of figure 2(*b*) shows the variation of the phase velocity with k_x for $k_z = 1$ (the variation is similar for other values of k_z). The inset confirms that the instabilities corresponding to the first and second peaks in figure 2(*b*) (as well as the large and small hills, respectively, in figure 2*a*) represent stationary waves (SW) and travelling waves (TW), respectively. The second peak in figure 2(*b*) at $k_x \sim 1$ is dubbed dominant TWs since their growth rates are the largest among all TWs. The effect of k_z on the dominant TW instabilities mirrors that on the dominant SW instabilities. It is clear from figure 2(*b*) that the growth rates of both dominant SW and TW instabilities reach maximum for $k_z = 0$ and decreases with increasing k_z at any value of k_x; therefore, the origin of these two instability modes is tied to 2D perturbations (i.e. $k_z = 0$).

https://doi.org/10.1017/jfm.2012.549 Published online by Cambridge University Press

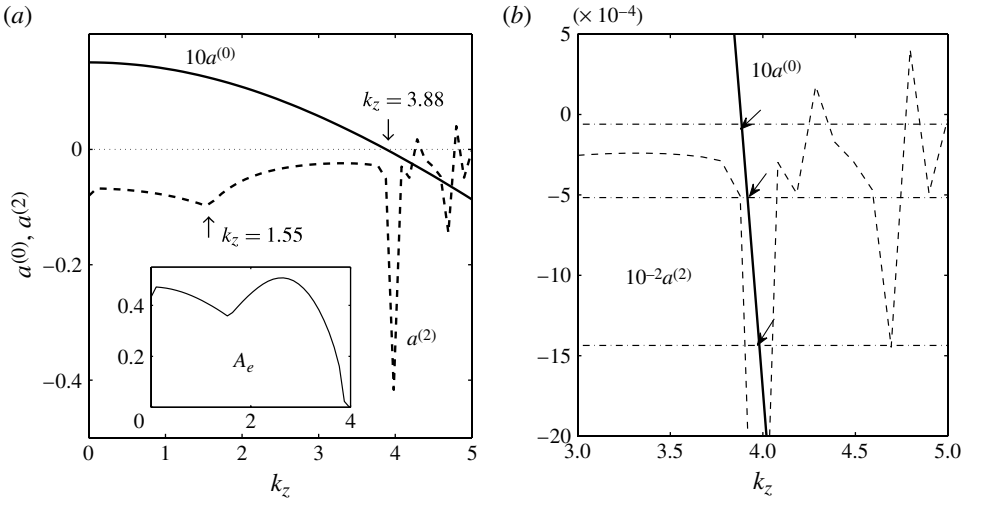


FIGURE 3. (*a*) Variation of $a^{(0)}$ (solid line), $a^{(2)}$ (dashed line), and A_e (inset), with k_z. The streamwise wavenumber, corresponding to the first peak of figure 2(*b*), is set to $k_x = 0.579$. The downward-arrow at $k_z = 3.88$ represents 'zero' growth rate. (*b*) $2a^{(0)}$ (solid line), $10^{-2}a^{(2)}$ (dashed line) and three eigenvalues of the mean-flow operators (horizontal dot-dashed lines). Other parameters are as in figure 2.

It is clear from the above discussion that the granular plane Couette flow admits three types of instabilities (dominant stationary and travelling instabilities, and long waves) at a moderate density of $\phi^0 = 0.2$, with a Couette gap of $H = 100$ and a restitution coefficient of $e = 0.8$. These are primarily 2D instabilities since the growth rate is positive and maximum for 2D perturbations. The effects of 3D perturbations on the nonlinear saturation of each of the above modes: (i) dominant stationary wave; (ii) dominant travelling wave; and (iii) long waves ($k_x \sim 0$), and the resulting nonlinear patterns are discussed in §§ 7.1.1–7.1.3, respectively. A concurrent focus is on analysing the cross-stream velocity and the streamwise vorticity fields of all instability modes.

7.1.1. *Dominant stationary instability: patterns with saddles, nodes and vortices*

Recall that the streamwise wavenumber for dominant stationary instability (corresponding to the first peak in figure 2*b*) is almost independent of the spanwise wavenumber and occurs at $k_x \approx 0.579$. Figure 3(*a*) shows the variations of the real parts of the growth rate of the least-stable mode (solid line) and that of the first Landau coefficient (dashed line), with k_z for $k_x = 0.579$, with other parameters as in figure 2(*b*). (The imaginary part of first Landau coefficient, $b^{(2)}$, is zero and so is its linear frequency $b^{(0)} = 0$, and hence they are not shown.) Since $a^{(0)} > 0$ and $a^{(2)} < 0$ for $k_z = [0, 3.9]$, the flow admits finite-amplitude equilibrium solutions $A_e = \sqrt{-a^{(0)}/a^{(2)}}$ and the bifurcation is supercritical for this range of spanwise wavenumbers. The corresponding variation of the equilibrium amplitude, A_e, with k_z is shown in the inset of figure 3(*a*). The nature of bifurcation in this case is of pitchfork-type since the underlying instabilities are stationary ($b^{(0)} = 0$). Note that the 2D flow (i.e. $k_z = 0$) admits supercritical bifurcations (Shukla & Alam 2011*b*) which remain supercritical with increasing three-dimensionality (i.e. increasing k_z) for a range of spanwise wavenumbers.

https://doi.org/10.1017/jfm.2012.549 Published online by Cambridge University Press

Before proceeding further, let us briefly recall the mean-flow resonance condition (Shukla & Alam 2011*b*) that occurs at quadratic-order, $O(A^2)$, in perturbation amplitude. By substituting $k = 0$ and $n = 2$ in (4.40), we obtain a set of equations for the mean-flow distortion ($X^{[0;2]}$) whose solution can be expressed as

$$X^{[0;2]} = \boldsymbol{L}_{02}^{-1} G_{02} = \left[2a^{(0)}\boldsymbol{I} - \boldsymbol{L}_0\right]^{-1} G_{02}, \tag{7.3}$$

where

$$\boldsymbol{L}_0 = \boldsymbol{L}(k_x = 0, k_z = 0) \tag{7.4}$$

is the linear stability operator for $k_x = 0 = k_z$. Equation (7.3) is solvable if and only if the mean-flow operator $\boldsymbol{L}_{02}$ is non-singular which happens if $2a^{(0)}$ is not an eigenvalue of $\boldsymbol{L}_0$. Therefore, the singularity/non-invertibility of $\boldsymbol{L}_{02}$ corresponds to the following condition:

$$2a^{(0)}(k_x, k_z) = a_j^{(0)}(k_x = k_z = 0) \quad \text{for } j = 1, 2, 3, \ldots. \tag{7.5}$$

When (7.5) is satisfied, a resonance occurs between the mean-flow distortion and a linear mode of the operator $\boldsymbol{L}_0$, and the signature of this appears as a discontinuity in the first Landau coefficient (Shukla & Alam 2011*b*).

It is seen in figure 3(*a*) that $a^{(2)}$ diverges near $k_z = 3.88$ (marked by the downward arrow) at the zero crossing of the growth rate curve; also, there are three additional points for $k_z > 4$ where $a^{(2)}$ is also diverging, resulting in kinks on the $a^{(2)}$-curve. Each of these kinks represents the mean-flow resonance condition (7.5) being satisfied there. To verify this assertion, we plot three eigenvalues of $\boldsymbol{L}_0$, denoted by three horizontal dot-dashed lines (and they represent 4th, 5th and 6th least-stable modes of $\boldsymbol{L}_0$), in figure 3(*b*); the solid line, representing the least-stable eigenvalue of the linear stability operator $\boldsymbol{L}$, intersects the dot-dashed lines at three points over a small range of spanwise wavenumbers $k_z \in (3.88, 4)$. The mean-flow resonance condition (7.5) is exactly satisfied at the intersection points of solid and dot-dashed lines; consequently, $a^{(2)}$ (dashed line) diverges at these specific values of k_z. It has been verified that the 3D flow admits mean-flow resonance at different k_z in the subcritical region (i.e. where the growth rate is negative). This conclusion reinforces our previous claim for 2D perturbations (Shukla & Alam 2011*b*).

The nonlinear patterns of perturbation density (ϕ'), as calculated from (6.8), for the dominant stationary instability for $k_x = 0.579$ and $k_z = 1$ are shown in the (y, z^*)-plane in figure 4(*b*) at three different streamwise locations, $x = 0$, $x = \lambda_x/2$ and $x = 3\lambda_x/4$, where $\lambda_x = 2\pi/k_x$ is the wavelength along the x-direction; other parameters are as in figure 3. On the grey scale, the white and black denote maximum and minimum values, respectively. Recall from § 6.3 that due to the symmetry of the perturbation fields (6.8) with respect to the interchange of x^* and z^* (where the starred coordinates are normalized by the respective wavelength), the 3D patterns would look the same in both (y, z^*)- and (y, x^*)-planes at fixed x- and z-locations, respectively. For a comparison, the corresponding 2D ($k_z = 0$) density pattern in the (x^*, y)-plane is displayed in figure 4(*a*) which should be compared with the 3D pattern in figure 4(*b*) at $x = 0$: both contain particle clusters that are primarily oriented at some oblique angle to the flow direction. However, the 3D patterns contain clusters of smaller sizes in contrast to those in 2D patterns. The granular temperature field in the (y, z^*)-plane at $x = 0$, shown in figure 4(*c*), possesses similar structural features to the corresponding density field. It must be noted that the true aspect ratio of each of these patterns can be ascertained by stretching the x- and z-axes in each panel by factor of $2\pi/k_x$ and $2\pi/k_z$, respectively.

https://doi.org/10.1017/jfm.2012.549 Published online by Cambridge University Press

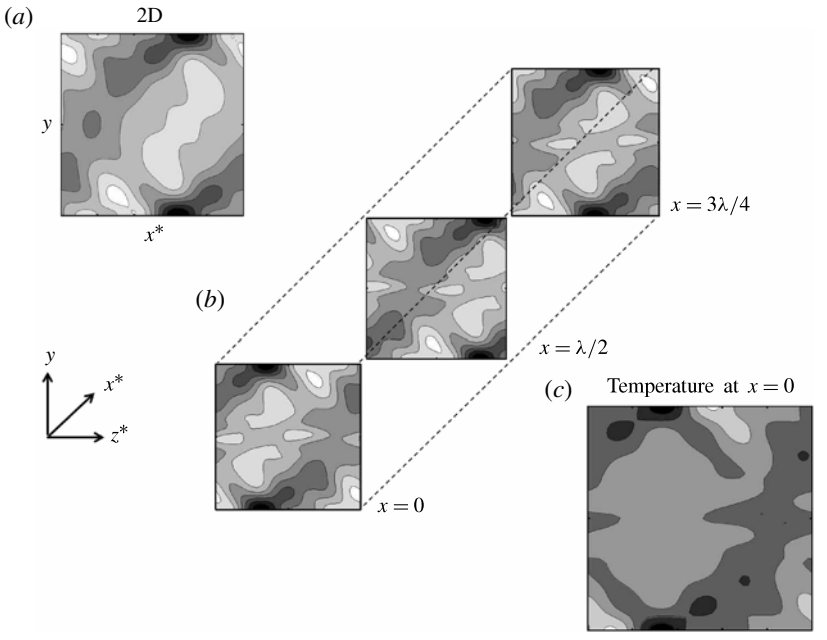


FIGURE 4. Nonlinear patterns of perturbation density for: (*a*) 2D ($k_z = 0$) flow in the (x^*, y)-plane; and (*b*) 3D ($k_z = 1$) flow in the (z^*, y)-plane at three different streamwise locations ($x = 0$, $\lambda_x/2$ and $3\lambda_x/4$). (*c*) Granular temperature in the (z^*, y)-plane at $x = 0$. Here $k_x = 0.579$ and other parameters are as in figure 3. On the grey scale, the white is maximum and the black minimum.

With parameter values as in figure 4(*b*), the vector map of the cross-stream velocity field (v', w') on the (y, z^*)-plane is displayed in figure 5(*a*) at the $x = 0$ location. We clearly observe: (i) a circulatory/vortical motion around $(y, z^*) \approx (0, 0.85)$, marked by a circle; (ii) two saddle points above and below the vortex located around $(y, z^*) \approx (0.25, 0.7)$ and $(y, z^*) \approx (-0.25, 0.92)$, respectively, each marked by curved arrows. (Each of these points represent a critical/fixed point of the planar velocity field; the critical or fixed or stationary points are synonymous in dynamical systems theory; Drazin 1992.) The curved arrows resemble hyperbolae and they corresponds to saddle points since two orbits approach the fixed point as $t \to \infty$ and the other two do so as $t \to -\infty$ (Drazin 1992). It is clear that the vortex at $(y, z^*) \approx (0, 0.85)$ is connected by the orbits of these two nearby saddle points. Note that this vortex is also surrounded by (iii) two sources: one at $(y, z^*) \approx (0, 0.3)$, marked by connected arrows, on its left and the other on its right (the same source is repeated on the right of the vortex due to the periodicity in z). In figure 5(*a*), we also find (iv) two 'imperfect' saddle points near two walls at $z^* \sim 0.3$; and (v) a sink around $(y, z^*) = (-0.15, 0.45)$. As expected, the sink is driven by the source and vice versa. A comparison between figure 5(*a*) and the density pattern in figure 4(*b*) (the first panel at $x = 0$) indicates that the source is located at a local density maximum, from which the particles are expelled, that possibly leads to the genesis of the sink at $(y, z^*) \approx (-0.15, 0.45)$ as well as other fixed points. Therefore, we may conclude that all the above described fixed points are intertwined with each other dynamically.

https://doi.org/10.1017/jfm.2012.549 Published online by Cambridge University Press

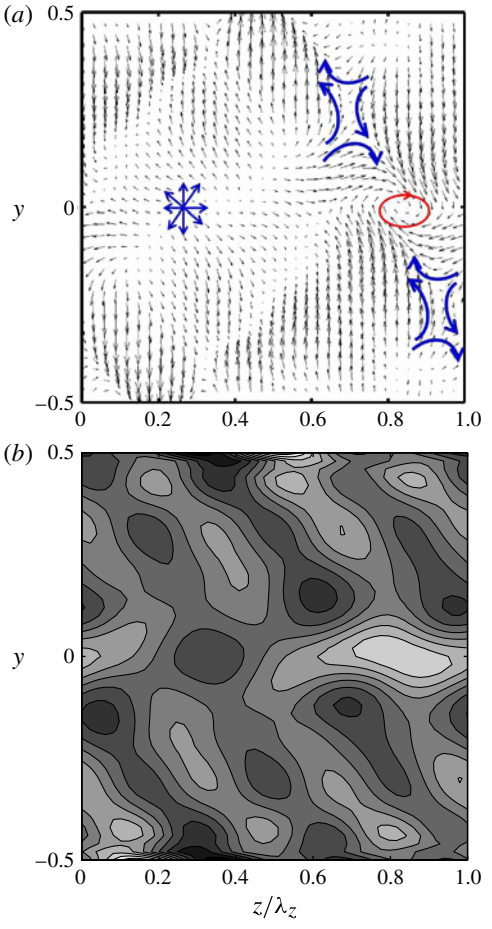


FIGURE 5. (Colour online) (*a*) Vector map of the nonlinear (v', w') velocity field at $x = 0$; and (*b*) contour grey-scale map (the white and black denote maximum and minimum, respectively) of the perturbation streamwise vorticity (Ω_x) at $x = 0$. Other parameters are as in figure 4(*b*).

Figure 5(*b*) shows a grey-scale map of the perturbation streamwise vorticity:

$$\Omega_x = \frac{\partial w'}{\partial y} - \frac{\partial v'}{\partial z} \tag{7.6}$$

at $x = 0$; on the grey scale, the white denotes maximum and the black minimum. Note that $\Omega_x = 0$ for 2D perturbations, and its non-zero value in 3D flows can be tied to the presence of streamwise vortical structures. It is seen that the location of the maximum Ω_x (the white region around $(y, z^*) = (0, 0.8)$ in figure 5*b*) corresponds to the location of the centre of the vortex in figure 5(*a*). Therefore, the maximum of the streamwise vorticity is correlated with the presence of a streamwise vortex in the (y, z^*)-plane. This correlation persists at any x-location, which is evident from figure 6(*a,b*). Note that the position of the vortex in the (y, z^*)-plane (marked by a closed circle in each panel) is different for different values of x; the corresponding locations of the maxima of Ω_x are indicated by an arrow in figure 6(*b*). We speculate that the presence of

https://doi.org/10.1017/jfm.2012.549 Published online by Cambridge University Press

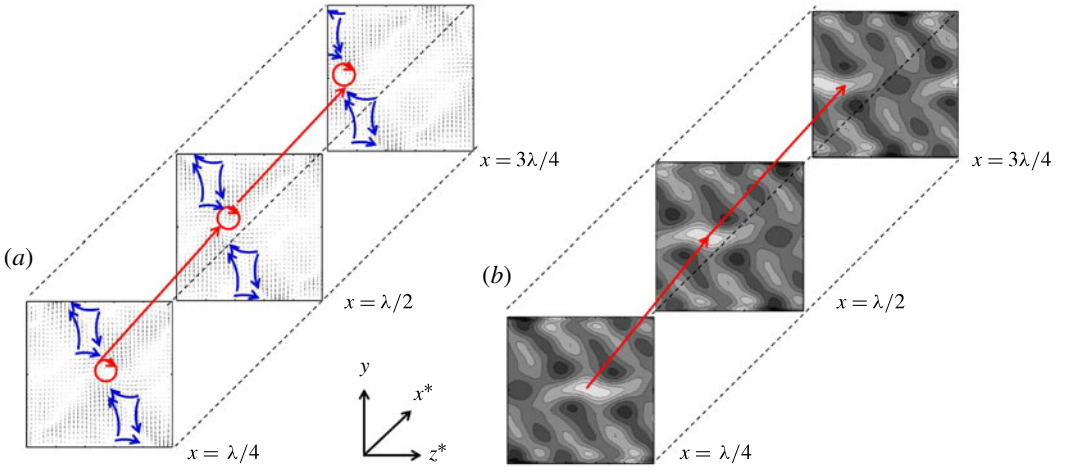


FIGURE 6. (Colour online) (*a*) Vector maps of (v', w') velocity; and (*b*) grey-scale maps (the white and black denote maximum and minimum, respectively) of Ω_x at $x = \lambda_x/4$, $\lambda_x/2$ and $3\lambda_x/4$. The vortices and saddle-points are marked by circles and hyperbolae, respectively, in (*a*). Parameters are as in figure 5 (which corresponds to $x = 0$).

streamwise vorticity and the underlying vortex-stretching mechanism is responsible for a more tenuous/inhomogeneous density field as observed in figure 4(*b*) for 3D stationary instability.

By fixing the streamwise wavenumber to $k_x = 0.579$ as in figure 4, we display a series of density (ϕ') patterns in the (y, z^*)-plane on figure 7(*a–c*) with increasing three-dimensionality (i.e. increasing k_z) at $x = 0$. (These patterns should be compared with those in figure 4*b* which corresponds to $k_z = 1$.) It is seen that the density patterns start deforming with increasing k_z and the stretching of clusters is prominent for larger k_z, resulting in a thinner and elongated shape of the density cluster around the mid-plane ($y = 0$) at $k_z = 3$ (figure 7*c*). The corresponding vectors maps of the cross-stream velocity (v', w') are displayed on figure 7(*d–f*): the position of the vortex in each figure is marked a closed curve; the vortex is surrounded by two saddle points in each figure, marked by hyperbolae. It is seen that the vortex takes an ellipsoidal shape at $k_z = 1.5$ (figure 7*d*) and eventually degenerates into a thin elongated shape at large $k_z > 2$ (figure 7*e*,*f*). For each k_z, the vortex appears to be driven by two nearby saddles in figure 7(*d–f*).

It must be noted that there is no universal definition of a vortex (see Jeong & Hussain 1995 for various definitions of a vortex and its identification schemes). In the topological characterization of flows (Perry & Chong 1987), the analysis is based on the invariants of the velocity gradient tensor that are connected with the vorticity field; the local flow topology is subsequently characterized using critical-point concepts of dynamical systems theory. For example, Chong, Perry & Cantwell (1990) identified a vortex core in terms of complex eigenvalues of the deformation tensor since they correspond to locally closed/spiralling streamlines in a reference frame moving with the critical point. The critical-point theory has been successfully used to characterize 3D eddying motions in a variety of steady/unsteady flows of Newtonian fluids (Perry & Chong 1987). In the dynamical systems theory, the source and sink are also called

https://doi.org/10.1017/jfm.2012.549 Published online by Cambridge University Press

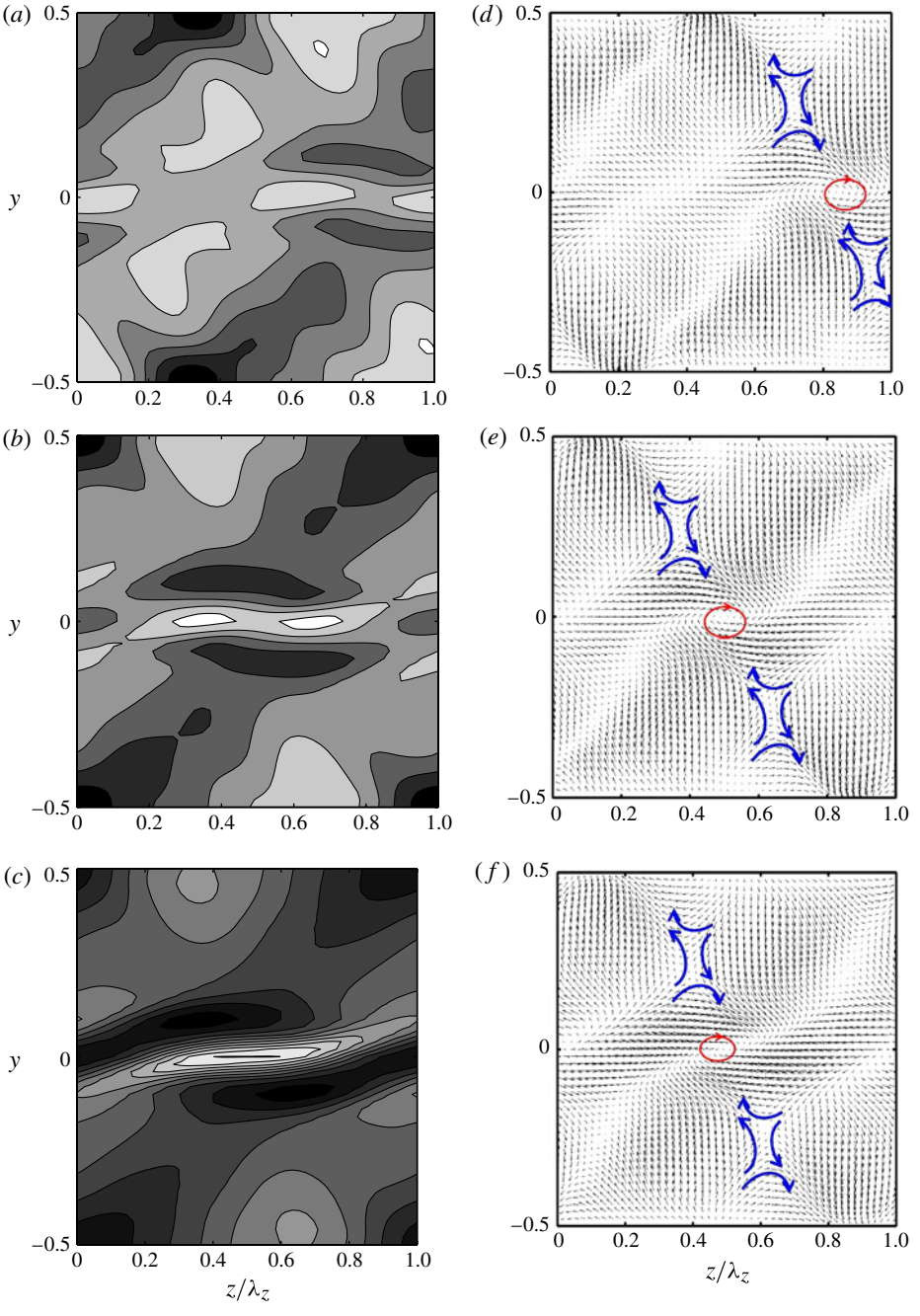


FIGURE 7. (Colour online) Effect of spanwise wavenumber on nonlinear patterns of perturbation density (*a–c*), and cross-stream perturbation velocity (*d–f*), in the (y, z^*)-plane at $x = 0$: (*a,d*) $k_z = 1.5$; (*b,e*) 2; and (*c,f*) 3. Here $k_x = 0.579$ and other parameters as in figure 4(*b*); the white and black denote maximum and minimum density, respectively.

https://doi.org/10.1017/jfm.2012.549 Published online by Cambridge University Press

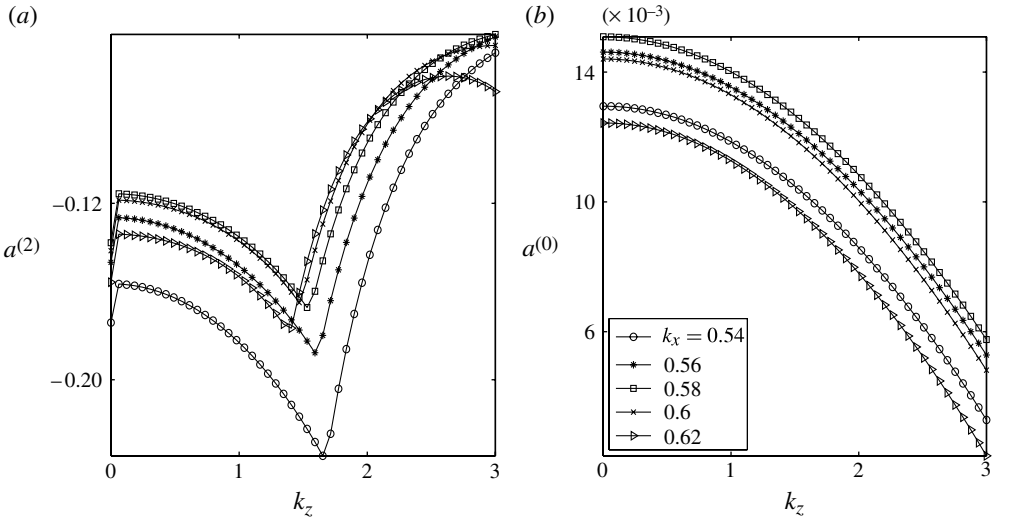


FIGURE 8. Variation of (*a*) $a^{(2)}$ and (*b*) $a^{(0)}$ with k_z for $k_x = 0.54$, 0.56, 0.58, 0.60 and 0.62. Other parameters as in figure 3.

unstable and stable nodes, respectively, and an ideal vortex is in fact a degenerate focus; following the definitions of Perry & Chong (1987), a non-degenerate focus can also be considered as a vortex.

In this paper, we have identified the fixed/critical points by visually inspecting the velocity vector maps such as those in figures 5(*a*), 6(*a*) and 7(*d–f*). For the nomenclature of critical points, we do not distinguish between degenerate and non-degenerate cases since this is a first attempt to describe the 3D motion (in granular flow) in terms of critical points of the underlying velocity field (see also §§ 7.1.2, 7.2 and 7.3). On the whole, the topology of motion as depicted in figures 5(*a*), 6(*a*) and 7(*d–f*) suggests that the flow is dominated by saddle-node-type motions in the (y, z^*)-plane along with a single vortex which appears to be driven by two nearby saddle points. A detailed 'reduced-order' theoretical model for the velocity gradient tensor to characterize the 3D eddying motion in granular Couette flow as well as the classification of its fixed points in terms of their behaviour near the wall and in the bulk can be developed (as in the works of Perry & Chong 1987; Jeong & Hussain 1995), but is relegated to a future work.

A closer look at the density patterns in figure 7(*a–c*) suggests that these patterns undergo significant structural changes (at small scales) for $k_z > 1.5$; this issue is discussed next. In figure 3(*a*), there is a kink on the $a^{(2)}$-curve at $k_z \sim 1.55$, marked by an upward arrow, which gives birth to the kink in the equilibrium amplitude (see the inset of figure 3*a*). The mean-flow resonance is not responsible for the genesis of this kink since the growth rate is positive at $k_z = 1.55$ and hence (7.5) is not satisfied at this point; therefore, $a^{(2)}$ does not diverge but remains continuous with a discontinuity in its derivative at $k_z \sim 1.55$. In fact, this kink is always present at some specified location of the spanwise wavenumber k_z for all values of k_x for the dominant stationary instability. The above assertion is verified in figure 8(*a*) which displays the kinks in the first Landau coefficient $a^{(2)}$ for five values of k_x, even though each growth rate curve remains smooth (see figure 8*b*) with varying spanwise wavenumber k_z. To understand the origin of these kinks, let us simplify the expression for the first Landau

https://doi.org/10.1017/jfm.2012.549 Published online by Cambridge University Press

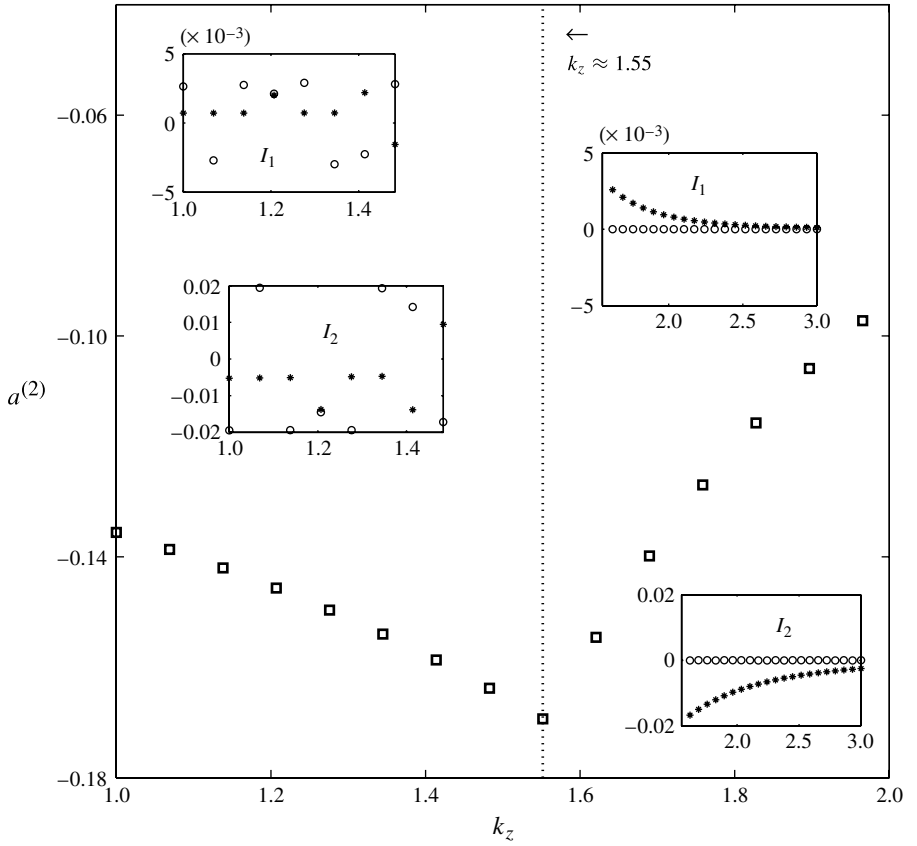


FIGURE 9. Variation of $a^{(2)}$ (squares) with k_z, with parameter values as in figure 3(*a*); the dotted vertical line marks the location of $k_z = 1.55$. Insets show the variations of I_1 and I_2 (see (7.7)) for two ranges of k_z (above and below $k_z = 1.55$): the circles and stars denote the real and imaginary parts of I_1 and I_2.

coefficient:

$$c^{(2)} = a^{(2)} + \mathrm{i}b^{(2)} = \frac{\displaystyle\int_{-1/2}^{1/2} \tilde{X}^{\dagger} G_{13}\,\mathrm{d}y}{\displaystyle\int_{-1/2}^{1/2} \tilde{X}^{\dagger} X^{[1;1]}\,\mathrm{d}y} = \frac{I_1}{I_2} = \frac{I_{1r}I_{2r} + I_{1i}I_{2i}}{I_{2r}^2 + I_{2i}^2} + \mathrm{i}\frac{I_{2r}I_{1i} - I_{1r}I_{2i}}{I_{2r}^2 + I_{2i}^2}, \tag{7.7}$$

where $I_1 = I_{1r} + \mathrm{i}I_{1i}$ and $I_2 = I_{2r} + \mathrm{i}I_{2i}$ are complex-valued functions. For the stationary instability in figure 3, the first Landau coefficient is always real, i.e. $b^{(2)} = 0$, which is possible if one of the following conditions holds: (i) I_1 and I_2 are real; (ii) I_1 and I_2 are purely imaginary; and (iii) $I_{2r}I_{1i} = I_{1r}I_{2i}$ (note that I_2 is always non-zero). For parameter values of figure 3(*a*), we have re-plotted the variation of $a^{(2)}$ (denoted by squares) over $k_z = [1, 2]$ in figure 9 and the insets show the real (circles) and imaginary (stars) parts of integrals, I_1 and I_2, for two ranges of $k_z = [1, 1.55]$ and $k_z = [1.55, 2]$. Both I_1 and I_2 are purely imaginary for $k_z = [1.55, 3]$, see the insets on the right-hand side of the vertical line, leading to real $c^{(2)}$. In contrast, both I_1 and I_2 are complex for $k_z = [1, 1.55]$, see the two left-hand insets in figure 9; therefore, the third condition (iii) holds for $k_z < 1.55$. This implies that the higher-order modal

https://doi.org/10.1017/jfm.2012.549 Published online by Cambridge University Press

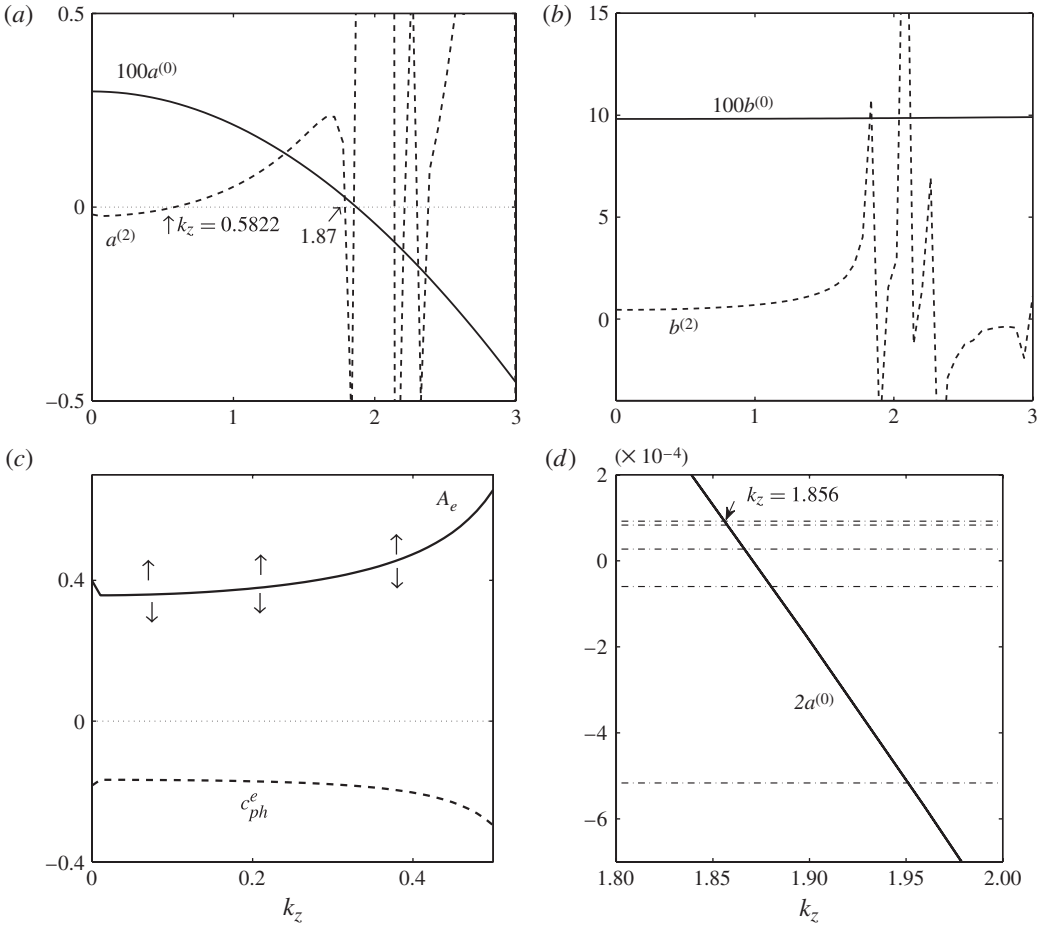


FIGURE 10. Variation of the dominant travelling instability with k_z at $k_x = 0.934$: (*a*) $100a^{(0)}$ (solid line) and $a^{(2)}$ (dashed line); (*b*) $100b^{(0)}$ (solid line) and $b^{(2)}$ (dashed line); (*c*) A_e (solid line) and c^e_{ph} (dashed line); (*d*) $2a^{(2)}$ (solid line) and five eigenvalues of the mean-flow operator (dot-dashed lines), see text for details. Other parameters as in figure 2.

eigenfunctions $X^{[2;2]}$ and $X^{[0;2]}$ change their character, resulting in a kink on the $c^{(2)}$-curve at $k_z \approx 1.55$ as seen in figure 3(*a*) as well as those in figure 8(*a*). The changes in $X^{[2;2]}$ and $X^{[0;2]}$ would affect the nonlinear perturbation fields (6.8) significantly as we have noticed in figure 7(*a–c*) for the perturbation density. Therefore, we conclude that the structural changes in the density patterns in figure 7(*a–c*) are due to the changes in the nonlinear (quadratic-order) modal eigenfunctions.

7.1.2. *Dominant travelling instability: patterns with saddles, nodes and vortices*

We now move to analyse the dominant travelling wave instabilities corresponding to the second peak of figure 2(*b*) – recall that the location of this peak, $k_x \approx 0.934$, is relatively insensitive to k_z. The variations of the real parts of the least-stable mode, $a^{(0)}$ (solid line), and the first Landau coefficient, $a^{(2)}$ (dashed line), with spanwise wavenumber (k_z) are shown in figure 10(*a*); the corresponding variations of the

https://doi.org/10.1017/jfm.2012.549 Published online by Cambridge University Press

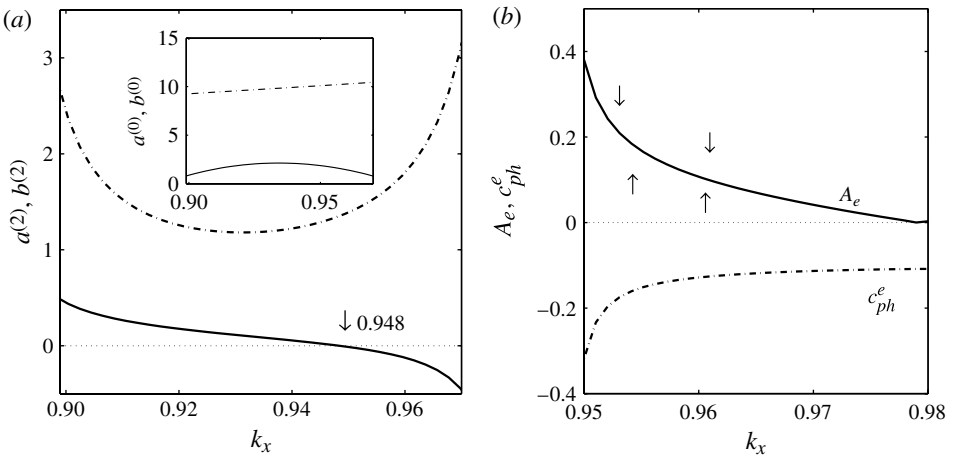


FIGURE 11. (*a*) Variation of $a^{(2)}$ (solid line) and $b^{(2)}$ (dot-dashed line) with k_x; the inset shows the variations of $100a^{(0)}$ (solid line) and $100b^{(0)}$ (dot-dashed line). (*b*) Variation of A_e (solid line) and c^e_{ph} (dot-dashed line) with k_x. The spanwise wavenumber is $k_z = 1$, with other parameters as in figure 2.

imaginary parts, $b^{(0)}$ (solid line) and $b^{(2)}$ (dashed line), are displayed in figure 10(*b*). The growth rate is positive and maximum at $k_z = 0$, decreases with increasing k_z and becomes negative at $k_z \approx 1.87$, indicated by an inclined arrow in figure 10(*a*), beyond which the flow is linearly stable to 3D perturbations. Looking at the variation of $a^{(2)}$ (dashed line), we find that $a^{(2)}$ changes its sign from negative to positive at $k_z \approx 0.582$, marked by a vertical arrow in figure 10(*a*). Therefore, $a^{(0)} > 0$ and $a^{(2)} < 0$ for a range of spanwise wavenumbers $k_z = [0, 0.582]$, resulting in supercritical Hopf/oscillatory ($b^{(n)} \neq 0$) bifurcations over this range. The corresponding variations of the equilibrium amplitude, A_e (solid line), and the equilibrium phase velocity, c^e_{ph} (dashed line), are shown in figure 10(*c*).

Notice in figure 10(*a*,*b*) that the first Landau coefficient $c^{(2)} = a^{(2)} + \mathrm{i}b^{(2)}$ diverges at several locations for $k_z > 1.87$ in the subcritical region (where the growth rate is negative). As explained for stationary wave instability in § 7.1.1, the mean-flow resonance condition (7.5) holds for travelling waves too at these singular points. This has been verified in figure 10(*d*): the solid line denotes $2a^{(0)}$ (i.e. twice the eigenvalues of the linear stability operator $\boldsymbol{L}$) and the horizontal dot-dashed lines represent five eigenvalues of the mean-flow operator $\boldsymbol{L}_0$ at quadratic-order. The intersection points of the solid and the dot-dash lines exactly satisfy the mean-flow resonance condition (7.5) that causes both $a^{(2)}$ and $b^{(2)}$ to diverge at these points, see the dashed discontinuities in figure 10(*a*,*b*).

To check the existence of nonlinear TW solutions at larger values of the spanwise wavenumber, we set $k_z = 1$ for which the variations of $a^{(2)}$ (solid line) and $b^{(2)}$ (dot-dashed line) with k_x are displayed in figure 11(*a*); the corresponding variations of $a^{(0)}$ and $b^{(0)}$ are displayed in its inset. It is clear that $a^{(0)} > 0$ and $a^{(2)} < 0$ over $k_x = (0.948, 0.97)$, yielding supercritical solutions; we have checked that there are mean-flow resonances (leading to discontinuities on the $c^{(2)}$-curve) beyond $k_x > 0.97$, and there is a small window of streamwise wavenumbers within $k_x = (0.98, 1)$ over which the criterion for subcritical solutions ($a^{(0)} < 0$ and $a^{(2)} > 0$) is satisfied.

https://doi.org/10.1017/jfm.2012.549 Published online by Cambridge University Press

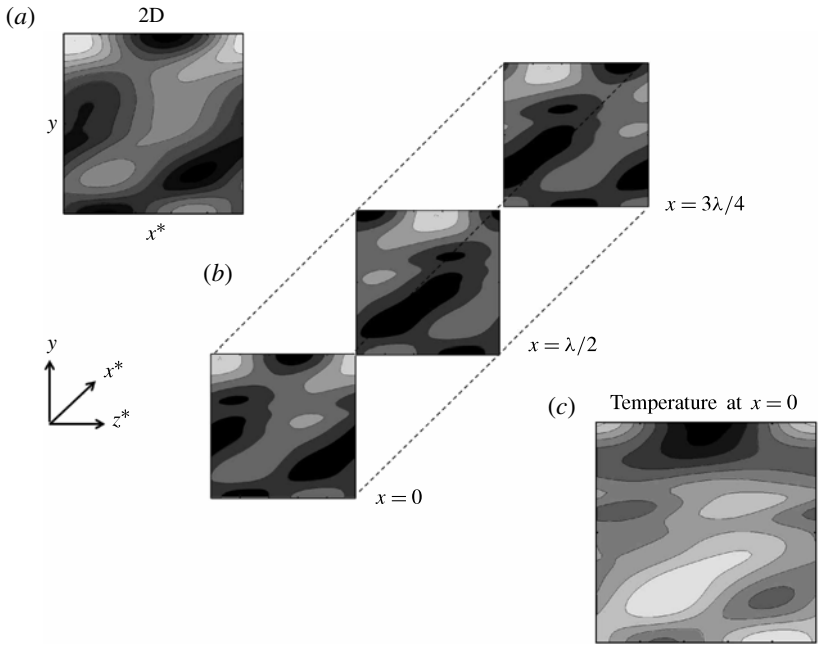


FIGURE 12. (*a*) Two-dimensional ($k_z = 0$) nonlinear perturbation density pattern in the (x, y^*)-plane. (*b*) Three-dimensional ($k_z = 1$) nonlinear density patterns in the (y, z^*)-plane at different streamwise locations ($x = 0$, $\lambda_x/2$ and $3\lambda_x/4$); and (*c*) the granular temperature (T') at $x = 0$ and $t = 0$. Parameters are as in figure 11 with $k_x = 0.97$. On the grey scale, the white is maximum and the black minimum.

Therefore, we have both supercritical and subcritical finite-amplitude solutions for the dominant travelling waves over two ranges of k_x at $k_z = 1$.

A series of nonlinear density patterns in the (y, z^*)-plane at three streamwise locations ($x = 0$, $\lambda_x/2$ and $3\lambda_x/4$) are displayed in figure 12(*b*), with $k_x = 0.97$ and $k_z = 1$. The pattern at $x = 0$ should be compared with figure 12(*a*) that shows the related 2D pattern ($k_z = 0$) of density in the (x^*, y)-plane – recall from (6.8) that the 3D pattern in the (x^*, y)-plane at $z^* = 0$ is the same as that in the (z^*, y)-plane at $x^* = 0$. It is seen that the overall features of 2D and 3D density patterns look similar, though the particle clusters/bands in the latter are more distorted. These patterns represent backward travelling waves, with a phase velocity of $c_{ph} \approx -0.1$, i.e. they travel much slower than the background shear flow. The granular temperature field at $x = 0$, displayed in figure 12(*c*), has similar characteristic features to the density field.

For parameter values of figure 12(*b*), the vector map of the cross-stream (v', w') velocity and the grey-scale contour map of the streamwise vorticity (Ω_x, (7.6)) are displayed in figures 13(*a*) and 13(*b*) , respectively, at the $x = 0$ location. Note that, for clarity, we have normalized z by twice the spanwise wavenumber ($2\lambda_z$). Similar to the case of the dominant SW instability in figure 5, we find that the cross-stream velocity field contains saddles, sources and sinks, along with a vortex (marked by the closed curve). The vortex is surrounded by two sources on its left and right, and by two saddles at above left and below right. As explained before, the vortical motion appears to be driven two saddle points. The location of the vortex corresponds to the maximum of the streamwise vorticity as confirmed in figure 13(*b*). Therefore, for both

https://doi.org/10.1017/jfm.2012.549 Published online by Cambridge University Press

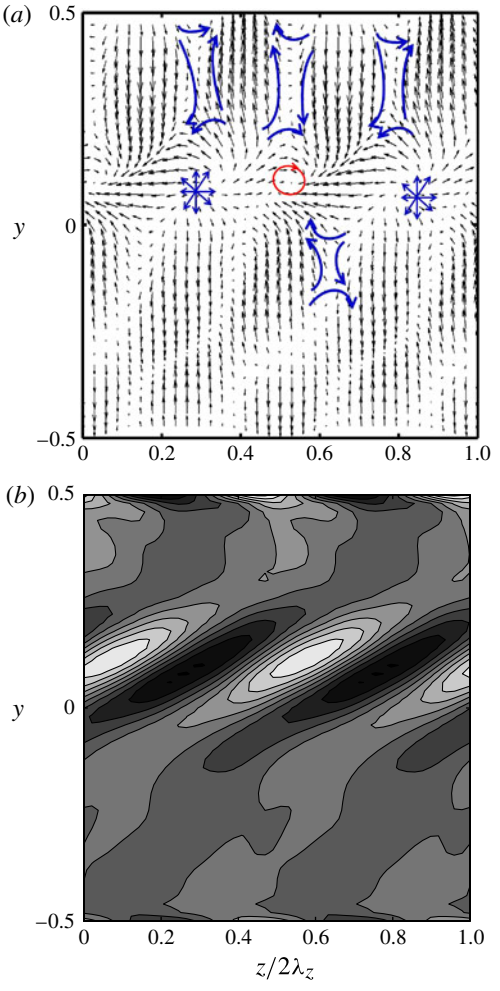


FIGURE 13. (Colour online) (*a*) Vector map of the nonlinear cross-stream (v', w') velocity field at $x = 0$; and (*b*) contour grey map of the perturbation streamwise vorticity (Ω_x) at $x = 0$. Other parameters are as in figure 12(*b*).

the dominant SW and TW instabilities, the cross-stream motion is largely dominated by saddle-node-type motions with a streamwise vortex.

7.1.3. *Long-wave ($k_x \sim 0$) instabilities: nodes and saddles*

Recall from the inset of figure 2(*a*), there are instabilities at small streamwise wavenumbers $k_x \sim 0$ (i.e. the streamwise wavelengths, $\lambda_x = 2\pi/k_x$, are large/long and hence called long waves) for a range of spanwise wavenumbers $k_z \in (0, 1.5)$. For these parameter values, the gradient-banding modes ($k_x = 0$; Shukla & Alam 2009, 2011*a*) are linearly unstable, and the flow also remains unstable to long-wave 2D perturbations ($k_x \neq 0$) of stationary and travelling waves. To probe the effect of spanwise perturbations ($k_z \neq 0$) on long-wave instabilities, we consider two values of $k_x = 10^{-5}$ and $k_x = 4 \times 10^{-5}$ for which the flow is known (Shukla & Alam 2011*b*) to be unstable to 2D perturbations of stationary and travelling waves, respectively.

https://doi.org/10.1017/jfm.2012.549 Published online by Cambridge University Press

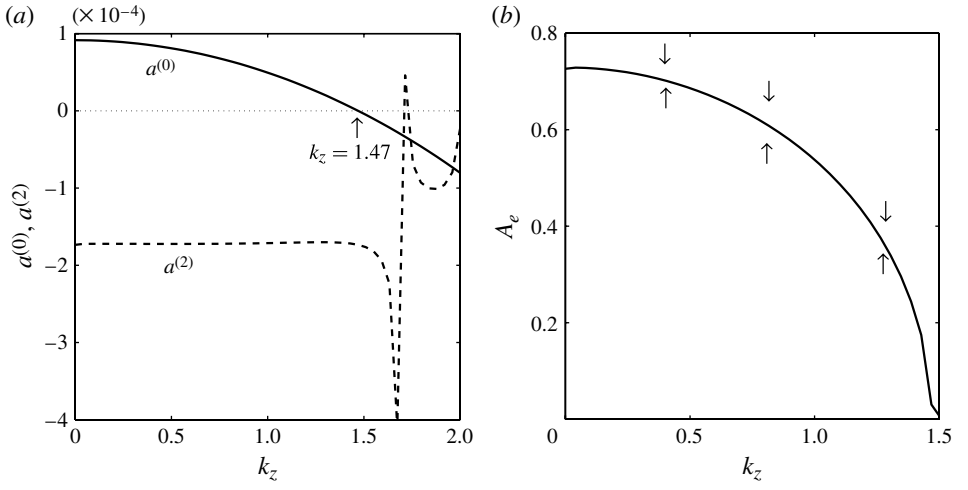


FIGURE 14. Variation of stationary long-wave mode with k_z: (*a*) $a^{(0)}$ (solid line) and $a^{(2)}$ (dashed line); (*b*) A_e. Here $k_x = 10^{-5}$ and other parameters as in figure 2.

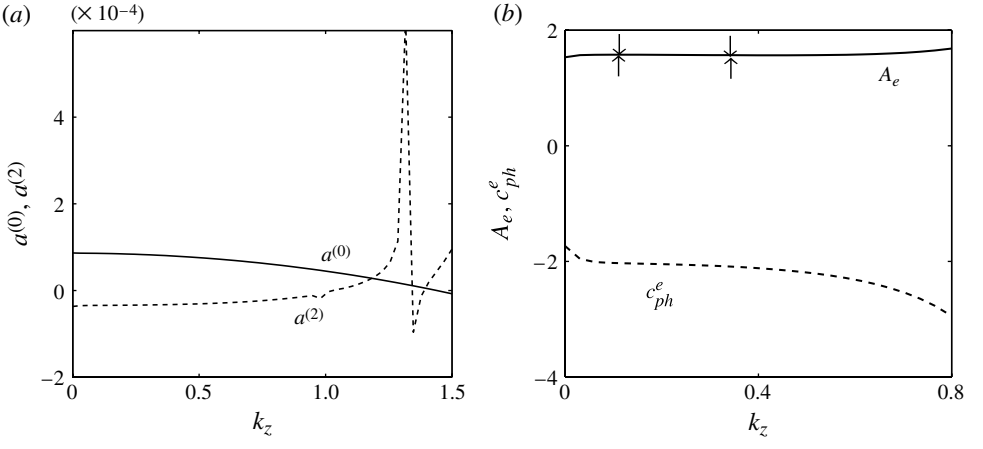


FIGURE 15. Variation of travelling long-wave mode with k_z: (*a*) $a^{(0)}$ (solid line) and $a^{(2)}$ (dashed line); (*b*) A_e (solid line) and c^e_{ph} (dashed line). Here $k_x = 4\times10^{-5}$ and other parameters as in figure 2.

Figure 14(*a*) shows the variations of $a^{(0)}$ (solid line) and $a^{(2)}$ (dashed line) with spanwise wavenumber for $k_x = 10^{-5}$, with other parameters as in figure 2. It is seen that the 3D flow remains unstable to stationary perturbations up to $k_z \approx 1.47$, marked by an arrow in figure 14(*a*), and stable thereafter. Note that the first Landau coefficient $a^{(2)}$ varies very little for $k_z < 1.47$, and the discontinuity in $a^{(2)}$ at $k_z \approx 1.6$ is tied to the occurrence of the mean-flow resonance as discussed earlier. The equilibrium amplitude decreases with increasing k_z as seen in figure 14(*b*). Figure 15 is the analogue of figure 14 for travelling waves at $k_x = 4 \times 10^{-5}$. We find that $a^{(0)} > 0$ and $a^{(2)} < 0$ for a range of spanwise wavenumbers $k_z = (0, 1.1)$ over which the flow admits

https://doi.org/10.1017/jfm.2012.549 Published online by Cambridge University Press

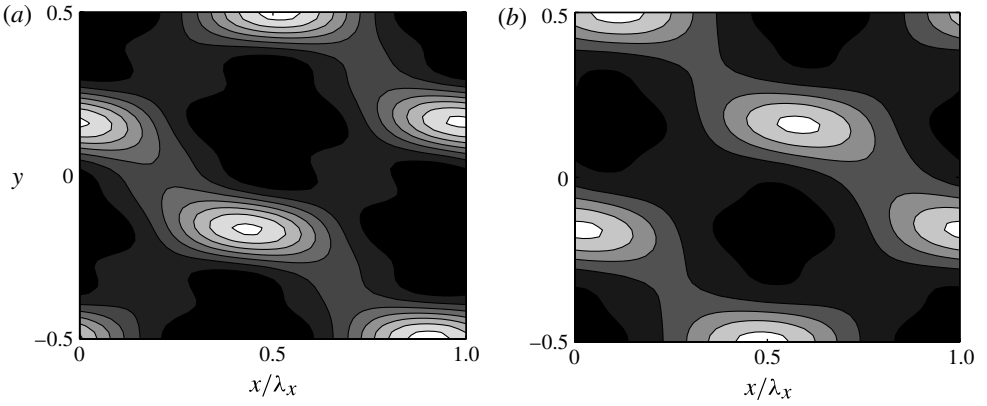


FIGURE 16. Nonlinear density (ϕ') patterns in the (x^*, y)-plane for (a) 2D ($k_z = 0$) and (b) 3D ($k_z = 1$, at $z = 0$) perturbations for $k_x = 10^{-5}$ (as in figure 14). On the grey scale, the white is maximum and the black minimum.

supercritical Hopf bifurcations since $b^{(0)} \neq 0$ (not shown). Figure 15(b) suggests that the equilibrium amplitudes, A_e (solid line), for these TWs remain relatively unaffected with varying k_z which is in contrast to the decaying amplitudes with increasing k_z for SWs in figure 14(b). For both values of k_x, the bifurcations are supercritical for 3D perturbations as in the case of 2D perturbations (Shukla & Alam 2011*b*).

A comparison of the density patterns for 2D perturbations and 3D perturbations (in the (x^*, y)-plane at $z = 0$ for $k_z = 1$) is shown in figures 16(a) and 16(b), respectively. We observe three rows of density maxima along the gradient (y) direction, and both patterns look strikingly similar. This observation holds also for other perturbation fields (velocity and granular temperature). Since $a^{(2)}$ deviates little with increasing k_z (see figure 14a), the fundamental and its harmonics ($X^{[1;1]}$, $X^{[0;2]}$, $X^{[2;2]}$ and $X^{[1;3]}$) do not change significantly with k_z, and therefore the patterns remain similar for 2D and 3D perturbations for such long waves.

The analogue of figure 12 (the dominant TW patterns) is shown in figure 17 for long-wave travelling patterns at $k_x = 4 \times 10^{-5}$ and $k_z = 0.3$. The density patterns in figure 17(a) (2D pattern) and figure 17(b) (at $x = 0$, i.e. a 3D pattern) are similar with respect to the orientation of particle clusters. Unlike for dominant instabilities at $k_x = O(1)$ in figure 12(c), the spatial pattern of granular temperature for long waves, as shown in figure 17(c), is almost anti-correlated with the corresponding density pattern in figure 17(b) at $x = 0$, i.e. high/low temperature corresponds to low/high density, respectively. A comparison between figures 12 and 17 suggests that the long-wave TW patterns are markedly different from those that originate from dominant TW instabilities both in terms of the orientation of particle clusters as well as in small-scale features. We have verified that the associated cross-stream velocity (v', w') patterns contain only nodes and saddles (not shown).

7.2. *Instabilities and patterns in dense flows*

Here we present results for dense flows by fixing the mean density to $\phi^0 = 0.4$, with a Couette gap of $H = 50$ and a restitution coefficient of $e = 0.8$; the linear and nonlinear stability results for the higher density of $\phi^0 = 0.5$ are similar (and hence not shown). The contours of zero and positive growth rates of the least-stable mode in

https://doi.org/10.1017/jfm.2012.549 Published online by Cambridge University Press

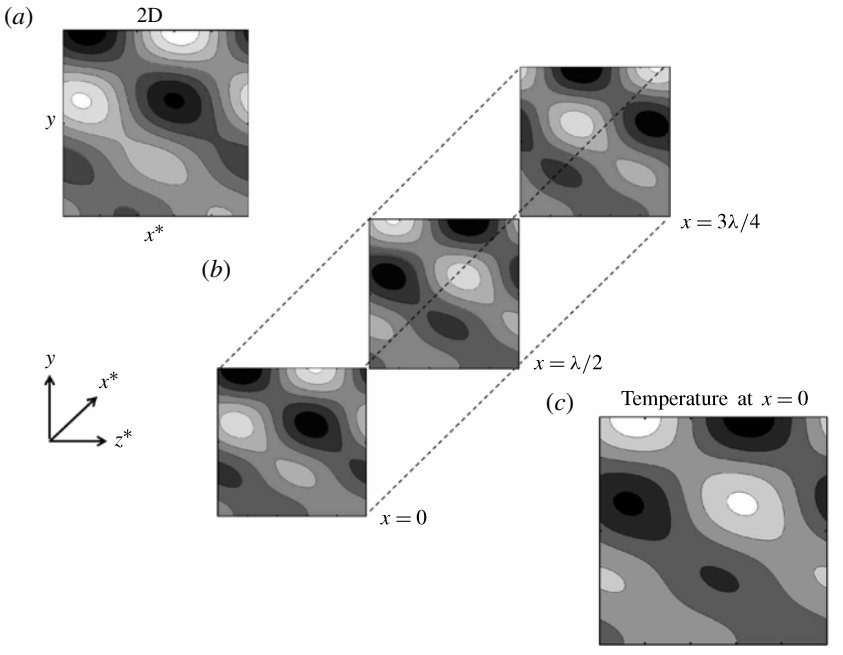


FIGURE 17. Same as figure 12 but for long-wave ($k_x = 4 \times 10^{-5}$) travelling instability. On the grey scale, the white is maximum and the black minimum.

the (k_x, k_z)-plane are displayed in figure 18(*a*), and the corresponding frequency map is displayed in figure 18(*b*). For this parameter combination, the flow is known to be unstable to 2D perturbations (Alam 2006) for a small range of k_x, and the origin of this instability is tied to the underlying gradient-banding mode ($k_x = 0$). Figure 18(*b*) confirms that these instabilities are travelling waves, except for a very small range of k_z (<0.0001) over which stationary waves exist whose origin is the 'stationary' gradient-banding mode. There exist two instability zones in figure 18(*a*): on for small k_z (~ 0) and the other for moderate values of k_z.

The variation of the growth rate ($a^{(0)}$) of the least-stable mode with k_z is shown in figure 18(*c*) for four values of streamwise wavenumber: $k_x = 0$, 0.001, 0.005 and 0.01. For the streamwise-independent mode ($k_x = 0$, solid line in figure 18*c*), the growth rate is maximum at $k_z = 0$ (i.e. a 2D perturbation) and decreases monotonically with increasing k_z. However, at $k_x = 0.001$ and 0.005, the maximum growth rate occurs at $k_z \neq 0$ (i.e. a 3D perturbation); with further increasing k_x to 0.01, the maximum in growth rate shifts back to a 2D ($k_z = 0$) mode. Therefore, in figure 18(*a*), the small instability lobe near $k_z \sim 0$ originates from 2D perturbations but the larger one for moderate values of k_z originates from 3D perturbations.

To probe the effect of finite-amplitude perturbations on the above mentioned two types of instabilities in dense flows, we set the streamwise wavenumber to $k_x = 0.005$. Figure 19 shows the variations of the real ($a^{(2)}$) and imaginary ($b^{(2)}$) parts of the first Landau coefficient with spanwise wavenumber, represented by the solid and dot-dash lines, respectively. Note that $a^{(2)} < 0$ for the whole range of k_z shown, but $a^{(0)} > 0$ (see the dot-dashed line in figure 18*c*) for $k_z = [0, 0.04]$ and $k_z = [0.1, 0.5]$, leading to supercritical finite-amplitude solutions for two ranges of k_z as displayed in the inset

https://doi.org/10.1017/jfm.2012.549 Published online by Cambridge University Press

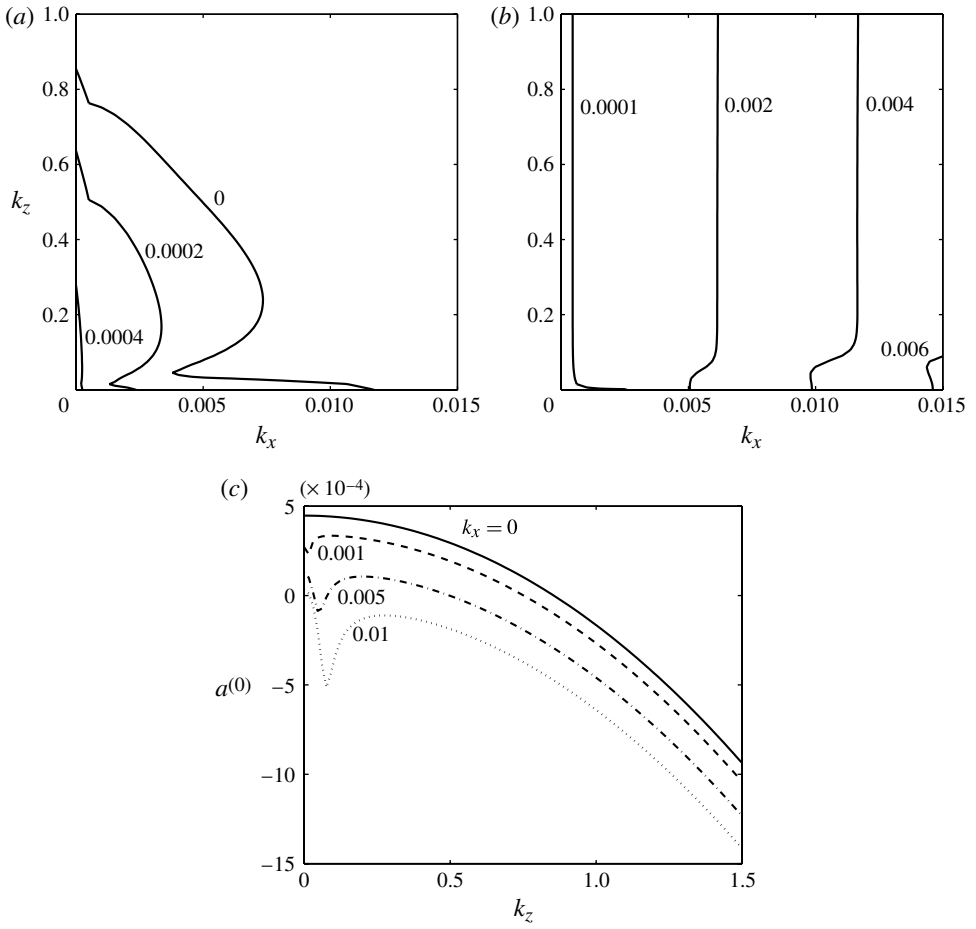


FIGURE 18. Contours of (a) the growth rate ($a^{(0)}$) and (b) the frequency ($|b^{(0)}|$) of the least-stable mode in the (k_x, k_z)-plane for dense flows ($\phi^0 = 0.4$) with $H = 50$ and $e = 0.8$. (c) Variation of the growth rate of the least-stable mode with k_z for $k_x = 0$ (solid line), 0.001 (dashed line), 0.005 (dot-dashed line) and 0.01 (dotted line).

of figure 19. Note that the bifurcation is Hopf/oscillatory for both ranges of k_z since $b^{(0)} \neq 0$ (see figure 18b for frequency contours).

The nonlinear patterns of perturbation density in the (y, z^*)-plane (at $x = 0$ and $t = 0$) for $k_z = 0.02$ and 0.4 are displayed in figures 20(a) and 20(b), respectively, with other parameters as in figure 19. While figure 20(b) contains three clusters/bands of particles across the y-direction, figure 20(a) contains two particle clusters; the orientation of the particle clusters is seen to be different in the two panels. Therefore, the structure and orientation of the particle clusters originating from 2D perturbations (figure 20a) differ from those originating from 3D perturbations (figure 20b). The related cross-stream (v', w') field (not shown) contains only node-saddle-type motions (see figure 21b and the related discussion below). Note that these supercritical TW patterns in dense flows (at long waves, $k_x \sim 0$) also differ from those shown in figure 17(b) (at $\phi^0 = 0.2$ and also at long waves $k_x \sim 0$) with respect to the orientation of particle bands.

https://doi.org/10.1017/jfm.2012.549 Published online by Cambridge University Press

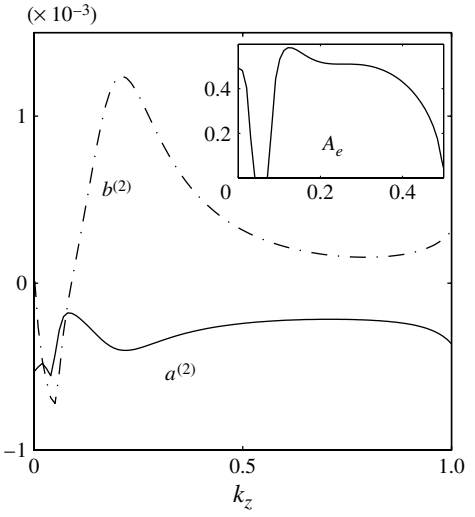


FIGURE 19. Variation of $a^{(2)}$ (solid line) and $b^{(2)}$ (dot-dashed line), and A_e (inset) with k_z for $k_x = 0.005$. Other parameters are as in figure 18.

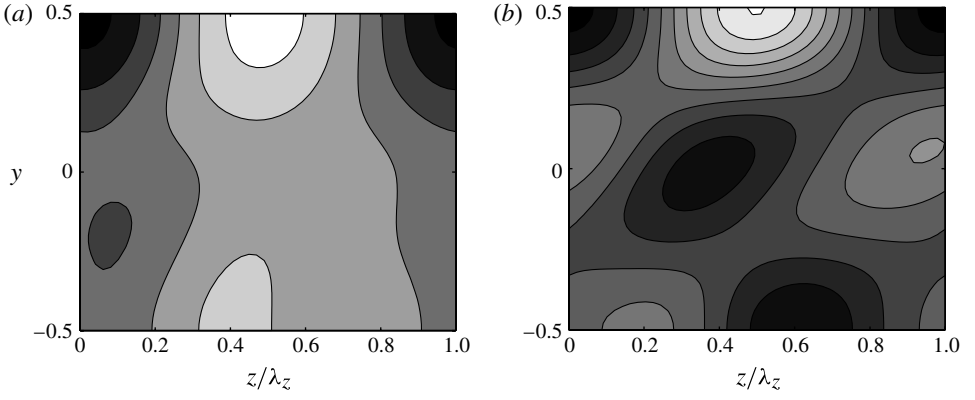


FIGURE 20. Nonlinear TW density (ϕ') patterns in the (y, z^*)-plane at $x = 0$ location for (a) $k_z = 0.02$ and (b) $k_z = 0.4$, with $k_x = 0.005$. Other parameters are as in figure 19. On the grey scale, the white is maximum and the black minimum.

For even smaller values of streamwise wavenumbers (say, $k_x = 0.001$) we found both supercritical TW solutions for a range of $k_z = (0, 0.75)$ over which the flow is linearly unstable (see the growth rate curve in figure 18*c* for $k_x = 0.001$) and subcritical TW solutions for $k_z > 0.9$. These supercritical and subcritical solutions are compared in figure 21. In addition to particle clusters near the top wall in figure 21(*a,c*), there is an additional row of clusters (located around $y \sim -0.1$) in the subcritical pattern in figure 21(*c*). The velocity pattern in figure 21(*b*) resembles a degenerate node-saddle case (case-I in figure 5 of Perry & Chong 1987). On the other hand, the subcritical pattern in figure 21(*d*) contains only nodes (sources and sinks).

Lastly, let us make a few additional comments on nonlinear instabilities in the dense limit. When the Couette gap is increased from $H = 50$ to $H = 160$, the analogues of

https://doi.org/10.1017/jfm.2012.549 Published online by Cambridge University Press

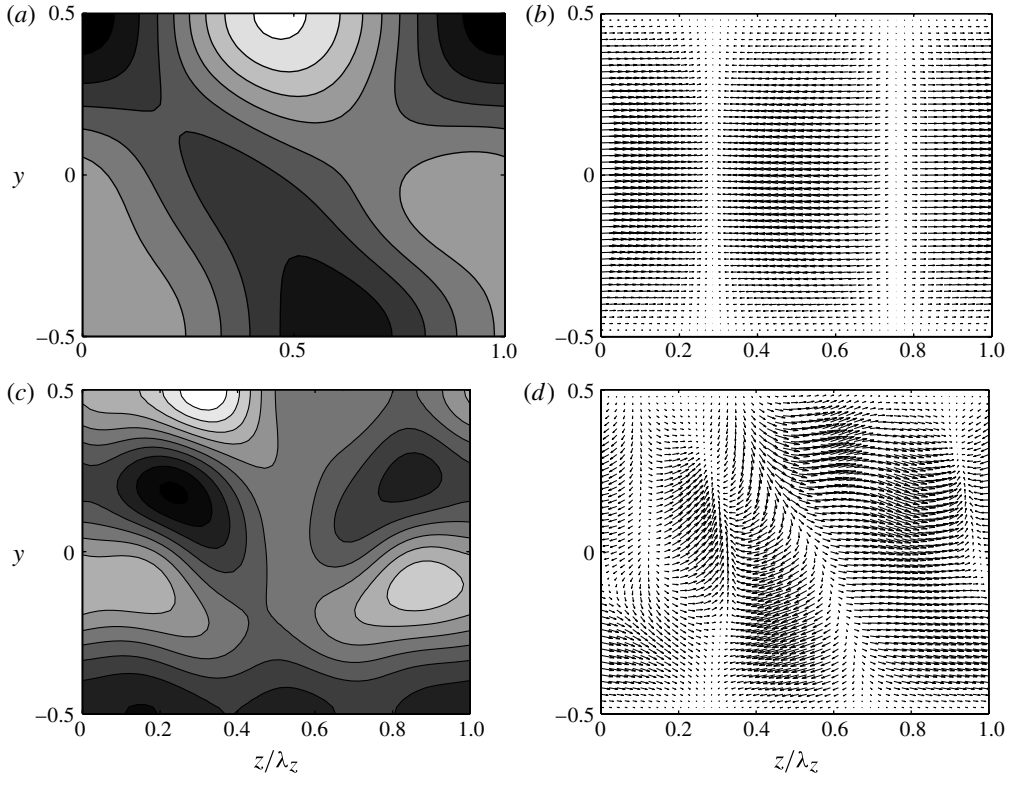


FIGURE 21. Supercritical (a,b, $k_z = 0.74$) and subcritical (c,d, $k_z = 1$) TW patterns of (a,c) perturbation density and (b,d) (v', w') velocity vectors at $t = 0$ for $k_x = 0.001$. Other parameters as in figure 18.

dominant SW and TW instabilities (that occur at $k_x = O(1)$ with the largest growth rate among all instabilities) appear even at $\phi^0 = 0.4$ (with other parameters as in figure 18); the nonlinear behaviour of these modes resembles that for $\phi^0 = 0.2$ as described in § 7.1. On the other hand, increasing the mean density to $\phi^0 = 0.5$ (with other parameters as in figure 18), we have only long-wave ($k_x \sim 0$) instabilities for a range of spanwise wavenumbers $k_z = O(1)$. Shukla & Alam (2011*b*) showed that the nonlinear equilibrium states do not exist at $(\phi^0, H) = (0.5, 50)$ for 2D perturbations ($k_z = 0$). However, we found the existence of both SW and TW nonlinear solutions at $k_x \sim 0$ for 3D perturbations with $k_z = O(1)$. These results are omitted for the sake of brevity.

7.3. *Purely 3D instabilities in dilute flows: large-scale vortices*

So far we have discussed nonlinear stability results for moderately dense ($\phi^0 = 0.2$) and dense ($\phi^0 = 0.4$) flows. Alam (2006) showed that there are 3D stationary and travelling wave instabilities in the dilute limit ($\phi^0 < 0.1$) having no analogue for 2D perturbations ($k_z = 0$), i.e. these are purely 3D instabilities in the sense that they are not present in 2D flows; the nonlinear saturation of these instabilities is studied in § 7.3.1. Another class of 3D stationary instabilities, which survive in 2D flows but have an anomalous dependence on inelasticity, is studied in § 7.3.2.

https://doi.org/10.1017/jfm.2012.549 Published online by Cambridge University Press

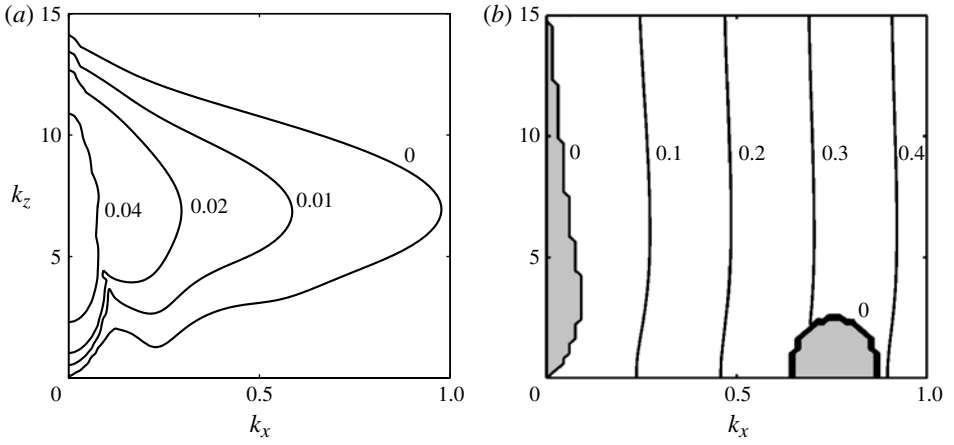


FIGURE 22. Contours of (*a*) the growth rate ($a^{(0)}$) and (*b*) the frequency ($|b^{(0)}|$) of the least-stable mode in the (k_x, k_z)-plane for dilute flows ($\phi^0 = 0.05$) with $H = 100$ and $e = 0.8$. The grey-shaded regions in (*b*) represent stationary ($b^{(0)} = 0$) waves.

7.3.1. *Instabilities originating from pure spanwise perturbations*

We set the mean density to $\phi^0 = 0.05$, with a Couette gap of $H = 100$ and a restitution coefficient of $e = 0.8$; the 3D linear stability of granular plane Couette flow for this parameter combination was studied by Alam (2006). It must be noted that the flow is linearly stable to 2D perturbations ($k_z = 0$) for this parameter set, but we show below that there are 3D finite-amplitude solutions with large-scale vortices.

The stability diagram displaying the contours of positive and zero growth rates of the least-stable mode in the (k_x, k_z)-plane is shown in figure 22(*a*), and the corresponding contours of its frequency in figure 22(*b*). The grey-shaded regions in figure 22(*b*) represent stationary waves. The flow is linearly unstable inside the neutral/critical ($a^{(0)} = 0$) contour and stable outside. It is clear that the flow is linearly stable to 2D perturbations ($k_z = 0$, the horizontal axis in figure 22*a*), but unstable to streamwise-independent ($k_x = 0$, i.e. those waves that have no dependence along the x-direction) perturbations. For any specified k_z in figure 22(*a*), the growth rate of these instabilities is seen to decrease with increasing k_x (except at $k_z = 1$). There are two instability lobes in figure 22(*a*): the lobe is near $k_x \sim 0$ represents stationary waves ($b^{(0)} = 0$, see the grey-shaded region in figure 22*b*) and the larger lobe at $k_x > 0.1$ represents travelling waves ($b^{(0)} \neq 0$, see figure 22*b*). Alam (2006) showed that the origin of these stationary instabilities at small k_x is tied to pure spanwise perturbations ($k_z \neq 0$, but $k_x = 0$ and $\partial/\partial y(\cdot) = 0$; see Shukla & Alam 2012 for details on nonlinear stability for this class of perturbations that are responsible for the vorticity-banding phenomenon). The modal evolution of these stationary instabilities with k_x (Alam & Nott 1998; Alam 2006) gives birth to new 3D travelling instabilities at $k_x = O(1)$, leading to the larger instability lobe in figure 22(*a*). Note in figure 22(*a*) that the instabilities in dilute flows exist for a much larger range of spanwise wavenumber up to $k_z = O(10)$ in comparison to those for moderately dense to dense flows (discussed in §§ 7.1 and 7.2) that survive only for a smaller range of spanwise wavenumber up to $k_z = O(1)$.

Let us first probe the nonlinear fate of SW instabilities for small k_x in figure 22(*a*). The variation of the growth rate of the least-stable mode with k_x is shown in figures 23(*a*) and 23(*b*), for spanwise wavenumbers of $k_z = 0.1$ and 10, respectively.

https://doi.org/10.1017/jfm.2012.549 Published online by Cambridge University Press

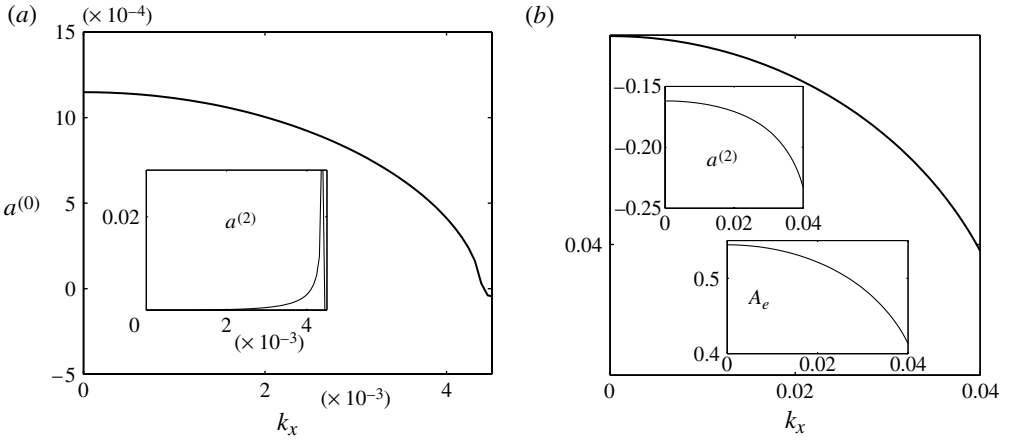


FIGURE 23. Variation of $a^{(0)}$, $a^{(2)}$ (inset) and A_e (lower inset in b) with k_x for stationary waves at small values of k_x: (a) $k_z = 0.1$ and (b) 10. Parameter values are as in figure 22.

An inset of each panel in figure 23 shows the corresponding variation of the real part of the first Landau coefficient $a^{(2)}$; note that the imaginary part of the Landau coefficient, $b^{(2)}$, is zero for SWs. For small values of $k_z = 0.1$, we find $a^{(0)} > 0$ and $a^{(2)} > 0$, see figure 23(a), and hence the cubic-order nonlinear solution does not exist for this case. However, for larger values of k_z (>0.5), we found $a^{(0)} > 0$ and $a^{(2)} > 0$, an example of which is shown in figure 23(b) for $k_z = 10$. Therefore, we have finite-amplitude equilibrium solutions for a range of $k_x \sim 0$ that appear via supercritical pitchfork bifurcations for $k_z > 0.5$, see the lower inset of figure 23(b).

Moving to the 3D TW instabilities in figure 22(a), we show the variations of $a^{(2)}$ (solid line) and $b^{(2)}$ (dot-dashed line) with k_z in figure 24(a) for $k_x = 0.1$; the corresponding variations of $a^{(0)}$ (solid line) and $b^{(0)}$ (dot-dashed line) are shown in its upper inset. Since the growth rate remains positive ($a^{(0)} > 0$) with a non-zero frequency and $a^{(2)} < 0$ for $k_z \sim [1.3, 13]$, we have supercritical Hopf bifurcations over $k_z = [1.3, 13]$. We also found subcritical Hopf bifurcations for smaller values of k_z since $a^{(0)} < 0$ and $a^{(2)} > 0$ over $k_z \sim [0, 1.27]$. The transition from subcritical to supercritical bifurcations occurs at $k_z \approx 1.273$ where there is a change-over in the eigenmode which is evident in the 'first' discontinuity on the frequency curve in the upper inset of figure 24(a) – this new eigenmode continues to be the least-stable mode till $k_z \approx 4.0$, again signalled by the 'second' discontinuity on the frequency curve, beyond which a third eigenmode takes over as the least-stable mode. We have verified that the first and third discontinuities on the $c^{(2)}$-curve in the main panel of figure 24(a) correspond to this change-over in the modal hierarchy. We have further verified that the 'second' discontinuity on the $c^{(2)}$-curve ($c^{(2)} = a^{(2)} + \mathrm{i}b^{(2)}$) corresponds to a mean-flow resonance (see (7.3)–(7.5) in § 7.1.1) at which $c^{(2)}$ undergoes a jump-discontinuity of order-infinity. The overall variation of equilibrium amplitude with $k_z \in (0, 13)$ is shown in the lower inset of figure 24(a): three discontinuities on the A_e-curve correspond exactly to the change-over in the modal hierarchy at two locations and the location of mean-flow resonance.

Figure 24(b) is the same as figure 24(a) but for a larger value of the streamwise wavenumber ($k_x = 1$) for which the flow is linearly stable ($a^{(0)} < 0$) for all k_z (see the upper inset of figure 24b as well as the stability diagram in figure 22). For this case, there are subcritical Hopf bifurcations for $k_z = [0, 1.3]$ over which $a^{(2)} > 0$ and $a^{(0)} < 0$.

https://doi.org/10.1017/jfm.2012.549 Published online by Cambridge University Press

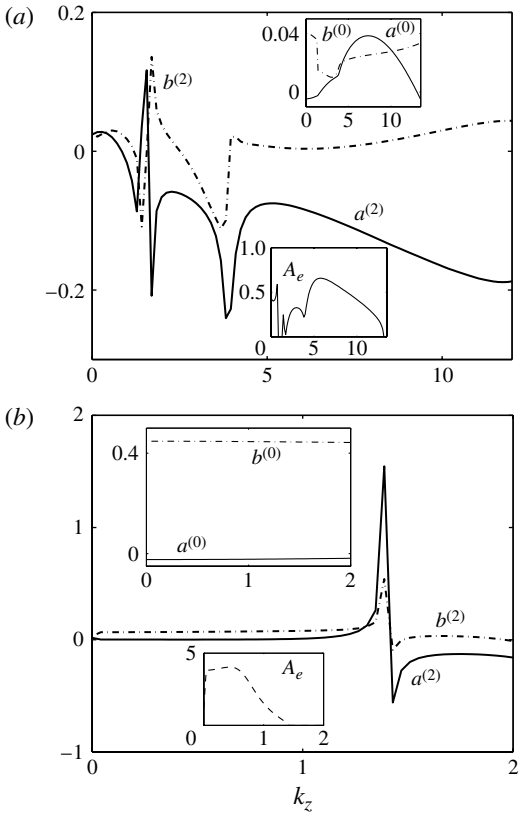


FIGURE 24. Variation of the first Landau coefficient ($a^{(2)}$ (solid line), $b^{(2)}$ (dot-dashed line)), linear eigenvalue (upper inset, $a^{(0)}$ (solid line), $b^{(0)}$ (dot-dashed line)) and equilibrium amplitude A_e (lower inset) with spanwise wavenumber k_z for (*a*) $k_x = 0.1$ and (*b*) $k_x = 1$. Other parameters as in figure 22.

Note that the jump-discontinuity in $a^{(2)}$ near $k_z \sim 1.5$ represents the occurrence of mean-flow resonance as discussed before. The equilibrium amplitude, A_e, decreases with increasing k_z as seen in the lower inset of figure 24(*b*).

The nonlinear TW patterns of density and (v', w') velocity in the (y, z^*)-plane at the $x = 0$ location are displayed in the first, second and third rows of figure 25 for $k_z = 0.2$, 2 and 12, respectively, with other parameters as figure 24(*a*); these specific values of k_z have been chosen to represent three different modes of figure 24(*a*). While the patterns in the first row represent subcritical (and unstable) solutions, those in the second and third rows are supercritical solutions. The subcritical pattern in figure 25(*a*) has its density maximum (white region) near the upper wall and contains another dense cluster/band of particles aligned parallel to the z-axis (at $y \sim -0.1$); the associated cross-stream velocity field in figure 25(*b*) contains a vortex (marked by the closed curve), and an imperfect source at $(y, z^*) \approx (-0.2, 0.3)$ which appears to be driving a saddle-type motion above it (marked by curved arrows). The supercritical patterns in figure 25(*c–f*) are seen to be structurally different from their subcritical counterpart (figure 25*a*,*b*). The particle clusters are now oriented at some oblique angle to the spanwise direction; the cross-stream velocity fields in figure 25(*d*,*f*) contain only saddles and nodes.

https://doi.org/10.1017/jfm.2012.549 Published online by Cambridge University Press

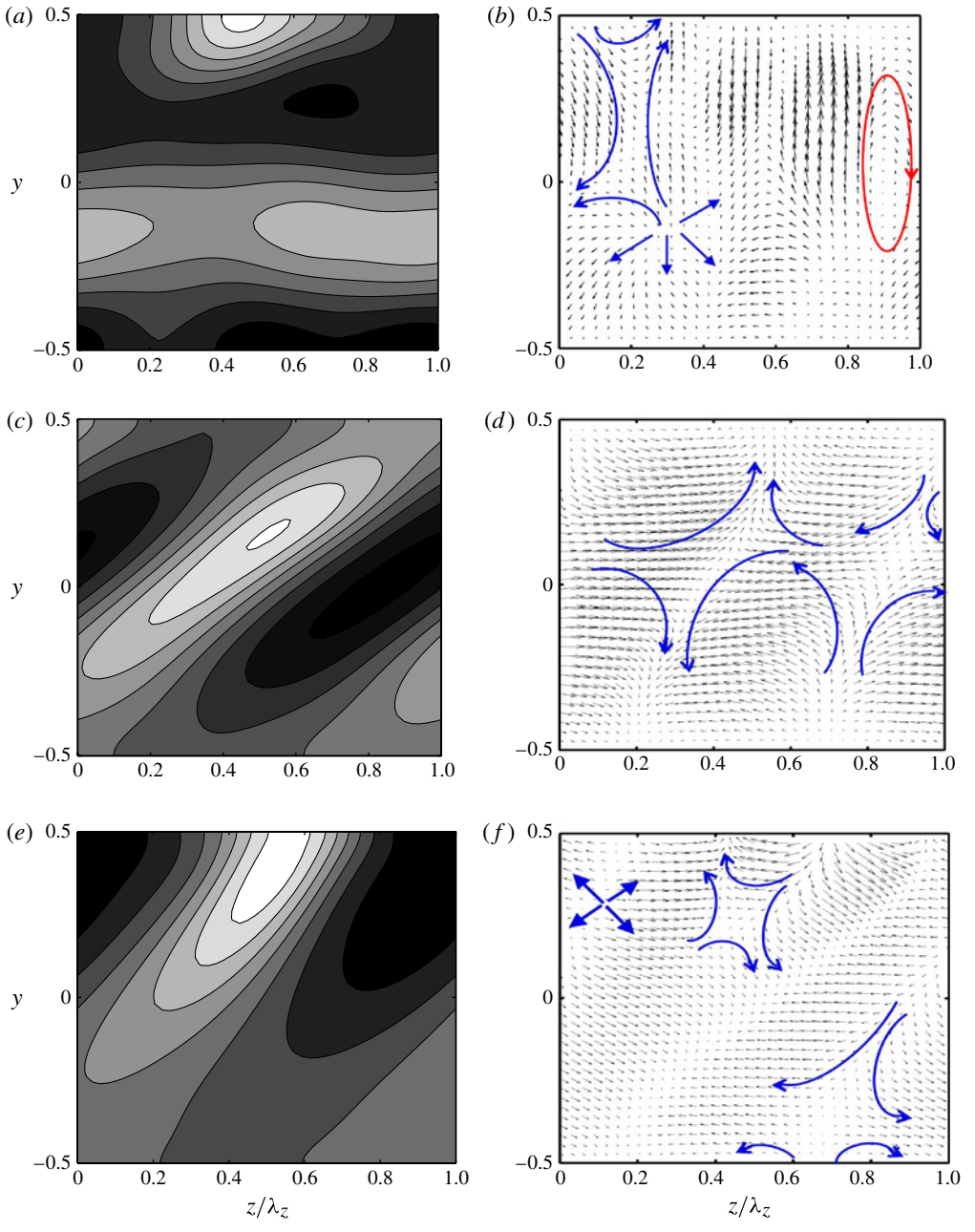


FIGURE 25. (Colour online) Nonlinear TW patterns of (a, c, e) perturbation density (ϕ') and (b, d, f) (v', w') velocity vectors in the (y, z^*)-plane at $x = 0$ and $t = 0$ at $k_x = 0.1$ for different spanwise wavenumbers: $k_z = 0.2$ (a,b), $k_z = 2$ (c,d) and $k_z = 12$ (e,f). Other parameters as in figure 24(a). On the grey scale, the white is maximum and the black minimum.

https://doi.org/10.1017/jfm.2012.549 Published online by Cambridge University Press

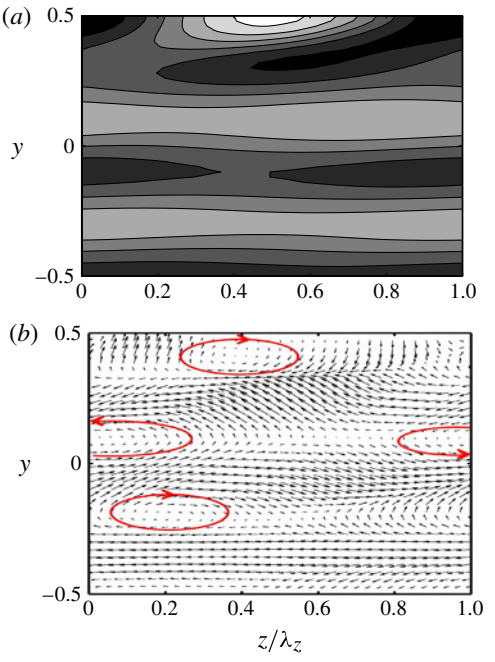


FIGURE 26. (Colour online) Same as figure 25 but for unstable subcritical patterns for $k_x = 1$ and $k_z = 1.3$. Other parameters as in figure 24(*b*).

Corresponding to the subcritical solutions in figure 24(*b*), we display the nonlinear patterns of perturbation density and (v', w') velocity in figures 26(*a*) and 26(*b*), respectively, for $k_x = 1$. The density pattern, with modulated bands of particles parallel to the z-axis, resembles the subcritical pattern in figure 25(*a*) for $k_x = 0.1$. There are three vortices in figure 26(*b*): the vortex near the top wall is of smaller extent, but the ones above and below the $y = 0$ axis are of larger extent in the spanwise direction. These vortices repeat along the periodic z-direction, forming an array of vortices, punctuated by a saddle point between two successive vortices in the z-direction. Comparing the density and velocity patterns, we find that the vortices are located around the local density maxima. Looking at the corresponding pattern of granular temperature (not shown), we found that these vortices are born near the local minima of kinetic pressure. It may be noted that the correlation of a vortex core with a low-pressure region is well-known in other fluids (Jeong & Hussain 1995), and the possibility of a similar criterion to identify vortices in granular fluids deserves future investigation.

7.3.2. *Anomalous 2D instability modes in the dilute limit ($\phi^0 = 0.01$)*

Alam (2006) showed that there are additional stationary instabilities in the dilute limit ($\phi^0 < 0.05$), but, in contrast to 3D instabilities discussed in § 7.3.1, the origin of these new instabilities is not tied to pure spanwise perturbations but they are, rather, connected to 2D perturbations (and hence dubbed anomalous, see below) as we demonstrate in this section.

Figures 27(*a*) and (*b*) display the stability diagrams for the stationary ($b^{(0)} = 0$) perturbations for two values of the restitution coefficient $e = 0.99$ and 0.8, respectively; the mean density is set to $\phi^0 = 0.01$ and the Couette gap is $H = 50$. The flow

https://doi.org/10.1017/jfm.2012.549 Published online by Cambridge University Press

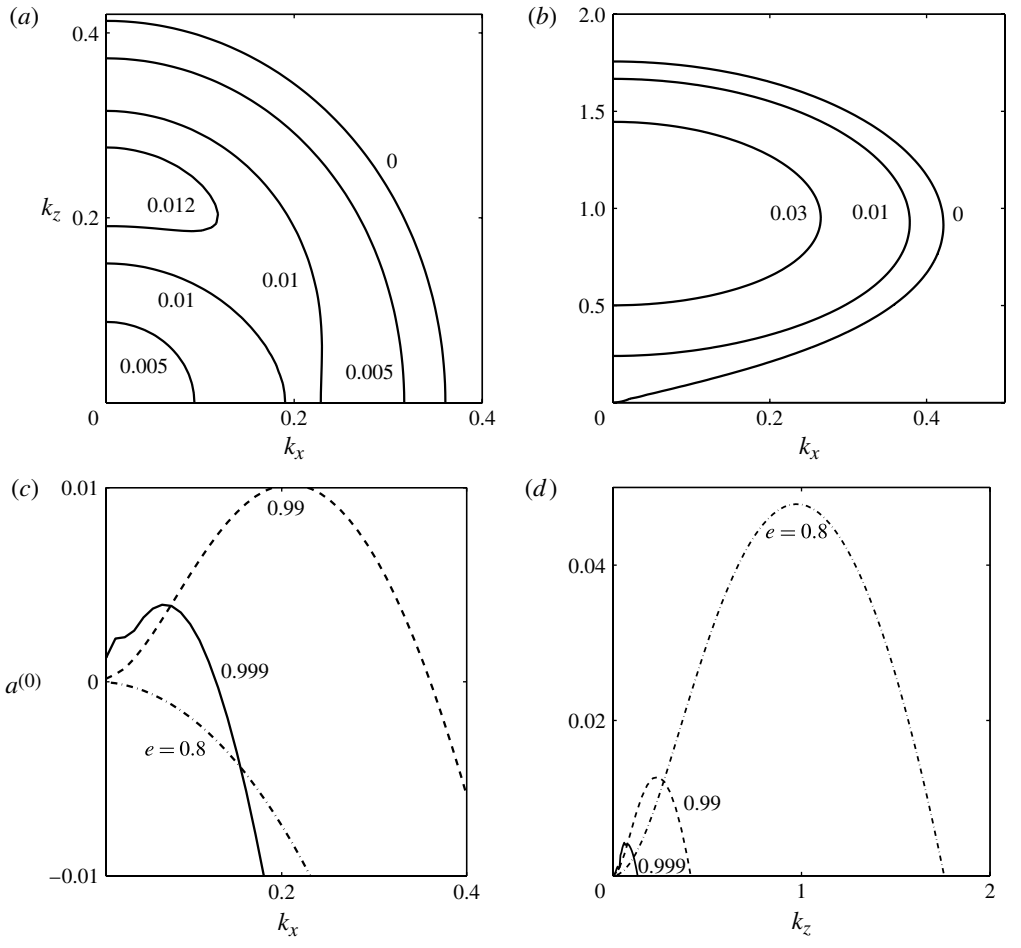


FIGURE 27. Contours of the growth rate ($a^{(0)}$) of the least-stable mode for (*a*) $e = 0.99$ and (*b*) $e = 0.8$. Variations of $a^{(0)}$ with (*c*) k_x for $k_z = 0$ (i.e. 2D perturbations), and with (*d*) k_z for $k_x = 0$ (streamwise-independent perturbations). All are stationary instabilities ($b^{(0)} = 0$) at $\phi^0 = 0.01$ and $H = 50$.

is unstable for a range of (k_x, k_z) inside the neutral/critical contour in each plot. It is interesting to note that the flow is unstable to both $k_x = 0$ (streamwise-independent perturbations) and $k_z = 0$ (2D perturbations) modes at $e = 0.99$, but becomes completely stable to 2D perturbations at $e = 0.8$. For both values of e, the maximum growth rate occurs for streamwise-independent ($k_x = 0$) perturbations. Since these instabilities survive at $k_z = 0$ in the quasi-elastic limit, their origin must be tied to 2D perturbations ($k_z = 0$).

Focusing on 2D perturbations, we show the variations of the growth rate of the least-stable mode with k_x for three values of restitution coefficient in figure 27(*c*). Note that that the growth rate is maximum at $e = 0.99$ (dashed line), decreases both with further increase in $e = 0.999$ (dot-dash line) as well as with further decrease in $e = 0.8$ (solid line). Therefore, these 2D instabilities have an anomalous dependence on inelasticity: the flow is most unstable (i.e. the growth rate is maximum) to 2D perturbations in the quasi-elastic limit ($e \sim 1$), but becomes stable for both perfectly

https://doi.org/10.1017/jfm.2012.549 Published online by Cambridge University Press

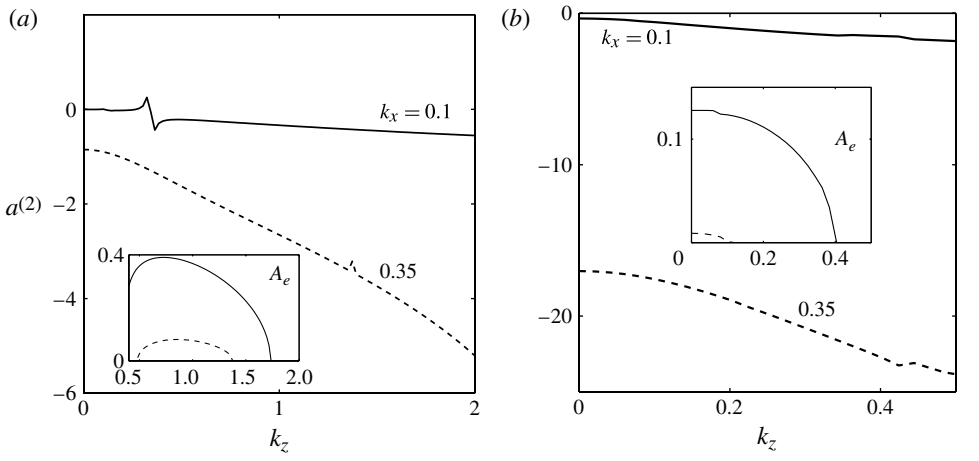


FIGURE 28. Variation of $a^{(2)}$ and A_e (inset), with k_z for $k_x = 0.1$ (solid line) and 0.35 (dashed line). (*a*) $e = 0.8$ and (*b*) $e = 0.99$. Other parameters as in figure 27.

elastic collisions ($e = 1$) as well as below some finite dissipation ($e \sim 0.8$). The latter behaviour is in stark contrast to all other instabilities in granular flows that have finite growth rate at any value of $e < 1$. Interestingly, when spanwise perturbations ($k_z \neq 0$) are incorporated in these instabilities, the dependence of their growth rate on e becomes normal, see figure 27(*d*); more specifically, the growth rate increases with decreasing e and remains positive (and hence unstable) at any $e < 1$. These stationary instabilities in dilute flows are henceforth dubbed *anomalous 2D modes* whose nonlinear behaviour is briefly probed next.

Figures 28(*a*) and 28(*b*) display the variations of the real part of the first Landau coefficient $a^{(2)}$ with spanwise wavenumber k_z for $e = 0.8$ and $e = 0.99$, respectively. In each figure, the solid and dashed lines represent streamwise wavenumbers of $k_x = 0.1$ and $k_x = 0.35$, respectively, with other parameters as in figure 27. For both cases, we find $a^{(2)} < 0$ and $a^{(0)} > 0$(see the growth-rate contours in figure 27*a*,*b*) for a range of k_z over which supercritical finite-amplitude solutions exist as confirmed in the insets of figure 28(*a*,*b*).

The nonlinear density pattern and the vector map of the cross-stream (v', w') velocity in the (y, z^*)-plane (at the $x = 0$ location) are displayed in figure 29 for which $(k_x, k_z) = (0.1, 1.6)$ and $(0.35, 1.0)$ for the upper and lower panels, respectively; other parameters are as in figure 28(*a*). (The patterns for $e = 0.99$ look similar, and hence not shown.) We observe that the dense (white regions) and dilute (black regions) layers of particle clusters span the whole Couette gap across the gradient/transverse direction, leading to columnar-like bands of particles that are inclined at some angle to the walls. To ascertain the true inclination angle of these clusters, the z-axes in figure 29(*a*,*c*) should be stretched by 1.25π and 2π, respectively. Along the dense layers in figure 29(*a*,*c*), the cross-stream motion is dominated by a saddle point, see the curved arrows in figure 29(*b*,*d*). The overall structural features of these patterns (that originate from anomalous 2D modes) are significantly different from those originating from other instability modes that have been discussed so far. The robustness of the columnar patterns was further checked with another set of constitutive relations for f_1–f_5 (see (A 6)–(A 11) in appendix A): they persist for both

https://doi.org/10.1017/jfm.2012.549 Published online by Cambridge University Press

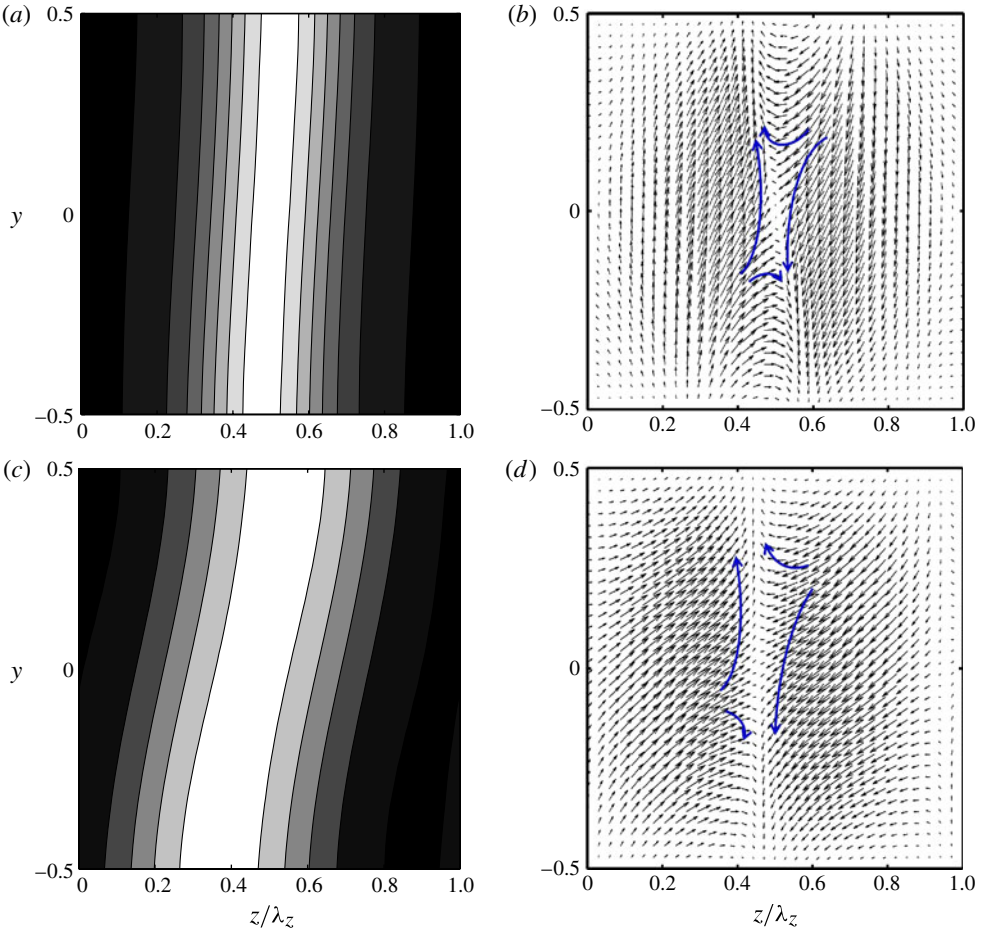


FIGURE 29. (Colour online) Stationary patterns of (*a*,*c*) perturbation density and (*b*,*d*) (v', w') velocity in the (y, z^*)-plane at $x = 0$ for $\phi^0 = 0.01$, $H = 50$ and $e = 0.8$. (*a*,*b*) $k_x = 0.1$ and $k_z = 1.6$; (*c*,*d*) $k_x = 0.35$ and $k_z = 1.0$.

cases for the same parameter set. However, the physical origin of these anomalous modes and the resulting columnar density bands remain unclear at present.

8. Discussion: implications for large-scale particle simulations

Let us now briefly discuss our predicted nonlinear instability patterns from the viewpoint of particle simulations of 3D granular plane Couette flow. For parameter combinations of dominant SW and TW instabilities in figures 4 and 12, respectively, the mean density is $\phi^0 = 0.2$, with a Couette gap of $H = \bar{l}_y/\bar{d} = 100$: the streamwise wavenumbers are $k_x = 0.58$ and $k_x = 0.97$, respectively, and the spanwise wavenumber is $k_z = 1$ for both modes. With these parameters and referring to figure 1, the dimensions of the Couette cell $(\bar{l}_x/\bar{d},\ \bar{l}_y/\bar{d},\ \bar{l}_z/\bar{d})$ would be $(1083, 100, 628)$ and $(668, 100, 628)$ for SW and TW modes, respectively, that correspond to a total number of particles of 8.16798×10^7 and 5.03982×10^7. For the purely 3D instabilities in dilute flows ($\phi^0 = 0.05$, with $H = 100$) as in figures 25(*a*, *b*), 25(*c*, *d*) and 25(*e*, *f*), we have

https://doi.org/10.1017/jfm.2012.549 Published online by Cambridge University Press

$k_z = 0.2$, 2 and 12, respectively, with a streamwise wavenumber of $k_x = 0.1$; hence the dimensions of the box (l_x/d, l_y/d, l_z/d) would be (6283, 100, 3146), (6283, 100, 314) and (6283, 100, 63) that correspond to a total number of particles of 5.9215×10^8, 5.9215×10^7 and 0.9869×10^7, respectively. These estimates suggest that we need very large-scale simulations with $O(10^7)$ particles. Note that all these predictions hold for a restitution coefficient of 0.8. We have verified that on decreasing the restitution coefficient to 0.6, both the dominant SW and TW instabilities occurred at a lower value of $H = 50$ which can be translated to a decrease in the total number of particles by an order of magnitude to $O(10^6)$. None of the published works on 3D shear flow reported such large-scale simulations, and hence a comparison between theory and simulation is not possible at present. It is clear from above discussion that for all cases we need to carry out particle simulations in a non-cubic box that would fit the wavenumbers (k_x and k_z) corresponding to a specific instability mode with the number of particles exceeding $O(10^6)$.

The simulations of Conway & Glasser (2004) are close our work; they reported gradient banding, vorticity banding, density waves and coherent vortices in granular Couette flow. All of their 3D simulations were done for a Couette gap of $H = 50$, with a mean density of $\phi^0 = 0.05$ and a restitution coefficient of 0.6, but the total number of particles was about $O(10^5)$ or less. They varied the streamwise and spanwise lengths of the box (which is equivalent to changing the wavenumbers along respective directions) so as to accommodate different instability modes. They showed that the near 3D Couette ($l_z \ll l_y$) flow preserves the instabilities of 2D flow as we found. One particular pattern from their simulations in dilute flows that corresponds to the banding of particles (in the form of rolls) along the spanwise/vorticity direction compares well with the predictions of our nonlinear theory (Shukla & Alam 2012). A single cross-stream 2D plug structure has been found as the depth of the Couette cell increases. They also found the existence of streamwise vortices by following the pathline of a single tracer particle which got entrapped inside a vortex. This agrees with the persistence of vortical patterns that we have found from the analyses of the cross-stream velocity and the streamwise vorticity.

As illustrated in §§ 7.1–7.3, the vortical motion on the cross-stream plane can be described in terms of the fixed/critical/stationary points of the underlying (v', w') flow field: saddles, nodes and focus/vortex. Following the success of such critical-point diagnostics in the shear flow of Newtonian fluids (Perry & Chong 1987), we suggest characterizing the 3D steady/unsteady granular flows in terms of fixed points – this can be easily done by analysing data from particle simulations. The coarse-grained velocity gradient tensor as well as its invariants can be extracted from simulations so as to classify the complex topology of the flow in terms of different types of fixed points and this would help to identify coherent/vortical structures in granular shear flows. Such simulations should be carried out for a range of densities spanning from the dilute to dense regimes to track all types of instabilities reported here. We hope this work will inspire others to carry out very large-scale simulations of 3D plane Couette flow in an effort to characterize the complex 3D eddying motion that can be compared with our predictions of nonlinear stability analysis. To minimize the computational cost of such simulations, a minimal flow unit can be conceived in order to track a particular instability mode whose wavenumbers will dictate the minimum size of the computational box ($\bar{l}_x/\bar{d} \equiv 2\pi/k_x^*$, $\bar{l}_z/\bar{d} \equiv 2\pi/k_z^*$ and $l_y/d = H$, where $k_i^* = k_i/H$, with $i = x, z$, is the respective wavenumber scaled in terms of particle diameter).

https://doi.org/10.1017/jfm.2012.549 Published online by Cambridge University Press

9. Summary and conclusion

Using Navier–Stokes-level hydrodynamic equations of rapid granular flows, we have investigated the nonlinear stability of 3D granular plane Couette flow for the first time. A previously developed order-parameter theory for 2D perturbations (Shukla & Alam 2011*a*,*b*) has been extended to 3D perturbations to arrive at the pertinent Landau–Stuart equation. Essentially, the nonlinear stability problem has been reduced to a sequence of linear problems at different orders in perturbation amplitude (A): (i) the fundamental mode at $O(A)$ which is simply the linear stability problem; (ii) the second harmonic and the distortion of mean flow at $O(A^2)$; (iii) the distortion of fundamental and the third harmonic at $O(A^3)$; and (iv) the subsequent higher-order harmonics. The differential equations for the modal amplitudes have been solved using a spectral-based numerical scheme that dealt with three specific types of problem: (i) the solution of a differential eigenvalue problem; (ii) the solution of inhomogeneous differential equations; and (iii) the evaluation of two definite integrals that yields the Landau coefficients. Stopping at cubic-order $O(A^3)$, we calculated the first Landau coefficient which is the leading-order nonlinear term in the Landau–Stuart equation.

The granular plane Couette flow is known to support a variety of SW and TW instabilities (Alam 2006), having wave-like modulations along both the streamwise (x) and spanwise/vorticity (z) directions (characterized by streamwise and spanwise wavenumber, k_x and k_z, respectively): (*a*) the *dominant* SW and TW instabilities (having the largest growth rate among all types of SW and TW instabilities) that appear at $k_x = O(1)$; (*b*) the *long-wave* SW and TW instabilities at $k_x \sim 0$ (i.e. the perturbations having large wavelengths along the streamwise direction, i.e. $\lambda_x = 2\pi/k_x \gg 1$); and (*c*) *purely 3D* SW and TW instabilities. The first two classes of instabilities originate from 2D perturbations ($k_z = 0$) and they exists for a range of densities spanning from moderately dense to dense flows. The last class of instabilities has its origin in 3D perturbations in dilute flows ($\phi^0 < 0.1$) and the flow is linearly stable to 2D perturbations in dilute flows. The effects of 3D perturbations ($k_z \neq 0$ and $k_x \neq 0$) on the finite-amplitude saturation of the above mentioned five types of instability modes, the nature of their bifurcations and the resulting nonlinear patterns have been analysed and contrasted with our previous study (Shukla & Alam 2011*b*) on 2D nonlinear perturbations. In addition, a first attempt has been made to analyse the nonlinear flow patterns in terms of the fixed/critical points (saddles, nodes and focus/vortex) of the underlying velocity field in order to ascertain the existence of vortices in this flow.

As in the case of 2D perturbations, we found evidence of mean-flow resonance for 3D perturbations in the near-critical regime of flows at all densities – the first Landau coefficient diverges at such resonance points. The origin of this resonance is shown to be tied to the interaction between a linear stability mode and a mean-flow mode (i.e. the one having no variation along either streamwise or spanwise directions). For a given parameter combination of mean density (ϕ^0) and Couette gap (H), we uncovered the coexistence of multiple nonlinear states of stationary and travelling waves, depending on the values of wavenumbers (k_x and k_z).

For both the dominant SW and TW instabilities, the 3D nonlinear solutions are born via supercritical pitchfork and Hopf bifurcations, respectively, for a range of spanwise wavenumbers up to $k_z = O(1)$. The 3D patterns of perturbation density in the shear plane are found to be markedly different from their 2D counterparts for both modes. The cross-stream (v', w') velocity field in the (y, z)-plane contains a vortex in the background of saddle-node-type motions (i.e. the flow is dominated by saddle points and nodes, such as sources and sinks). The vortical motion appears

https://doi.org/10.1017/jfm.2012.549 Published online by Cambridge University Press

to be driven by two nearby saddle points, and the location of this vortex is found to be correlated with the local maxima of the perturbation streamwise vorticity. The presence of strong streamwise vorticity seems to be responsible for the occurrence of more tenuous/inhomogeneous particle clusters in 3D flows as well as for the stretching of clusters with increasing spanwise wavenumber for both the dominant SW and TW instabilities.

Beyond a moderate value of the mean density ($\phi^0 \sim 0.15$), there are SW linear instability modes for a very small range of streamwise wavenumbers $k_x \sim 0$. The origin of these long-wave instabilities is tied to the underlying gradient-banding instability ($k_x = 0$ and $k_z = 0$). These modes remain unstable for a range of spanwise wavenumbers $k_z = O(1)$, yielding nonlinear stationary states via pitchfork bifurcations. These long-wave stationary instabilities subsequently give birth to TW instabilities (at $k_x \sim 0$) that are responsible for the genesis of nonlinear oscillatory states via Hopf bifurcations. For both of these long-wave instability modes, the bifurcations are supercritical for 2D perturbations (Shukla & Alam 2011*b*) and remain supercritical for 3D perturbations. The density patterns of the long-wave TW instabilities are found to be structurally different from those that originate from dominant TW instabilities (that occur at $k_x \sim O(1)$) with respect to both large- and small-scale features.

For dense flows too, the above SW instability at long waves persists having similar nonlinear behaviour. However, we found two types of supercritical TW solutions in the dense regime: one for small k_z ($\sim$0) and the other for moderate values of $k_z = O(1)$; the former originates from 2D perturbations and the latter from 3D perturbations. In dense flows, we also uncovered subcritical TW solutions at $k_z = O(1)$ which originate from 3D perturbations at small values of k_x. The related nonlinear density patterns are found to be different from those that occur at moderate densities with respect to the orientation of particle clusters/bands. For all long-wave instabilities that occur in moderately dense to dense regimes, the flow on the cross-stream plane is largely dominated by nodes (sources and sinks) and saddles.

For purely 3D SW and TW instabilities (having no analogue in 2D flows) that exist only in dilute flows, we found both supercritical and subcritical finite-amplitude solutions for a much larger range of spanwise wavenumbers $k_z = O(10)$. At small values of k_x, we uncovered a change-over in the modal hierarchy with varying k_z which is responsible for the observed differences in nonlinear TW patterns. While the cross-stream velocity field for supercritical solutions contains nodes (sources and sinks) and saddles, the subcritical solutions are dominated by large-scale vortices in the background of saddle-node-type motions. The density patterns for the two cases are also found to be different in the cross-stream plane: while the supercritical solutions have particle clusters positioned at some oblique angle to the spanwise direction, the subcritical solutions have modulated clusters almost parallel to the spanwise direction. Lastly, for the anomalous 2D instability modes in the dilute limit, the dense and dilute layers of particles span across the Couette gap, leading to columnar-like particle bands over which the saddle-type motion of the cross-stream velocity persists. In all cases, the vortices correspond to a local maximum of streamwise vorticity.

It is recommended to use critical-point concepts from dynamical systems theory to analyse the velocity gradient tensor in terms of its invariants or other related measures (Perry & Chong 1987; Jeong & Hussain 1995) which is likely to help to identify the large-scale vortical structures in this flow. Another avenue in the search for streamwise vortices in granular shear flow is to examine the optimal perturbations (that are responsible for maximum amplification of perturbation energy) using non-modal stability analyses (Malik *et al.* 2006, 2008). The present work should

https://doi.org/10.1017/jfm.2012.549 Published online by Cambridge University Press

be complemented with large-scale simulations with $O(10^8)$ particles as discussed in § 8 to uncover the rich dynamics in 3D granular Couette flow. The effects of non-uniform shear flow (Alam & Nott 1998; Alam *et al.* 2005) and slip boundary conditions (Jenkins & Richman 1986; Chikkadi & Alam 2009) should be probed so as to understand the generality of the predicted pattern formation scenario in granular plane Couette flow. It may be noted that the rheology of granular fluids is known to be non-Newtonian, characterized by large normal stress differences if the collisional dissipation is large (Alam & Luding 2003, 2005). Therefore, more accurate constitutive relations having a larger range of validity in terms of inelasticity (Jenkins & Richman 1985; Sela & Goldhirsch 1998; Garzo *et al.* 2007; Noskowicz *et al.* 2007) should also be tested and compared with the present results. The order-parameter theory developed in § 4 can be easily adapted to granular flows described by Newtonian/non-Newtonian constitutive models with different boundary conditions (slip/non-slip and adiabatic/non-adiabatic boundary conditions (Alam & Nott 1998; Chikkadi & Alam 2009) as well as with gravity (Alam *et al.* 2005). The present work is thus a stepping stone to initiate future studies on 3D nonlinear instabilities and the related pattern formation scenario in various types of granular flows (granular Poiseuille flow, inclined chute flow, granular convection, etc.). Work in this direction is in progress.

Acknowledgements

M.A. gratefully acknowledges the funding support from the Department of Atomic Energy, Government of India (DAE/MA/4265) through DAE-SRC 'Outstanding Research Investigator Award'.

Appendix A. Constitutive relations for $f_1(\phi, e)$–$f_5(\phi, e)$

For all calculations in this paper, the dimensionless functions $f_1 - f_5$ as defined in (2.10) are taken to have following forms:

$$f_1(\phi) = \phi(1 + 4\phi\chi), \tag{A 1}$$

$$f_2(\phi) = \frac{5\sqrt{\pi}}{96\chi}\left(1 + \frac{8}{5}\phi\chi\right)^2 + \frac{8}{5\sqrt{\pi}}\phi^2\chi, \tag{A 2}$$

$$f_3(\phi) = \frac{8}{3\sqrt{\pi}}\phi^2\chi, \tag{A 3}$$

$$f_4(\phi) = \frac{25\sqrt{\pi}}{128\chi}\left(1 + \frac{12}{5}\phi\chi\right)^2 + \frac{4}{\sqrt{\pi}}\phi^2\chi, \tag{A 4}$$

$$f_5(\phi, e) = \frac{12}{\sqrt{\pi}}(1 - e^2)\phi^2\chi, \tag{A 5}$$

where $\chi(\phi)$ is the radial distribution function (2.11). Note that inelastic nature of collisions is reflected only in the expression for the collisional dissipation rate ($\mathcal{D}$) which is proportional to $(1 - e^2)$ that vanishes in the elastic limit $e \to 1$.

All linear stability results presented in this paper (yielding five distinct instability modes as discussed in § 7) have also been checked by using following constitutive

https://doi.org/10.1017/jfm.2012.549 Published online by Cambridge University Press

relations of Lun *et al.* (1984):

$$f_1(\phi, e) = \phi(1 + 4\eta\phi\chi(\phi)), \tag{A 6}$$

$$f_2(\phi, e) = \frac{5\sqrt{\pi}}{96\eta(2-\eta)}\left(1 + \frac{8}{5}\eta\phi\chi(\phi)\right)\left(\frac{1}{\chi(\phi)} + \frac{8}{5}\eta(3\eta - 2)\phi\right) + \frac{8}{5\sqrt{\pi}}\eta\phi^2\chi(\phi), \tag{A 7}$$

$$f_3(\phi, e) = \frac{8}{3\sqrt{\pi}}\eta\phi^2\chi(\phi), \tag{A 8}$$

$$f_4(\phi, e) = \frac{25\sqrt{\pi}}{16\eta(41 - 33\eta)}\left(1 + \frac{12}{5}\eta\phi\chi(\phi)\right)\left(\frac{1}{\chi(\phi)} + \frac{12}{5}\eta^2(4\eta - 3)\phi\right) + \frac{4}{\sqrt{\pi}}\eta\phi^2\chi(\phi), \tag{A 9}$$

$$f_{4h}(\phi, e) = \frac{15\sqrt{\pi}}{4\eta(41 - 33\eta)}\left(\frac{1}{\phi\chi(\phi)} + \frac{12}{5}\eta\right)\eta(2\eta - 1)(\eta - 1)\frac{\mathrm{d}}{\mathrm{d}\phi}(\phi^2\chi(\phi)), \tag{A 10}$$

$$f_5(\phi, e) = \frac{48}{\sqrt{\pi}}\eta(1 - \eta)\phi^2\chi(\phi), \tag{A 11}$$

where

$$\eta = \frac{(1 + e)}{2}. \tag{A 12}$$

In particular, Alam (2006) used the above set of constitutive relations (A 6)–(A 11) that account for a non-Fourier term ($f_{4h} \neq 0$) in the heat flux, along with the dependence of f_1–f_4 on the restitution coefficient (e). Comparing the linear stability results of Alam (2006) with those reported in the present paper using (A 1)–(A 5), we have drawn two conclusions: (i) all five instability modes of Alam (2006) have been reproduced using the first set of minimal constitutive relations (A 1)–(A 5); and (ii) therefore the non-Fourier term in the heat flux (f_{4h}) does not introduce any new instability in granular plane Couette flow. The differences appear only in the value of the growth rate of the unstable mode and the range of wavenumbers (k_x and k_z) over which each instability mode survives for specified values of the mean density (ϕ^0), the Couette gap (H) and the restitution coefficient (e). For example, (a) the growth rates are relatively lower and (b) the unstable ranges of k_x and k_z are slightly smaller for the present constitutive relations (A 1)–(A 5) in comparison to those obtained using (A 6)–(A 11).

Since our nonlinear analysis tracks each of the above five linear instability modes, we expect our nonlinear results to hold even for the case of the second set of constitutive expressions (A 6)–(A 11). It may be noted that other sets of constitutive expressions for f_1–f_5 can be obtained from the works of other researchers (Jenkins & Richman 1985; Sela & Goldhirsch 1998; Garzo *et al.* 2007; Noskowicz *et al.* 2007). A comparative nonlinear analysis of the present problem using different constitutive relations is recommended for a future work.

https://doi.org/10.1017/jfm.2012.549 Published online by Cambridge University Press

Appendix B. Linear stability operator and its adjoint

The elements of the linear stability operator, $\boldsymbol{\mathcal{L}} = [l_{ij}]$, are given by

$$l_{11} = -u^0 \frac{\partial}{\partial x}, \quad l_{12} = -\phi^0 \frac{\partial}{\partial x}, \quad l_{13} = -\left[\phi^0_y + \phi^0 \frac{\partial}{\partial y}\right], \quad l_{14} = -\phi^0 \frac{\partial}{\partial z}, \quad l_{15} = 0, \tag{B 1}$$

$$l_{21} = \frac{1}{H^2\phi^0}\left[-p^0_\phi \frac{\partial}{\partial x} + u^0_y\left(\mu^0_{\phi y} + \mu^0_\phi \frac{\partial}{\partial y}\right) + u^0_{yy}\mu^0_\phi\right], \tag{B 2}$$

$$l_{22} = -u^0 \frac{\partial}{\partial x} + \frac{1}{H^2\phi^0}\left[(2\mu^0 + \lambda^0)\frac{\partial^2}{\partial x^2} + \mu^0\left(\frac{\partial^2}{\partial y^2} + \frac{\partial^2}{\partial z^2}\right) + \mu^0_y \frac{\partial}{\partial y}\right], \tag{B 3}$$

$$l_{23} = -u^0_y + \frac{1}{H^2\phi^0}\left[(\mu^0 + \lambda^0)\frac{\partial^2}{\partial x \partial y} + \mu^0_y \frac{\partial}{\partial x}\right], \quad l_{24} = \frac{(\mu^0 + \lambda^0)}{H^2\phi^0}\frac{\partial^2}{\partial x \partial z}, \tag{B 4}$$

$$l_{25} = \frac{1}{H^2\phi^0}\left[-p^0_T \frac{\partial}{\partial x} + u^0_y\left(\mu^0_{Ty} + \mu^0_T \frac{\partial}{\partial y}\right) + u^0_{yy}\mu^0_T\right], \tag{B 5}$$

$$l_{31} = \frac{1}{H^2\phi^0}\left[-\left(p^0_{\phi y} + p^0_\phi \frac{\partial}{\partial y}\right) + u^0_y \mu^0_\phi \frac{\partial}{\partial x}\right], \tag{B 6}$$

$$l_{32} = \frac{1}{H^2\phi^0}\left[\lambda^0_y \frac{\partial}{\partial x} + (\lambda^0 + \mu^0)\frac{\partial^2}{\partial x \partial y}\right], \tag{B 7}$$

$$l_{33} = -u^0 \frac{\partial}{\partial x} + \frac{1}{H^2\phi^0}\left[(2\mu^0_y + \lambda^0_y)\frac{\partial}{\partial y} + (2\mu^0 + \lambda^0)\frac{\partial^2}{\partial y^2} + \mu^0\left(\frac{\partial^2}{\partial z^2} + \frac{\partial^2}{\partial x^2}\right)\right], \tag{B 8}$$

$$l_{34} = \frac{1}{H^2\phi^0}\left[\lambda^0_y \frac{\partial}{\partial z} + (\lambda^0 + \mu^0)\frac{\partial^2}{\partial z \partial y}\right], \tag{B 9}$$

$$l_{35} = \frac{1}{H^2\phi^0}\left[-\left(p^0_{Ty} + p^0_T \frac{\partial}{\partial y}\right) + u^0_y \mu^0_T \frac{\partial}{\partial x}\right], \quad l_{41} = \frac{-p^0_\phi}{H^2\phi^0}\frac{\partial}{\partial z}, \tag{B 10}$$

$$l_{42} = \frac{(\mu^0 + \lambda^0)}{H^2\phi^0}\frac{\partial^2}{\partial x \partial z}, \quad l_{43} = \frac{1}{H^2\phi^0}\left[(\mu^0 + \lambda^0)\frac{\partial^2}{\partial y \partial z} + \mu^0_y \frac{\partial}{\partial z}\right], \tag{B 11}$$

$$l_{44} = -u^0 \frac{\partial}{\partial x} + \frac{1}{H^2\phi^0}\left[(2\mu^0 + \lambda^0)\frac{\partial^2}{\partial z^2} + \mu^0\left(\frac{\partial^2}{\partial x^2} + \frac{\partial^2}{\partial y^2}\right) + \mu^0_y \frac{\partial}{\partial y}\right], \tag{B 12}$$

$$l_{45} = \frac{-p^0_T}{H^2\phi^0}\frac{\partial}{\partial z}, \tag{B 13}$$

$$l_{51} = \frac{2}{3\phi^0 H^2}\left[T^0_{yy}\kappa^0_\phi + T^0_y\left(\kappa^0_\phi \frac{\partial}{\partial y} + \kappa^0_{\phi y}\right)\right] + \frac{2(u^{0^2}_y \mu^0_\phi - \mathcal{D}^0_\phi)}{3\phi^0}, \tag{B 14}$$

$$l_{52} = \frac{2}{3\phi^0}\left[-p^0 \frac{\partial}{\partial x} + 2\mu^0 u^0_y \frac{\partial}{\partial y}\right], \quad l_{53} = -T^0_y + \frac{2}{3\phi^0}\left[-p^0 \frac{\partial}{\partial y} + 2\mu^0 u^0_y \frac{\partial}{\partial x}\right], \tag{B 15}$$

$$l_{54} = -\frac{2p^0}{3\phi^0}\frac{\partial}{\partial z}, \tag{B 16}$$

$$l_{55} = -u^0 \frac{\partial}{\partial x} + \frac{2}{3\phi^0 H^2}\left[\kappa^0\left(\frac{\partial^2}{\partial x^2} + \frac{\partial^2}{\partial y^2} + \frac{\partial^2}{\partial z^2}\right) + \kappa^0_y \frac{\partial}{\partial y} + \kappa^0_T T^0_{yy}\right. \tag{B 17}$$

$$\left. + T^0_y\left(\kappa^0_T \frac{\partial}{\partial y} + \kappa^0_{Ty}\right)\right] + \frac{2(\mu^0_T u^{0^2}_y - \mathcal{D}^0_T)}{3\phi^0}. \tag{B 18}$$

https://doi.org/10.1017/jfm.2012.549 Published online by Cambridge University Press

The subscripts y, ϕ and T on any quantity denote its partial derivative with respect y, ϕ and T, respectively, and the superscript 0 denotes its value at base-state conditions. The elements of the linear operator, $\boldsymbol{L}$, as defined in (3.8) and (3.9) can be obtained from those of $\boldsymbol{\mathcal{L}}$ by replacing $\partial^j/\partial x^j \to (\mathrm{i}k_x)^j$ and $\partial^j/\partial z^j \to (\mathrm{i}k_z)^j$.

The elements of the adjoint linear operator, $\boldsymbol{L}^\dagger = [l^\dagger_{ij}]$, are given by

$$l^\dagger_{11} = \mathrm{i}k_x u^0, \quad l^\dagger_{12} = \frac{\mathrm{i}k_x p^0_\phi}{\phi^0 H^2} - \frac{u^0_y \mu^0_\phi (\phi^0 d_y - \phi^0_y)}{(\phi^0 H)^2}, \tag{B 19}$$

$$l^\dagger_{13} = \frac{-\mathrm{i}k_x u^0_y \mu^0_\phi}{\phi^0 H^2} + \frac{p^0_\phi (\phi^0 d_y - \phi^0_y)}{(\phi^0 H)^2}, \quad l^\dagger_{14} = \frac{\mathrm{i}p^0_\phi k_z}{\phi^0 H^2}, \tag{B 20}$$

$$l^\dagger_{15} = \frac{2(\mu^0_\phi (u^0_y)^2 - \mathcal{D}^0_\phi)}{3\phi^0} - \frac{2T^0_y \kappa^0_\phi d_y}{3\phi^0 H^2} + \frac{2\phi^0_y T^0_y \kappa^0_\phi}{3(\phi^0 H)^2}, \quad l^\dagger_{21} = \mathrm{i}k_x \phi^0, \tag{B 21}$$

$$l^\dagger_{22} = \mathrm{i}k_x u^0 - \frac{k_x^2(2\mu^0 + \lambda^0) + \mu^0 k_z^2}{\phi^0 H^2} + \frac{1}{(\phi^0 H)^2}\left[-\mu^0_y \phi^0_y - \mu^0 \phi^0_{yy} + \frac{2(\phi^0_y)^2 \mu^0}{\phi^0} + (\phi^0 \mu^0_y - 2\phi^0_y \mu^0) d_y + \phi^0 \mu^0 d_y^2\right], \tag{B 22}$$

$$l^\dagger_{23} = \frac{\mathrm{i}k_x\left[(\mu^0 + \lambda^0)(\phi^0 d_y - \phi^0_y) + \phi^0 \mu^0_y\right]}{(\phi^0 H)^2}, \quad l^\dagger_{24} = -\frac{(\mu^0 + \lambda^0) k_x k_z}{\phi^0 H^2}, \tag{B 23}$$

$$l^\dagger_{25} = \frac{2\mathrm{i}k_x p^0}{3\phi^0} - \frac{4}{3(\phi^0)^2}[\phi^0(\mu^0 u^0_y d_y + \mu^0_y u^0_y + \mu^0 u^0_{yy}) - \phi^0_y \mu^0 u^0_y], \tag{B 24}$$

$$l^\dagger_{31} = \phi^0 d_y, \quad l^\dagger_{32} = -u^0_y + \frac{\mathrm{i}k_x\left[(\mu^0 + \lambda^0)(\phi^0 d_y - \phi^0_y) + \phi^0 \lambda^0_y\right]}{(\phi^0 H)^2}, \tag{B 25}$$

$$l^\dagger_{33} = \mathrm{i}k_x u^0 - \frac{\mu^0(k_x^2 + k_z^2)}{\phi^0 H^2} + \frac{1}{(\phi^0 H)^2}\left[-(2\mu^0_y + \lambda^0_y)\phi^0_y - (2\mu^0 + \lambda^0)\phi^0_{yy} + \phi^0(2\mu^0_y + \lambda^0_y) d_y - 2(2\mu^0 + \lambda^0)\phi^0_y d_y + \phi^0(2\mu^0 + \lambda^0) d_y^2\right] + \frac{2(\phi^0_y)^2(2\mu^0 + \lambda^0)}{(\phi^0)^3 H^2}, \tag{B 26}$$

$$l^\dagger_{34} = \frac{\mathrm{i}k_z\left[(\mu^0 + \lambda^0)(\phi^0 d_y - \phi^0_y) + \phi^0 \lambda^0_y\right]}{(\phi^0 H)^2}, \tag{B 27}$$

$$l^\dagger_{35} = -T^0_y - \frac{4\mathrm{i}k_x \mu^0 u^0_y}{3\phi^0} + \frac{2(\phi^0(p^0 d_y + p^0_y) - \phi^0_y p^0)}{3(\phi^0)^2}, \tag{B 28}$$

$$l^\dagger_{41} = \mathrm{i}k_z \phi^0, \quad l^\dagger_{42} = -\frac{(\lambda^0 + \mu^0) k_x k_z}{\phi^0 H^2}, \tag{B 29}$$

$$l^\dagger_{43} = \frac{\mathrm{i}k_z\left[(\mu^0 + \lambda^0)(\phi^0 d_y - \phi^0_y) + \phi^0 \mu^0_y\right]}{(\phi^0 H)^2}, \tag{B 30}$$

$$l^\dagger_{44} = \mathrm{i}k_x u^0 - \frac{k_z^2(2\mu^0 + \lambda^0) + \mu^0 k_x^2}{\phi^0 H^2} + \frac{1}{(\phi^0 H)^2}\left[-\mu^0_y \phi^0_y - \mu^0 \phi^0_{yy} + \frac{2(\phi^0_y)^2 \mu^0}{\phi^0} + (\phi^0 \mu^0_y - 2\phi^0_y \mu^0) d_y + \phi^0 \mu^0 d_y^2\right], \quad l^\dagger_{45} = \frac{2\mathrm{i}p^0 k_z}{3\phi^0}, \tag{B 31}$$

https://doi.org/10.1017/jfm.2012.549 Published online by Cambridge University Press

$$l_{51}^{\dagger}=0,\quad l_{52}^{\dagger}=\frac{\mathrm{i}k_x p_T^0}{\phi^0 H^2}-\frac{(\phi^0 u_y^0 \mu_T^0 d_y-\phi_y^0 \mu_T^0 u_y^0)}{(\phi^0 H)^2}, \tag{B 32}$$

$$l_{53}^{\dagger}=\frac{-\mathrm{i}k_x u_y^0 \mu_T^0}{\phi^0 H^2}+\frac{(\phi^0 p_T^0 d_y-\phi_y^0 p_T^0)}{(\phi^0 H)^2},\quad l_{54}^{\dagger}=\frac{\mathrm{i}p_T^0 k_z}{\phi^0 H^2}, \tag{B 33}$$

$$\begin{aligned} l_{55}^{\dagger}=&\,\mathrm{i}k_x u^0+\frac{2}{3\phi^0}\left[-\frac{1}{H^2}(k_x^2+k_z^2)\kappa^0+\mu_T^0\left(u_y^0\right)^2-\mathcal{D}_T^0\right]+\frac{4\left(\phi_y^0\right)^2\kappa^0}{3H^2\left(\phi^0\right)^3}\\ &+\frac{2}{3\left(\phi^0 H\right)^2}\left[\phi_y^0 T_y^0 \kappa_T^0-\phi_{yy}^0\kappa^0-\phi_y^0\kappa_y^0\right.\\ &\left.+(\phi^0\kappa_y^0-\phi^0 T_y^0\kappa_T^0-2\phi_y^0\kappa^0)d_y+\phi^0\kappa^0 d_y^2\right]. \end{aligned} \tag{B 34}$$

In the above, $d_y\equiv \mathrm{d}/\mathrm{d}y$ and $d_y^2\equiv \mathrm{d}^2/\mathrm{d}y^2$ represent first and second derivatives with respect to y, respectively.

Appendix C. Nonlinear terms in the perturbation equations

The perturbation form of the nonlinear mass balance equation and the expression for its quadratic nonlinearity are given by

$$\frac{\partial\phi'}{\partial t}=-\left[u^0\frac{\partial\phi'}{\partial x}+\left(\phi_y^0+\phi^0\frac{\partial}{\partial y}\right)v'+\phi^0\frac{\partial u'}{\partial x}+\phi^0\frac{\partial w'}{\partial z}\right]+\mathcal{N}_2^1, \tag{C 1}$$

$$\mathcal{N}_2^1=-\left[\frac{\partial(\phi' u')}{\partial x}+\frac{\partial(\phi' v')}{\partial y}+\frac{\partial(\phi' w')}{\partial z}\right]. \tag{C 2}$$

Note that the quadratic and cubic nonlinear terms are designated by subscripts 2 and 3, respectively, and the superscripts 1, 2, 3, 4 and 5 on $\mathcal{N}_i^j$ refer to terms originating from the continuity, x-momentum, y-momentum, z-momentum and energy equations, respectively.

Quadratic ($\mathcal{N}_2^3$) and cubic ($\mathcal{N}_3^3$) nonlinear terms in the x-momentum equation

$$\begin{aligned} (\phi^0 H^2)\mathcal{N}_2^2=&-H^2\left[\phi^0(\boldsymbol{u}'\cdot\boldsymbol{\nabla})u'+\phi'\left(\frac{\partial u'}{\partial t}+u^0\frac{\partial u'}{\partial x}+u_y^0 v'\right)\right]\\ &-\left(\frac{1}{2}p_{\phi\phi}^0\frac{\partial\phi'^2}{\partial x}+\frac{1}{2}p_{TT}^0\frac{\partial T'^2}{\partial x}+p_{\phi T}^0\frac{\partial\phi' T'}{\partial x}\right)+2(\mu_\phi^0\phi'+\mu_T^0 T')\frac{\partial^2 u'}{\partial x^2}\\ &+2\left(\mu_\phi^0\frac{\partial\phi'}{\partial x}+\mu_T^0\frac{\partial T'}{\partial x}\right)\frac{\partial u'}{\partial x}+(\lambda_\phi^0\phi'+\lambda_T^0 T')\frac{\partial(\boldsymbol{\nabla}\cdot\boldsymbol{u}')}{\partial x}\\ &+\left(\lambda_\phi^0\frac{\partial\phi'}{\partial x}+\,+\lambda_T^0\frac{\partial T'}{\partial x}\right)(\boldsymbol{\nabla}\cdot\boldsymbol{u}')\\ &+\left(\frac{1}{2}\mu_{\phi\phi}^0\phi'^2+\frac{1}{2}\mu_{TT}^0 T'^2+\mu_{\phi T}^0\phi' T'\right)u_{yy}^0\\ &+(\mu_\phi^0\phi'+\mu_T^0 T')\frac{\partial}{\partial y}\left(\frac{\partial u'}{\partial y}+\frac{\partial v'}{\partial x}\right)\\ &+u_y^0\left(\frac{1}{2}\mu_{\phi\phi y}^0\phi'^2+\frac{1}{2}\mu_{\phi\phi}^0\frac{\partial\phi'^2}{\partial y}\right.\\ &\left.+\frac{1}{2}\mu_{TTy}^0 T'^2+\frac{1}{2}\mu_{TT}^0\frac{\partial T'^2}{\partial y}+\mu_{\phi Ty}^0\phi' T'+\mu_{\phi T}^0\frac{\partial\phi' T'}{\partial y}\right) \end{aligned}$$

https://doi.org/10.1017/jfm.2012.549 Published online by Cambridge University Press

$$
\begin{aligned}
&+\left(\frac{\partial u'}{\partial y}+\frac{\partial v'}{\partial x}\right)\left(\mu^0_{\phi y}\phi'+\mu^0_{\phi}\frac{\partial \phi'}{\partial y}+\mu^0_{Ty}T'+\mu^0_{T}\frac{\partial T'}{\partial y}\right)\\
&+\left(\mu^0_{\phi}\frac{\partial \phi'}{\partial z}+\mu^0_{T}\frac{\partial T'}{\partial z}\right)\left(\frac{\partial u'}{\partial z}+\frac{\partial w'}{\partial x}\right)\\
&+(\mu^0_{\phi}\phi'+\mu^0_{T}T')\frac{\partial}{\partial z}\left(\frac{\partial u'}{\partial z}+\frac{\partial w'}{\partial x}\right). \qquad \text{(C 3)}
\end{aligned}
$$

$$
\begin{aligned}
(\phi^0H^2)\mathcal{N}^2_3 = &-H^2\phi'(\boldsymbol{u}'\cdot\boldsymbol{\nabla})u'\\
&-\frac{\partial}{\partial x}\left(\frac{1}{6}p^0_{\phi\phi\phi}\phi'^3+\frac{1}{6}p^0_{TTT}T'^3+\frac{1}{2}p^0_{\phi\phi T}\phi'^2T'+\frac{1}{2}p^0_{\phi TT}\phi'T'^2\right)\\
&+2\left(\frac{1}{2}\mu^0_{\phi\phi}\phi'^2+\frac{1}{2}\mu^0_{TT}T'^2+\mu^0_{\phi T}\phi'T'\right)\frac{\partial^2 u'}{\partial x^2}\\
&+2\left(\frac{1}{2}\mu^0_{\phi\phi}\frac{\partial \phi'^2}{\partial x}+\frac{1}{2}\mu^0_{TT}\frac{\partial T'^2}{\partial x}+\mu^0_{\phi T}\frac{\partial(\phi'T')}{\partial x}\right)\frac{\partial u'}{\partial x}\\
&+\left(\frac{1}{2}\lambda^0_{\phi\phi}\phi'^2+\frac{1}{2}\lambda^0_{TT}T'^2+\lambda^0_{\phi T}\phi'T'\right)\frac{\partial(\boldsymbol{\nabla}\cdot\boldsymbol{u}')}{\partial x}\\
&+\left(\frac{1}{2}\lambda^0_{\phi\phi}\frac{\partial \phi'^2}{\partial x}+\frac{1}{2}\lambda^0_{TT}\frac{\partial T'^2}{\partial x}+\lambda^0_{\phi T}\frac{\partial(\phi'T')}{\partial x}\right)(\boldsymbol{\nabla}\cdot\boldsymbol{u}')\\
&+\left(\frac{1}{6}\mu^0_{\phi\phi\phi}\phi'^3+\frac{1}{6}\mu^0_{TTT}T'^3+\frac{1}{2}\mu^0_{\phi\phi T}\phi'^2T'+\frac{1}{2}\mu^0_{\phi TT}\phi'T'^2\right)u^0_{yy}\\
&+\left(\frac{1}{2}\mu^0_{\phi\phi}\phi'^2+\frac{1}{2}\mu^0_{TT}T'^2+\mu^0_{\phi T}\phi'T'\right)\frac{\partial}{\partial y}\left(\frac{\partial u'}{\partial y}+\frac{\partial v'}{\partial x}\right)\\
&+u^0_y\left(\frac{1}{6}\mu^0_{\phi\phi\phi y}\phi'^3+\frac{1}{6}\mu^0_{\phi\phi\phi}\frac{\partial \phi'^3}{\partial y}+\frac{1}{6}\mu^0_{TTTy}T'^3+\frac{1}{6}\mu^0_{TTT}\frac{\partial T'^3}{\partial y}\right.\\
&\left.+\frac{1}{2}\mu^0_{\phi\phi Ty}\phi'^2T'+\frac{1}{2}\mu^0_{\phi\phi T}\frac{\partial \phi'^2T'}{\partial y}+\frac{1}{2}\mu^0_{\phi TTy}\phi'T'^2+\frac{1}{2}\mu^0_{\phi TT}\frac{\partial \phi'T'^2}{\partial y}\right)\\
&+\left(\frac{\partial u'}{\partial y}+\frac{\partial v'}{\partial x}\right)\left(\frac{1}{2}\mu^0_{\phi\phi y}\phi'^2+\frac{1}{2}\mu^0_{\phi\phi}\frac{\partial \phi'^2}{\partial y}+\frac{1}{2}\mu^0_{TTy}T'^2+\frac{1}{2}\mu^0_{TT}\frac{\partial T'^2}{\partial y}\right.\\
&\left.+\mu^0_{\phi Ty}\phi'T'+\mu^0_{\phi T}\frac{\partial \phi'T'}{\partial y}\right)\\
&+\left(\frac{1}{2}\mu^0_{\phi\phi}\phi'^2+\frac{1}{2}\mu^0_{TT}T'^2+\mu^0_{\phi T}\phi'T'\right)\frac{\partial}{\partial z}\left(\frac{\partial u'}{\partial z}+\frac{\partial w'}{\partial x}\right)\\
&+\left(\frac{1}{2}\mu^0_{\phi\phi}\frac{\partial \phi'^2}{\partial z}+\frac{1}{2}\mu^0_{TT}\frac{\partial T'^2}{\partial z}+\mu^0_{\phi T}\frac{\partial(\phi'T')}{\partial z}\right)\left(\frac{\partial u'}{\partial z}+\frac{\partial w'}{\partial x}\right). \qquad \text{(C 4)}
\end{aligned}
$$

Quadratic ($\mathcal{N}^3_2$) and cubic ($\mathcal{N}^3_3$) nonlinear terms in the y-momentum equation

$$
\begin{aligned}
(\phi^0H^2)\mathcal{N}^3_2 = &-H^2\left[\phi^0(\boldsymbol{u}'\cdot\boldsymbol{\nabla})v'+\phi'\left(\frac{\partial v'}{\partial t}+u^0\frac{\partial v'}{\partial x}\right)\right]\\
&-\left(\frac{1}{2}p^0_{\phi\phi y}\phi'^2+\frac{1}{2}p^0_{\phi\phi}\frac{\partial \phi'^2}{\partial y}+\frac{1}{2}p^0_{TTy}T'^2\right.\\
&\left.+\frac{1}{2}p^0_{TT}\frac{\partial T'^2}{\partial y}+p^0_{\phi Ty}\phi'T'+p^0_{\phi T}\frac{\partial \phi'T'}{\partial y}\right)
\end{aligned}
$$

https://doi.org/10.1017/jfm.2012.549 Published online by Cambridge University Press

$$
\begin{aligned}
&+2\left(\mu^0_\phi\phi'+\mu^0_T T'\right)\frac{\partial^2 v'}{\partial y^2}+2\left(\mu^0_{\phi y}\phi'+\mu^0_\phi\frac{\partial\phi'}{\partial y}+\mu^0_{Ty}T'+\mu^0_T\frac{\partial T'}{\partial y}\right)\frac{\partial v'}{\partial y}\\
&+\left(\lambda^0_\phi\phi'+\lambda^0_T T'\right)\frac{\partial(\boldsymbol{\nabla}\cdot\boldsymbol{u}')}{\partial y}+\left(\lambda^0_{\phi y}\phi'+\lambda^0_\phi\frac{\partial\phi'}{\partial y}+\lambda^0_{Ty}T'+\lambda^0_T\frac{\partial T'}{\partial y}\right)(\boldsymbol{\nabla}\cdot\boldsymbol{u}')\\
&+(\mu^0_\phi\phi'+\mu^0_T T')\frac{\partial}{\partial x}\left(\frac{\partial u'}{\partial y}+\frac{\partial v'}{\partial x}\right)\\
&+u^0_y\left(\mu^0_{\phi\phi}\phi'\frac{\partial\phi'}{\partial x}+\mu^0_{TT}T'\frac{\partial T'}{\partial x}+\mu^0_{\phi T}\frac{\partial\phi' T'}{\partial x}\right)\\
&+\left(\mu^0_\phi\frac{\partial\phi'}{\partial x}+\mu^0_T\frac{\partial T'}{\partial x}\right)\left(\frac{\partial u'}{\partial y}+\frac{\partial v'}{\partial x}\right)\\
&+\left(\mu^0_\phi\phi'+\mu^0_T T'\right)\frac{\partial}{\partial z}\left(\frac{\partial v'}{\partial z}+\frac{\partial w'}{\partial y}\right)\\
&+\left(\mu^0_\phi\frac{\partial\phi'}{\partial z}+\mu^0_T\frac{\partial T'}{\partial z}\right)\left(\frac{\partial v'}{\partial z}+\frac{\partial w'}{\partial y}\right). \qquad \text{(C 5)}
\end{aligned}
$$

$$
\begin{aligned}
(\phi^0H^2)\mathcal{N}^3_3 = &-H^2\phi'(\boldsymbol{u}'\cdot\boldsymbol{\nabla})v'\\
&-\left(\frac{1}{6}p^0_{\phi\phi\phi y}\phi'^3+\frac{1}{6}p^0_{\phi\phi\phi}\frac{\partial\phi'^3}{\partial y}+\frac{1}{6}p^0_{TTTy}T'^3+\frac{1}{6}p^0_{TTT}\frac{\partial T'^3}{\partial y}\right.\\
&\left.+\frac{1}{2}p^0_{\phi\phi Ty}\phi'^2T'+\frac{1}{2}p^0_{\phi\phi T}\frac{\partial\phi'^2T'}{\partial y}+\frac{1}{2}p^0_{\phi TTy}\phi'T'^2+\frac{1}{2}p^0_{\phi TT}\frac{\partial\phi'T'^2}{\partial y}\right)\\
&+2\left(\frac{1}{2}\mu^0_{\phi\phi}\phi'^2+\frac{1}{2}\mu^0_{TT}T'^2+\mu^0_{\phi T}\phi'T'\right)\frac{\partial^2 v'}{\partial y^2}\\
&+2\frac{\partial v'}{\partial y}\left(\frac{1}{2}\mu^0_{\phi\phi y}\phi'^2+\frac{1}{2}\mu^0_{\phi\phi}\frac{\partial\phi'^2}{\partial y}+\frac{1}{2}\mu^0_{TTy}T'^2+\frac{1}{2}\mu^0_{TT}\frac{\partial T'^2}{\partial y}\right.\\
&\left.+\mu^0_{\phi Ty}\phi'T'+\mu^0_{\phi T}\frac{\partial\phi'T'}{\partial y}\right)\\
&+\left(\frac{1}{2}\lambda^0_{\phi\phi}\phi'^2+\frac{1}{2}\lambda^0_{TT}T'^2+\lambda^0_{\phi T}\phi'T'\right)\frac{\partial(\boldsymbol{\nabla}\cdot\boldsymbol{u}')}{\partial y}\\
&+(\boldsymbol{\nabla}\cdot\boldsymbol{u}')\left(\frac{1}{2}\lambda^0_{\phi\phi y}\phi'^2+\frac{1}{2}\lambda^0_{\phi\phi}\frac{\partial\phi'^2}{\partial y}+\frac{1}{2}\lambda^0_{TTy}T'^2\right.\\
&\left.+\frac{1}{2}\lambda^0_{TT}\frac{\partial T'^2}{\partial y}+\lambda^0_{\phi Ty}\phi'T'+\lambda^0_{\phi T}\frac{\partial\phi'T'}{\partial y}\right)\\
&+\left(\frac{1}{2}\mu^0_{\phi\phi}\phi'^2+\frac{1}{2}\mu^0_{TT}T'^2+\mu^0_{\phi T}\phi'T'\right)\frac{\partial}{\partial x}\left(\frac{\partial u'}{\partial y}+\frac{\partial v'}{\partial x}\right)\\
&+u^0_y\left(\frac{1}{6}\mu^0_{\phi\phi\phi}\frac{\partial\phi'^3}{\partial x}+\frac{1}{6}\mu^0_{TTT}\frac{\partial T'^3}{\partial x}\right.\\
&\left.+\frac{1}{2}\mu^0_{\phi\phi T}\frac{\partial(\phi'^2T')}{\partial x}+\frac{1}{2}\mu^0_{\phi TT}\frac{\partial(\phi'T'^2)}{\partial x}\right)\\
&+\left(\frac{1}{2}\mu^0_{\phi\phi}\frac{\partial\phi'^2}{\partial x}+\frac{1}{2}\mu^0_{TT}\frac{\partial T'^2}{\partial x}+\mu^0_{\phi T}\frac{\partial(\phi'T')}{\partial x}\right)\left(\frac{\partial u'}{\partial y}+\frac{\partial v'}{\partial x}\right)
\end{aligned}
$$

https://doi.org/10.1017/jfm.2012.549 Published online by Cambridge University Press

$$+\left(\frac{1}{2}\mu^0_{\phi\phi}\frac{\partial\phi'^2}{\partial z}+\frac{1}{2}\mu^0_{TT}\frac{\partial T'^2}{\partial z}+\mu^0_{\phi T}\frac{\partial(\phi'T')}{\partial z}\right)\left(\frac{\partial v'}{\partial z}+\frac{\partial w'}{\partial y}\right)$$
$$+\left(\frac{1}{2}\mu^0_{\phi\phi}\phi'^2+\frac{1}{2}\mu^0_{TT}T'^2+\mu^0_{\phi T}\phi'T'\right)\frac{\partial}{\partial z}\left(\frac{\partial v'}{\partial z}+\frac{\partial w'}{\partial y}\right). \tag{C 6}$$

Quadratic ($\mathcal{N}^4_2$) and cubic ($\mathcal{N}^4_3$) nonlinear terms in the z-momentum equation

$$\begin{aligned}(\phi^0H^2)\mathcal{N}^4_2 = &-H^2\left[\phi^0(\boldsymbol{u}'\cdot\boldsymbol{\nabla})w'+\phi'\left(\frac{\partial w'}{\partial t}+u^0\frac{\partial w'}{\partial x}\right)\right]\\
&-\left(\frac{1}{2}p^0_{\phi\phi}\frac{\partial\phi'^2}{\partial z}+\frac{1}{2}p^0_{TT}\frac{\partial T'^2}{\partial z}+p^0_{\phi T}\frac{\partial\phi'T'}{\partial z}\right)\\
&+2(\mu^0_\phi\phi'+\mu^0_TT')\frac{\partial^2w'}{\partial z^2}+2\left(\mu^0_\phi\frac{\partial\phi'}{\partial z}+\mu^0_T\frac{\partial T'}{\partial z}\right)\frac{\partial w'}{\partial z}\\
&+(\lambda^0_\phi\phi'+\lambda^0_TT')\frac{\partial(\boldsymbol{\nabla}\cdot\boldsymbol{u}')}{\partial z}+\left(\lambda^0_\phi\frac{\partial\phi'}{\partial z}+\lambda^0_T\frac{\partial T'}{\partial z}\right)(\boldsymbol{\nabla}\cdot\boldsymbol{u}')\\
&+(\mu^0_\phi\phi'+\mu^0_TT')\frac{\partial}{\partial x}\left(\frac{\partial u'}{\partial z}+\frac{\partial w'}{\partial x}\right)\\
&+\left(\mu^0_\phi\frac{\partial\phi'}{\partial x}+\mu^0_T\frac{\partial T'}{\partial x}\right)\left(\frac{\partial u'}{\partial z}+\frac{\partial w'}{\partial x}\right)\\
&+(\mu^0_\phi\phi'+\mu^0_TT')\frac{\partial}{\partial y}\left(\frac{\partial v'}{\partial z}+\frac{\partial w'}{\partial y}\right)\\
&+\left(\mu^0_{\phi y}\phi'+\mu^0_\phi\frac{\partial\phi'}{\partial y}+\mu^0_{Ty}T'+\mu^0_T\frac{\partial T'}{\partial y}\right)\left(\frac{\partial v'}{\partial z}+\frac{\partial w'}{\partial y}\right).\end{aligned} \tag{C 7}$$

$$\begin{aligned}(\phi^0H^2)\mathcal{N}^4_3 = &-H^2\phi'(\boldsymbol{u}'\cdot\boldsymbol{\nabla})w'\\
&-\left(\frac{1}{6}p^0_{\phi\phi\phi}\frac{\partial\phi'^3}{\partial z}+\frac{1}{6}p^0_{TTT}\frac{\partial T'^3}{\partial z}+\frac{1}{2}p^0_{\phi\phi T}\frac{\partial\phi'^2T'}{\partial z}+\frac{1}{2}p^0_{\phi TT}\frac{\partial\phi'T'^2}{\partial z}\right)\\
&+2\left(\frac{1}{2}\mu^0_{\phi\phi}\phi'^2+\frac{1}{2}\mu^0_{TT}T'^2+\mu^0_{\phi T}\phi'T'\right)\frac{\partial^2w'}{\partial z^2}\\
&+2\left(\frac{1}{2}\mu^0_{\phi\phi}\frac{\partial\phi'^2}{\partial z}+\frac{1}{2}\mu^0_{TT}\frac{\partial T'^2}{\partial z}+\mu^0_{\phi T}\frac{\partial\phi'T'}{\partial z}\right)\frac{\partial w'}{\partial z}\\
&+\left(\frac{1}{2}\lambda^0_{\phi\phi}\phi'^2+\frac{1}{2}\lambda^0_{TT}T'^2+\lambda^0_{\phi T}\phi'T'\right)\frac{\partial(\boldsymbol{\nabla}\cdot\boldsymbol{u}')}{\partial z}\\
&+\left(\frac{1}{2}\lambda^0_{\phi\phi}\frac{\partial\phi'^2}{\partial z}+\frac{1}{2}\lambda^0_{TT}\frac{\partial T'^2}{\partial z}+\lambda^0_{\phi T}\frac{\partial\phi'T'}{\partial z}\right)(\boldsymbol{\nabla}\cdot\boldsymbol{u}')\\
&+\left(\frac{1}{2}\mu^0_{\phi\phi}\phi'^2+\frac{1}{2}\mu^0_{TT}T'^2+\mu^0_{\phi T}\phi'T'\right)\frac{\partial}{\partial x}\left(\frac{\partial u'}{\partial z}+\frac{\partial w'}{\partial x}\right)\\
&+\left(\frac{1}{2}\mu^0_{\phi\phi}\frac{\partial\phi'^2}{\partial x}+\frac{1}{2}\mu^0_{TT}\frac{\partial T'^2}{\partial x}+\mu^0_{\phi T}\frac{\partial\phi'T'}{\partial x}\right)\left(\frac{\partial u'}{\partial z}+\frac{\partial w'}{\partial x}\right)\\
&+\left(\frac{1}{2}\mu^0_{\phi\phi}\phi'^2+\frac{1}{2}\mu^0_{TT}T'^2+\mu^0_{\phi T}\phi'T'\right)\frac{\partial}{\partial y}\left(\frac{\partial v'}{\partial z}+\frac{\partial w'}{\partial y}\right)\\
&+\frac{\partial}{\partial y}\left(\frac{1}{2}\mu^0_{\phi\phi}\phi'^2+\frac{1}{2}\mu^0_{TT}T'^2+\mu^0_{\phi T}\phi'T'\right)\left(\frac{\partial v'}{\partial z}+\frac{\partial w'}{\partial y}\right).\end{aligned} \tag{C 8}$$

https://doi.org/10.1017/jfm.2012.549 Published online by Cambridge University Press

Quadratic ($\mathcal{N}_2^5$) and cubic ($\mathcal{N}_3^5$) nonlinear terms in the granular energy equation

$$\begin{aligned}
\left(\frac{3}{2}\phi^0\right)\mathcal{N}_2^5 = &-\frac{3}{2}\left[\phi^0(\boldsymbol{u}'\cdot\boldsymbol{\nabla})T' + \phi'\left(\frac{\partial T'}{\partial t} + T_y^0 v' + u^0\frac{\partial T'}{\partial x}\right)\right] \\
&+ \frac{1}{H^2}\left[\frac{\partial T'}{\partial x}\left(\kappa_\phi^0\frac{\partial\phi'}{\partial x} + \kappa_T^0\frac{\partial T'}{\partial x}\right) + \frac{\partial^2 T'}{\partial x^2}(\kappa_\phi^0\phi' + \kappa_T^0 T')\right. \\
&+ T_y^0\left(\frac{1}{2}\kappa_{\phi\phi y}^0\phi'^2 + \frac{1}{2}\kappa_{\phi\phi}^0\frac{\partial\phi'^2}{\partial y} + \frac{1}{2}\kappa_{TTy}^0 T'^2 + \frac{1}{2}\kappa_{TT}^0\frac{\partial T'^2}{\partial y}\right. \\
&\left. + \kappa_{\phi Ty}^0\phi' T' + \kappa_{\phi T}^0\frac{\partial\phi' T'}{\partial y}\right) + T_{yy}^0\left(\frac{1}{2}\kappa_{\phi\phi}^0\phi'^2 + \frac{1}{2}\kappa_{TT}^0 T'^2 + \kappa_{\phi T}^0\phi' T'\right) \\
&+ \frac{\partial T'}{\partial y}\left(\kappa_{\phi y}^0\phi' + \kappa_\phi^0\frac{\partial\phi'}{\partial y} + \kappa_{Ty}^0 T' + \kappa_T^0\frac{\partial T'}{\partial y}\right) + \frac{\partial^2 T'}{\partial y^2}(\kappa_\phi^0\phi' + \kappa_T^0 T') \\
&\left. + \frac{\partial T'}{\partial z}\left(\kappa_\phi^0\frac{\partial\phi'}{\partial z} + \kappa_T^0\frac{\partial T'}{\partial z}\right) + \frac{\partial^2 T'}{\partial z^2}(\kappa_\phi^0\phi' + \kappa_T^0 T')\right] \\
&- (p_\phi^0\phi' + p_T^0 T')(\boldsymbol{\nabla}\cdot\boldsymbol{u}') + 2\mu^0\left[\left(\frac{\partial u'}{\partial x}\right)^2 + \left(\frac{\partial v'}{\partial y}\right)^2 + \left(\frac{\partial w'}{\partial z}\right)^2\right] \\
&+ \mu^0\left(\frac{\partial u'}{\partial y} + \frac{\partial v'}{\partial x}\right)^2 + (u_y^0)^2\left(\frac{1}{2}\mu_{\phi\phi}^0\phi'^2 + \frac{1}{2}\mu_{TT}^0 T'^2 + \mu_{\phi T}^0\phi' T'\right) \\
&+ 2\,u_y^0\,(\mu_\phi^0\phi' + \mu_T^0 T')\left(\frac{\partial u'}{\partial y} + \frac{\partial v'}{\partial x}\right) + \mu^0\left(\frac{\partial v'}{\partial z} + \frac{\partial w'}{\partial y}\right)^2 \\
&+ \mu^0\left(\frac{\partial w'}{\partial x} + \frac{\partial u'}{\partial z}\right)^2 + \lambda^0\,(\boldsymbol{\nabla}\cdot\boldsymbol{u}')^2 \\
&- \left(\frac{1}{2}\mathcal{D}_{\phi\phi}^0\phi'^2 + \frac{1}{2}\mathcal{D}_{TT}^0 T'^2 + \mathcal{D}_{\phi T}^0\phi' T'\right). \qquad \text{(C 9)}
\end{aligned}$$

$$\begin{aligned}
\left(\frac{3}{2}\phi^0\right)\mathcal{N}_3^5 = &-\frac{3}{2}\phi'(\boldsymbol{u}'\cdot\boldsymbol{\nabla})T' + \frac{1}{H^2}\left[\frac{\partial T'}{\partial x}\left(\frac{1}{2}\kappa_{\phi\phi}^0\frac{\partial\phi'^2}{\partial x} + \frac{1}{2}\kappa_{TT}^0\frac{\partial T'^2}{\partial x} + \kappa_{\phi T}^0\frac{\partial\phi' T'}{\partial x}\right)\right. \\
&+ \frac{\partial^2 T'}{\partial x^2}\left(\frac{1}{2}\kappa_{\phi\phi}^0\phi'^2 + \frac{1}{2}\kappa_{TT}^0 T'^2 + \kappa_{\phi T}^0\phi' T'\right) \\
&+ T_y^0\left(\frac{1}{6}\kappa_{\phi\phi\phi y}^0\phi'^3 + \frac{1}{6}\kappa_{\phi\phi\phi}^0\frac{\partial\phi'^3}{\partial y} + \frac{1}{6}\kappa_{TTTy}^0 T'^3 + \frac{1}{6}\kappa_{TTT}^0\frac{\partial T'^3}{\partial y}\right. \\
&\left. + \frac{1}{2}\kappa_{\phi\phi Ty}^0\phi'^2 T' + \frac{1}{2}\kappa_{\phi\phi T}^0\frac{\partial\phi'^2 T'}{\partial y} + \frac{1}{2}\kappa_{\phi TTy}^0\phi' T'^2 + \frac{1}{2}\kappa_{\phi TT}^0\frac{\partial\phi' T'^2}{\partial y}\right) \\
&+ T_{yy}^0\left(\frac{1}{6}\kappa_{\phi\phi\phi}^0\phi'^3 + \frac{1}{6}\kappa_{\phi TT}^0 T'^3 + \frac{1}{2}\kappa_{\phi\phi T}^0\phi'^2 T' + \frac{1}{2}\kappa_{\phi TT}^0\phi' T'^2\right) \\
&+ \frac{\partial T'}{\partial y}\left(\frac{1}{2}\kappa_{\phi\phi y}^0\phi'^2 + \frac{1}{2}\kappa_{\phi\phi}^0\frac{\partial\phi'^2}{\partial y} + \frac{1}{2}\kappa_{TTy}^0 T'^2\right. \\
&\left. + \frac{1}{2}\kappa_{TT}^0\frac{\partial T'^2}{\partial y} + \kappa_{\phi Ty}^0\phi' T' + \kappa_{\phi T}^0\frac{\partial\phi' T'}{\partial y}\right) \\
&\left. + \frac{\partial^2 T'}{\partial y^2}\left(\frac{1}{2}\kappa_{\phi\phi}^0\phi'^2 + \frac{1}{2}\kappa_{TT}^0 T'^2 + \kappa_{\phi T}^0\phi' T'\right)\right.
\end{aligned}$$

https://doi.org/10.1017/jfm.2012.549 Published online by Cambridge University Press

$$+\frac{\partial T'}{\partial z}\left(\frac{1}{2}\kappa^0_{\phi\phi}\frac{\partial \phi'^2}{\partial z}+\frac{1}{2}\kappa^0_{TT}\frac{\partial T'^2}{\partial z}+\kappa^0_{\phi T}\frac{\partial \phi' T'}{\partial z}\right)$$
$$+\frac{\partial^2 T'}{\partial z^2}\left(\frac{1}{2}\kappa^0_{\phi\phi}\phi'^2+\frac{1}{2}\kappa^0_{TT}T'^2+\kappa^0_{\phi T}\phi' T'\right)\Bigg]$$
$$-\left(\frac{1}{2}p^0_{\phi\phi}\phi'^2+\frac{1}{2}p^0_{TT}T'^2+p^0_{\phi T}\phi' T'\right)(\boldsymbol{\nabla}\cdot\boldsymbol{u}')$$
$$+2(\mu^0_\phi\phi'+\mu^0_T T')\left[\left(\frac{\partial u'}{\partial x}\right)^2+\left(\frac{\partial v'}{\partial y}\right)^2+\left(\frac{\partial w'}{\partial z}\right)^2\right]$$
$$+\left(\frac{1}{6}\mu^0_{\phi\phi\phi}\phi'^3+\frac{1}{6}\mu^0_{TTT}T'^3+\frac{1}{2}\mu^0_{\phi\phi T}\phi'^2T'+\frac{1}{2}\mu^0_{\phi TT}\phi' T'^2\right)(u^0_y)^2$$
$$+2u^0_y\left(\frac{1}{2}\mu^0_{\phi\phi}\phi'^2+\frac{1}{2}\mu^0_{TT}T'^2+\mu^0_{\phi T}\phi' T'\right)\left(\frac{\partial u'}{\partial y}+\frac{\partial v'}{\partial x}\right)$$
$$+(\mu^0_\phi\phi'+\mu^0_T T')\left[\left(\frac{\partial u'}{\partial y}+\frac{\partial v'}{\partial x}\right)^2+\left(\frac{\partial v'}{\partial z}+\frac{\partial w'}{\partial y}\right)^2+\left(\frac{\partial w'}{\partial x}+\frac{\partial u'}{\partial z}\right)^2\right]$$
$$+\left(\lambda^0_\phi\phi'+\lambda^0_T T'\right)(\boldsymbol{\nabla}\cdot\boldsymbol{u}')^2$$
$$-\left(\frac{1}{6}\mathcal{D}^0_{\phi\phi\phi}\phi'^3+\frac{1}{6}\mathcal{D}^0_{TTT}T'^3+\frac{1}{2}\mathcal{D}^0_{\phi\phi T}\phi'^2T'+\frac{1}{2}\mathcal{D}^0_{\phi TT}\phi' T'^2\right). \tag{C 10}$$

REFERENCES

ALAM, M. 2005 Universal unfolding of pitchfork bifurcations and the shear-band formation in rapid granular Couette flow. In *Trends in Applications of Mathematics to Mechanics* (ed. Y. Wang & K. Hutter), pp. 11–20. Shaker.

ALAM, M. 2006 Streamwise structures and density patterns in rapid granular Couette flow: a linear stability analysis. *J. Fluid Mech.* **553**, 1.

ALAM, M., ARAKERI, V. H., GODDARD, J. D., NOTT, P. R. & HERRMANN, H. J. 2005 Instability-induced ordering, universal unfolding and the role of gravity in granular Couette flow. *J. Fluid Mech.* **523**, 277.

ALAM, M., CHIKKADI, V. K. & GUPTA, V. K. 2009 Density waves and the effect of wall roughness in granular Poiseuille flow: simulation and linear stability. *Eur. Phys. J. ST* **179**, 69.

ALAM, M. & LUDING, S. 2003 First normal stress difference and crystallization in a dense sheared granular fluid. *Phys. Fluids* **15**, 2298.

ALAM, M. & LUDING, S. 2005 Energy nonequipartition, rheology and microstructure in sheared bidisperse granular mixtures. *Phys. Fluids* **17**, 063303.

ALAM, M. & NOTT, P. R. 1998 Stability of plane Couette flow of a granular material. *J. Fluid Mech.* **377**, 99.

ALAM, M. & SHUKLA, P. 2008 Nonlinear stability of granular shear flow: Landau equation, shear-banding and universality. In *Proceedings of International Conference on Theoretical and Applied Mechanics* (ISBN 978-0-9805142-0-9), *24–29 August, Adelaide, Australia*.

ALAM, M. & SHUKLA, P. 2012 Origin of subcritical shear-banding instability in a dense two-dimensional sheared granular fluid. *Gran. Matt.* **14**, 221.

ALAM, M., SHUKLA, P. & LUDING, S. 2008 Universality of shear-banding instability and crystallization in sheared granular fluid. *J. Fluid Mech.* **615**, 293.

ARANSON, I. S. & TSIMRING, L. S. 2006 Patterns and collective behaviour in granular media: theoretical concepts. *Rev. Mod. Phys.* **78**, 641.

https://doi.org/10.1017/jfm.2012.549 Published online by Cambridge University Press

BRILLIANTOV, N. V. & PÖSCHEL, T. 2004 *Kinetic Theory of Granular Gases*. Oxford University Press.

CANUTO, C., HUSSAINI, M. Y., QUARTERONI, A. & ZANG, T. A. 1988 *Spectral Methods in Fluid Dynamics*. Springer.

CARR, J. 1981 *Applications of Center Manifold Theory*. Springer.

CHIKKADI, V. K. & ALAM, M. 2009 Slip velocity and stresses in granular Poiseuille flow via event-driven simulation. *Phys. Rev.* E **79**, 021303.

CHONG, M. S., PERRY, A. E. & CANTWELL, B. J. 1990 A general classification of three-dimensional flow fields. *Phys. Fluids* A **2**, 765.

CONWAY, S. & GLASSER, B. J. 2004 Density waves and coherent structures in granular Couette flow. *Phys. Fluids* **16**, 509.

CROSS, M. C. & HOHENBERG, P. 1993 Patterns formation outside of equilibrium. *Rev. Mod. Phys.* **65**, 851.

DRAZIN, P. G. 1992 *Nonlinear Systems*. Cambridge University Press.

DRAZIN, P. G. & REID, W. H. 1981 *Hydrodynamic Stability*. Cambridge University Press.

ECKHAUS, W. 1965 *Studies in Nonlinear Stability Theory*. Cambridge University Press.

ESHUIS, P., VAN DER MEER, D., ALAM, M., VAN GERNER, H. J., VAN DER WEELE, K. & LOHSE, D. 2010 Onset of convection in strongly shaken granular matter. *Phys. Rev. Lett.* **104**, 038001.

FORTERRE, F. & POULIQUEN, O. 2002 Stability analysis of rapid granular chute flows: formation of longitudinal vortices. *J. Fluid Mech.* **467**, 361.

GALLAS, J. A . C., HERRMANN, H. J. & SOKOLOWSKI, S. 1992 Convection cells in vibrating granular layers. *Phys. Rev. Lett.* **69**, 1371.

GARZO, V. & DUFTY, J. W. 1999 Dense fluid transport for inelastic hard spheres. *Phys. Rev.* E **59**, 5895.

GARZO, V., SANTOS, A. & MONTANERO, J. M. 2007 Modified Sonine approximation for the Navier–Stokes transport coefficients of a granular gas. *Physica* A **376**, 94.

GAYEN, B. & ALAM, M. 2006 Algebraic and exponential instabilities in a sheared micropolar granular fluid. *J. Fluid Mech.* **567**, 195.

GODDARD, J. D. & ALAM, M. 1999 Shear flow and material instabilities in particulate suspensions and dry granular media. *Particulate Sci. Tech.* **17**, 69.

GOLDFARB, D. J., GLASSER, B. J. & SHINBROT, T. 2002 Shear instabilities in granular flows. *Nature* **415**, 302.

GOLDHIRSCH, I. 2003 Rapid granular flows. *Annu. Rev. Fluid Mech.* **35**, 267.

HOPKINS, M. A., JENKINS, J. T. & LOUGE, M. Y. 1993 On the structure of three-dimensional shear flows. In *Advances in Micromechanics of Granular Materials* (ed. H. H. Shen, M. Satake, M. Mehrabadi, C. S. Chang & C. S. Campbell), pp. 271–279. Elsevier.

JACKSON, R. 2000 *Dynamics of Fluidized Beds*. Cambridge University Press.

JENKINS, J. T. & RICHMAN, M. W. 1985 Grads 13-moment system for a dense gas of inelastic spheres. *Arch. Rat. Mech. Anal.* **87**, 355.

JENKINS, J. T. & RICHMAN, M. W. 1986 Boundary conditions for plane flows of smooth, nearly elastic, circular disks. *J. Fluid Mech.* **171**, 53.

JEONG, J. & HUSSAIN, F. 1995 On the identification of a vortex. *J. Fluid Mech.* **285**, 69.

KHAIN, E. & MEERSON, B. 2006 Shear-induced crystallization of a dense rapid granular flow: hydrodynamics beyond the melting point. *Phys. Rev.* E **73**, 061301.

LUN, C. K. K., SAVAGE, S. B., JEFFREY, D. J. & CHEPURNIY, N. 1984 Kinetic theories for granular flow: inelastic particles in Couette flow and slightly inelastic particles in a general flow field. *J. Fluid Mech.* **140**, 223.

MACK, L. M. 1984 Boundary layer linear stability theory. *AGARD Rep.* 709, p. 3-1.

MALIK, M., ALAM, M. & DEY, J. 2006 Nonmodal energy growth and optimal perturbations in compressible Couette flow. *Phys. Fluids* **18**, 034103.

MALIK, M., DEY, J. & ALAM, M. 2008 Linear stability, transient energy growth and the role of viscosity stratification in compressible plane Couette flow. *Phys. Rev.* E **77**, 036322.

MCNAMARA, S. 1993 Hydrodynamic modes of a uniform granular medium. *Phys. Fluids* A **5**, 3056.

https://doi.org/10.1017/jfm.2012.549 Published online by Cambridge University Press

MOROZOV, A. N. & VAN SAARLOOS, W. 2007 An introductory essay on subcritical instabilities and the transition to turbulence in visco-elastic parallel shear flows. *Phys. Rep.* **447**, 112.

NOSKOWICZ, S. H., BAR-LEV, O., SERERO, D. & GOLDHIRSCH, I. 2007 Computer-aided kinetic theory and granular gases. *Europhys. Lett.* **79**, 60001.

PERRY, A. E. & CHONG, M. S. 1987 A description of eddying motions and flow patterns using critical-point concepts. *Annu. Rev. Fluid Mech.* **19**, 125.

RAAFAT, T., HULIN, J. P. & HERRMANN, H. J. 1996 Density waves in dry granular media falling through a vertical pipe. *Phys. Rev.* E **53**, 4345.

RAMIREZ, R., RISSO, D. & CORDERO, P. 2000 Thermal convection in fluidized granular systems. *Phys. Rev. Lett.* **85**, 1030.

REYNOLDS, W. C. & POTTER, M. C. 1967 Finite amplitude instability of parallel shear flows. *J. Fluid Mech.* **27**, 465.

SAITOH, K. & HAYAKAWA, H. 2007 Rheology of a granular gas under a plane shear. *Phys. Rev.* E **75**, 021302.

SAITOH, K. & HAYAKAWA, H. 2011 Weakly nonlinear analysis of two-dimensional sheared granular flow. *Granul. Matt.* **13**, 679.

SAUERMANN, G., KROY, K. & HERRMANN, H. J. 2001 A continuum saltation model for sand dunes. *Phys. Rev.* E **64**, 031305.

SAVAGE, S. B. 1992 Instability of unbounded uniform granular shear flow. *J. Fluid Mech.* **241**, 109.

SELA, N. & GOLDHIRSCH, I. 1998 Hydrodynamic equations for rapid shear flows of smooth, inelastic spheres, to Burnett order. *J. Fluid Mech.* **361**, 41.

SHUKLA, P. & ALAM, M. 2009 Order parameter description of shear-banding in granular Couette flow via Landau equation. *Phys. Rev. Lett.* **103**, 068001.

SHUKLA, P. & ALAM, M. 2011*a* Weakly nonlinear theory of shear-banding instability in granular plane Couette flow: analytical solution, comparison with numerics and bifurcation. *J. Fluid Mech.* **666**, 204.

SHUKLA, P. & ALAM, M. 2011*b* Nonlinear stability and patterns in granular plane Couette flow: Hopf and pitchfork bifurcations, and evidence for resonance. *J. Fluid Mech.* **672**, 147.

SHUKLA, P. & ALAM, M. 2012 Nonlinear vorticity banding instability in granular plane Couette flow: higher-order Landau coefficient, bistability and bifurcation scenario. *J. Fluid Mech.* (in press).

STUART, J. T. 1960 On the nonlinear mechanics of wave disturbances in stable and unstable parallel flows. *J. Fluid Mech.* **9**, 353.

TAN, M.-L. & GOLDHIRSCH, I. 1997 Inter-cluster interactions in rapid granular shear flows. *Phys. Fluids* **9**, 856.

TREFETHEN, N. & BAU, H. 1997 *Linear Algebra*. SIAM.

UMBANHOWER, P., MELO, F. & SWINNEY, H. L. 1996 Oscillons in vibrated granular media. *Nature* **382**, 793.

WATSON, J. 1960 On the nonlinear mechanics of wave disturbances in stable and unstable parallel flows. *J. Fluid Mech.* **9**, 371.

WOODHOUSE, M. J. & HOGG, A. J. 2010 Rapid granular flows down inclined planar chutes. Part 2. Linear stability analysis of steady flow solutions. *J. Fluid Mech.* **652**, 461.

https://doi.org/10.1017/jfm.2012.549 Published online by Cambridge University Press